UNIVERSITY OF CALIFORNIA
RIVERSIDE

Studies on the Production and Characteristics of Natural and Anthropogenic Aerosols

A Dissertation submitted in partial satisfaction
of the requirements for the degree of

Doctor of Philosophy

in

Environmental Sciences

by

Alexander L. Frie

June 2019

Dissertation Committee:
Dr. Roya Bahreini, Chairperson
Dr. Samantha Ying
Dr. Ying-Hsuan Lin

The Dissertation of Alexander L. Frie is approved by:

_____

_____

_____

Committee Chairperson

University of California, Riverside

Acknowledgements

The Author would like to thank the various scientists who supported the technical aspects of this work including Dr. Yongxuan Su, Andrew Robinson, Steve Bates, and David Lyons, and Macon Abernathy.

Funding Sources for this work include the UCR department of Environmental Science, UCR Regents' Faculty Development Award, UCR Office of Research and Development Collaborative Seed Grant Program, USDA National Institute of Food and Agriculture, Hatch project Accession No. 233133, USDA (Accession No. 1015963, Project No. CA-R-ENS-5072-H), NSF (AGS 1454374), and the U.S. Geological Survey under Grant/Cooperative Agreement Nos. G11AP20121 and G16AP00041. The views and conclusions contained in this document are those of the authors and should not be interpreted as representing the opinions or policies of the U.S. Geological Survey. Mention of trade names or commercial products does not constitute their endorsement by the U.S. Geological Survey.

The text of this dissertation, in part or in full, is a reprint of the material as it appears in "The Effect of a Receding Saline Lake (The Salton Sea) on Airborne Particulate Matter Composition" published within *Environmental Science and Technology* in 2017 which was authored by Alexander L. Frie, Justin H. Dingle, Samantha C. Ying, and Roya Bahreini, "Brown Carbon Formation from Nighttime Chemistry of Heterocyclic Aromatic Compounds." published within *Environmental Science and Technology Letters* in 2019 which was authored by Huanhuan Jiang and Alexander L. Frie, Jin Chen, Avi Lavi, Haofei Zhang, Roya Bahreini and Ying-Hsuan Lin, and "Dust Sources in the Salton Sea Basin: A

Clear Case of an Anthropogenically Impacted Dust Budget" submitted to *Environmental Science and Technology* in 2019 which was authored by Alexander L. Frie, Alexis C. Garrison, Michael V. Schaefer, Steve Bates, Jon Botthoff, Mia Maltz, Samantha C. Ying, Timothy Lyons, Emma Aronson, and Roya Bahreini. The co-author Roya Bahreini listed in those publications directed and supervised the research which forms the basis for this dissertation.

Dedication

I would like to thank all those who have supported me while I worked towards completion of my Ph.D. First, I would like to thank my wife, Sara Frie Vliet. I am lucky to have partner who also chose to pursue a PhD and has been able to share my joys and struggles. She has always supported me and my academic pursuits and is constant reminder that academics are important but only one component of my life. Second, I would like to thank my family. Coming to UCR has meant missing birthdays, holidays, and memories. Despite this, all you've ever given me is support. Thank you. Third, I would like to thank the friends who have made my time at UCR a time in I will always look upon fondly. Whether climbing physical or metaphorical mountains I have been fortunate to always have friends willing to lend a hand. One secret challenge of graduate school is the bittersweet taste of graduation as you watch your friends move forward; now it's my turn and the bittersweet is a two-way street. I will miss the morning coffees, evening beers, and weekend hikes we've shared. I wish all of you success, but most of all happiness. Fourth, I'd like to thank all of the scientists and staff who have supported me. I would also like to thank my committee members Dr. Ying-Hsuan Lin and Dr. Samantha Ying, this document could not exist without their significant contributions. Lastly, I would like to thank my mentor Roya Bahreini who has been the best advisor a student could ask for. She has given me the independence to pursue my own lines of inquiry and but also made sure I was always moving towards success.

ABSTRACT OF THE DISSERTATION

Studies on the Production and Characteristics of Natural and Anthropogenic Aerosols

by

Alexander L. Frie

Doctor of Philosophy, Graduate Program in Environmental Sciences
University of California Riverside, June 2019
Roya Bahreini, Chairperson

Aerosol particles (hereafter referred to as aerosols) impact the earth system, affecting climate, ecosystems, and health. To understand aerosols' effects and mitigate their negative impacts we must understand the sources of aerosols and of their properties. This work explores two case studies investigating sources: one investigating the sources of mineral dust aerosols and one investigating sources of aerosol absorption. Additionally, a technique for estimating the uncertainty in the full distribution optical closure method (FDOCM) of refractive index (*m*) calculations is presented.

In the first study, the sources of aerosols in the Salton Sea Basin, CA, were explored through 2 field campaigns. The Salton Sea Basin is a region of poor air quality, which is thought to be primarily controlled by natural dust emissions. Although mineral dust is often considered a natural source, recently observed increases in dust emissions reveal the importance of anthropogenic controls. In the first field campaign, PM_{10} was sampled in August 2015 and February 2016. In the second, passive dust samples were collected ~monthly from May 2017 to May 2018. Elemental composition and soluble anion content

of the dust samples were used as inputs into positive matrix factorization (PMF). This investigation revealed multiple dust sources traceable to geologic features and anthropogenic activities. Of particular interest, is the importance of an emerging lakebed, which is identified as a new dust source, possibly worsening regional air quality.

In the second case study, secondary organic aerosol (SOA) generated from the nitrate oxidation of heterocyclic compounds (pyrrole, furan, and thiophene) was investigated as a potential source of absorbing organic aerosol. This investigation employed chamber experiments, on- and offline optical measurements, and on- and offline mass spectrometry to explore the optical and chemical properties of the gas phase intermediates and aerosols. These experiments revealed pyrrole SOA as a potential source of absorbing aerosol and possibly an important component of biomass burning SOA.

Lastly, a technique for estimating the uncertainty in FDOCM was developed. Uncertainties in FDOCM results were estimated by repeatedly performing the optical closure calculations with perturbed inputs. Simulated inputs reveal the dependence of *m* uncertainty on the size distribution and *m*. This method can be applied to help better constrain uncertainty in *m* calculations and yield more certain radiative forcing estimations.

Table of Contents

List of Figures

List of Tables

List of Equations

List of Acronyms and Symbols

$2\sigma_{norm\_n}$: Normalized *n* 68% confidence interval
$2\sigma_{norm\_k}$: Normalized *k* 68% confidence interval
Å: Angstrom Exponent
β_{abs}: Absorption Coefficient
β_{scat}: Scattering Coefficient
β_{scat_Theo}: Theoretical Scattering Coefficient in Mie Theory Calculations
β_{abs_Theo}: Theoretical Absorption Coefficient in Mie Theory Calculations
β_{scat_obs}: Observed Scattering Coefficient in Mie Theory Calculations
β_{abs_obs}: Observed Absorption Coefficient in Mie Theory Calculations
σ_{abs}: Relative Uncertainty in Absorption Measurement
σ_{scat}: Relative Uncertainty in Scattering Measurement
σ_{dia}: Relative Uncertainty in Diameter Measurement
σ_{N}: Relative Uncertainty in Number Concentration Measurement
λ: Wavelength
BB: Bombay Beach
BBS: Bombay Beach Summer
BC: Black Carbon
BD: Boyd Deep Canyon
BLM: Bureau of Land Management
BrC: Brown Carbon
CAFW: California Fish and Wildlife
d_p: Particle Diameter
DAD: Diode Array Detector
DP: Dos Palmas
DRE: Direct Radiative Effect
ED-XRF: X-ray Florescence spectroscopy
EF: Enrichment Factor
EF_{absC}: Absorption Cross-Section Emission Factor
ESI: Electrospray Ionization
F_{org}: Fraction Organic Matter
FDOCM: Full Distribution Optical Closure Method
Height: Fit measure used to ensure m_{true} sampling space is the correct size
HR-ToF-CIMS: High-Resolution Time-of-Flight Chemical Ionization Mass Spectrometer
HR-TOFMS: High-Resolution Time-of-Flight Mass Spectrometer
HYSPLIT: Hybrid Single Particle Lagrangian Integrated Trajectory Model
I_{spin}: Number of Iterations during Spin up of RICE
I_{final}: Number of Iterations during the final cycle of RICE
ICP-MS: Inductively Couple Plasma Mass Spectroscopy
Idle: Count of the number of 0 probability n_{true} or k_{true} values test by RICE
IVOC: Intermediately Volatile Organic Compound
IMR: Ion Molecule Reaction Region

***k*:** Imaginary Component of the Refractive Index
k_{true}: k component of m_{true} tested for ability to yield m_r
k_{width}: half width of the k space explored for k_{true} values which could yield m_{calc}
***m*:** Complex Refractive Index
m_r: Retrieved m
m_{true}: m value tested for ability to yield m_r
m_{calc}: solution m values to RICE iterations
n_{width}: half width of the n space explored for n_{true} values which could yield n_{calc}
$\mathbf{M}_{spin}$: n by k matrix size during Spin up of RICE
$\mathbf{M}_{final}$: n by k matrix size during final cycle of RICE
MAC: Mass Absorption Coefficient
MOUDI: Micro-orifice Uniform Deposition Impactor
n: Real Component of the Refractive Index
n_{true}: n component of m_{true} tested for ability to yield m_r
OA: Organic Aerosol
OCM: Optical Closure Method
OHV: Off Highway Vehicle
PAX: Photoacoustic Extinctiometer
PD: Palm Desert
PM: Particulate Matter
$\mathbf{PM_{10}}$: Particulate Matter with Aerodynamic Diameters ≤ 10 μm
PMF: Positive Matrix Factorization
POA: Primary Organic Aerosol
QSA: Quantification Settlement Agreement
Q_{scat}: Scattering Efficiency
Q_{abs}: Absorption Efficiency
RH: Relative Humidity
RICE: Refractive Index Confidence Explorer
SB: Sonny Bono
SC: Salton City
SCS: Salton City Summer
SCW: Salton City Winter
SEM-EDS: Energy-Dispersive X-ray Spectroscopy
SEMS: Scanning Electron Mobility Spectrometer
SOA: Secondary Organic Aerosol
$\mathbf{SOA_{pot}}$: Potential Secondary Organic Aerosol
SSA: Single Scattering Albedo
SSOCM: Size Selected Optical Closure Method
SVOC: Semi-Volatile Organic Compound
UC: University of California
UCC: Upper Continental Crust
UV: Ultra Violet
USFW: United Stated Fish and Wildlife Service
VOC: Volatile Organic Compound

WI: Wister
XRD: X-Ray Diffraction
$\boldsymbol{Y_{SOA}}$: Secondary Organic Aerosol Yield

Chapter 1: Introduction to Studies on The Production and Characteristics of Natural and Anthropogenic Aerosols

1.0 Introduction

Aerosol particles, solid or liquid phase particles suspended in the atmosphere, dramatically affect human health and the condition of the earth's environment. These particles influence rainfall, seasonal weather patterns, cloud formation and lifetime, and top of the atmosphere radiative forcing, affecting climate on local, regional, and global scales.[1–3] Furthermore, increases in aerosol mass have been linked to cardiovascular disease, respiratory disease, and mortality.[4] In addition, the composition of aerosol particles can increase toxicity.[5–7] Despite these broad impacts, a fundamental understanding of aerosol properties and sources is still developing. In this work, a series of studies examining the sources and properties of multiple types of aerosols are presented.

1.1 Aerosols Sources

Before aerosols can affect health, interact with radiation, or deposit, they must be emitted into or form within the atmosphere, as primary or secondary aerosols respectively. Because of this, aerosol sources must be constrained if aerosol effects are to be appropriately understood, modeled, and/or mitigated. Primary aerosol sources include vehicle emissions, plants, wildfires, soils.[8–12] To understand the effects of aerosols in a specific region and across the globe, it is crucial to identify the relative importance of individual sources.

A large variety of methods have been used to identify aerosol sources. These include visual identification, composition-based receptor models, complex chemical

models, and satellite measurements.[13–18] Through applying these tools, the aerosol community has identified major aerosol types including primary or secondary organic aerosol, inorganic aerosol, soot, mineral dust, and sea spray. Differences in aerosol sources affect the aerosol population in unique ways and on time scales ranging from seasonal to minutes. For example, in many urban areas aerosols are dominated by relatively small-diameter (<1 μm) secondary organic aerosols (SOA) sourced from traffic emissions and the resulting atmospheric chemistry; SOA in these areas often have dramatic seasonality and diurnal patterns.[8] These patterns will depend on traffic patterns, but also occur in part because photochemistry is a major pathway of SOA formation and photochemistry and rates are, in part, controlled by the solar flux which is seasonally dependent.[19] In contrast, aerosol populations in desert regions are often dominated by relatively large-diameter mineral dust. The concentrations of these particles are not controlled by chemistry, but instead almost solely by meteorological conditions (e.g., wind speed or precipitation).[20] Given this, aerosol effects and mitigation strategies in a remote desert region would be much different than in an urban region. Given the diversity of aerosol sources and their broad impacts, it is essential to understand aerosol sources on local, regional, and global scales.

1.2 Mineral Dust Aerosols and Playas

Mineral dust aerosols are widely accepted as one of the largest sources of aerosol mass on Earth.[21] Despite this, significant uncertainty exists in estimations of mineral dust effects on air quality and the radiation budget.[21–23] These uncertainties arise in part from an incomplete understanding of dust emissions and human activity driven changes in the

dust budget. Anthropogenic activity increases mineral dust emission by changing vegetative cover, destroying protective features (e.g. soil crusts), and causing direct emissions.[24] These actions and land use changes are thought to cause a net increase in global dust emissions.

One major way humans have influenced the dust budget is through water management. Globally, humans have been diverting water from arid endorheic basins and causing saline lakes to recede and salt crusted surfaces, known as playas, to form. As long as ground water is present, these salt crusts are regenerative and become potentially emissive surfaces, often more emissive than the surrounding desert.[25] In Chapters two and three the importance of an emerging playa as a dust source in the Southwest US is investigated.

1.3 Aerosols and Climate

Due to an incomplete understanding of aerosol properties, aerosol direct and indirect climate effects provide the largest sources of uncertainty in predictions of the anthropogenic impacts on climate.[26] The aerosol direct radiative effect (DRE) is driven by the primary interaction of aerosol particles with light whereas the aerosol indirect effect is driven by effects on cloud formation, properties, and lifetime, resulting in surface albedo changes. One area of uncertainty is compositionally driven variation in aerosol absorption and scattering of radiation, which are major optical properties of aerosols and control the DRE. Without characterizing the optical properties of aerosols from major emissions sources, the chemical drivers of optical properties, and the influence of various aging conditions, characterization of the radiative balance of the Earth system is limited.

Aerosol optical properties are the quantities used to describe how aerosols interact with radiation. These quantities are described by the refractive index (*m*) of the aerosol material. Accurate determination of *m* of aerosols is crucial, as it is the determining factor for DRE of aerosols. To better constrain aerosol DRE, *m* values in aerosols of different compositions and the parameters controlling *m* values under diverse atmospheric conditions must be constrained. In chapter five of this work, a new method of estimating the uncertainty in aerosol *m* calculations is presented.

1.4 Optical Properties of Secondary Organic Aerosol

Secondary organic aerosols, those formed from the oxidation of volatile organic compounds (VOCs) or intermediate/semi volatile organic compounds (IVOCs and SVOCs, respectively), have atmospheric concentrations that rival/are greater than those of sulfate and nitrate, common anthropogenic inorganic components of aerosols.[27,28] Despite the large contribution to submicron aerosol mass, optical properties of SOA are not fully characterized.

To form SOA in the gas phase, gaseous vapors are oxidized by ubiquitous atmospheric oxidants including O_3, ·OH, NO_3, and ·Cl. These oxidation processes can functionalize or fragment hydrocarbons; fragmentation leads to smaller compounds while functionalization leads to more oxidized and larger compounds.[29] The functionalization is generally thought to decrease saturation vapor pressure and drive the condensation of products to form SOA.[30] Due to the diverse reaction conditions and multitude of VOC + oxidant combinations, the physio chemical properties of SOA are very diverse, resulting also in diverse optical properties.

Chamber experiments have repeatedly revealed that increases in NO_x concentrations are associated with higher absorption for anthropogenic and biogenic SOA.[31–33] The influence of NO_x on SOA absorption demonstrates changes in chemical nature and development of chromophoric components within SOA. The ability of a compound to absorb radiation is driven by the stability/distance of electron transitions.[34] For example, long conjugated chains or functionalized species are more likely to absorb at visible wavelengths because n to π* transitions require less energy. Given this principle, it is expected that N-containing, O-containing, and aromatic species will be more likely to absorb within the near UV-visible light spectrum. Multiple studies have demonstrated the role of NO_x in the formation of organonitrate and nitro organic compounds, which have been in turn observed in both the lab and field to act as chromophores.[35–40] An additional source of N containing SOA is the oxidation of VOCs by nitrate ($NO_3^{\cdot}$) radicals, the predominant nighttime oxidant in the atmosphere. In this work, functionalized heterocyclic aromatic compounds are examined for their potential to create absorbing organic aerosols (Chapter 4).

1.5 Works Cited

1. Bond, T. C. *et al.* Bounding the role of black carbon in the climate system: A scientific assessment. *J. Geophys. Res. Atmos.* 118, 5380–5552 (2013).

2. Koehler, K. A. *et al.* Laboratory investigations of the impact of mineral dust aerosol on cold cloud formation. *Atmos. Chem. Phys.* 10, 11955–11968 (2010).

3. Ramanathan, V. & Carmichael, G. Global and regional climate changes due to black carbon. *Nature Geosci* 1, 221–227 (2008).

4. Kelly, F. J. & Fussell, J. C. Air pollution and public health: emerging hazards and improved understanding of risk. *Environ Geochem Health* 37, 631–649 (2015).

5. Kelly, F. J. & Fussell, J. C. Size, source and chemical composition as determinants of toxicity attributable to ambient particulate matter. *Atmos. Environ.* 60, 504–526 (2012).

6. Tsai, F. C., Apte, M. G. & Daisey, J. M. An exploratory analysis of the relationship between mortality and the chemical composition of airborne particulate matter. *Inhal. Toxicol.* 12, 121–135 (2000).

7. Cassee, F. R., Heroux, M.-E., Gerlofs-Nijland, M. E. & Kelly, F. J. Particulate matter beyond mass: recent health evidence on the role of fractions, chemical constituents and sources of emission. *Inhal. Toxicol.* 25, 802–812 (2013).

8. Viana, M. *et al.* Source apportionment of particulate matter in Europe: A review of methods and results. *J. Aerosol. Sci.* 39, 827–849 (2008).

9. Mahowald, N. M., Bryant, R. G., del Corral, J. & Steinberger, L. Ephemeral lakes and desert dust sources. *Geophys. Res. Lett.* 30, 1074 (2003).

10. Lough, G. C. *et al.* Emissions of metals associated with motor vehicle roadways. *Environ. Sci. Technol.* 39, 826–836 (2005).

11. Andreae, M. O. & Gelencsér, A. Black carbon or brown carbon? The nature of light-absorbing carbonaceous aerosols. *Atmos. Chem. Phys.* 6, 3131–3148 (2006).

12. Hoffmann, T. *et al.* Formation of organic aerosols from the oxidation of biogenic hydrocarbons. *J. Atmos. Chem.* 26, 189–222 (1997).

13. Belis, C. A., Karagulian, F., Larsen, B. R. & Hopke, P. K. Critical review and meta-analysis of ambient particulate matter source apportionment using receptor models in

Europe. *Atmos. Environ.* 69, 94–108 (2013).

14. Pant, P. & Harrison, R. M. Critical review of receptor modelling for particulate matter: A case study of India. *Atmos. Environ.* 49, 1–12 (2012).

15. Reff, A., Eberly, S. I. & Bhave, P. V. Receptor modeling of ambient particulate matter data using positive matrix factorization: review of existing methods. *J Air Waste Manag Assoc* 57, 146–154 (2007).

16. Mendez, M. *et al.* Modeling of the chemical composition of fine particulate matter: Development and performance assessment of EASYWRF-Chem. *Atmos. Res.* 170, 41–51 (2016).

17. Dubovik, O. *et al.* Retrieving global aerosol sources from satellites using inverse modeling. *Atmos. Chem. Phys.* 8, 209–250 (2008).

18. Yu, H. *et al.* Global view of aerosol vertical distributions from CALIPSO lidar measurements and GOCART simulations: Regional and seasonal variations. *J. Geophys. Res.-Atmos.* 115, D00H30 (2010).

19. Chu, S. H. PM2.5 episodes as observed in the speciation trends network. *Atmos. Environ.* 38, 5237–5246 (2004).

20. Zender, C. S., Bian, H. S. & Newman, D. Mineral Dust Entrainment and Deposition (DEAD) model: Description and 1990s dust climatology. *J. Geophys. Res.-Atmos.* 108, 4416 (2003).

21. Ginoux, P., Prospero, J. M., Gill, T. E., Hsu, N. C. & Zhao, M. Global-scale attribution of anthropogenic and natural dust sources and their emission rates based on MODIS Deep Blue aerosol products. *Rev. Geophys.* 50, RG3005 (2012).

22. Tegen, I. & Fung, I. Modeling of Mineral Dust in the Atmosphere - Sources, Transport, and Optical-Thickness. *J. Geophys. Res.-Atmos.* 99, 22897–22914 (1994).

23. Zhao, C. *et al.* Uncertainty in modeling dust mass balance and radiative forcing from size parameterization. *Atmos. Chem. Phys.* 13, 10733–10753 (2013).

24. Webb, N. P. & Pierre, C. Quantifying Anthropogenic Dust Emissions. *Earth's Future* 6, 286–295 (2018).

25. Reynolds, R. L. *et al.* Dust emission from wet and dry playas in the Mojave desert, USA. *Earth Surf. Process. Landf.* 32, 1811–1827 (2007).

26. Fifth Assessment Report - Synthesis Report. Available at: https://www.ipcc.ch/report/ar5/syr/. (Accessed: 20th June 2017)

27. Zhang, Q. *et al.* Ubiquity and dominance of oxygenated species in organic aerosols in anthropogenically-influenced Northern Hemisphere midlatitudes. *Geophys. Res. Lett.* 34, L13801 (2007).

28. Jimenez, J. L. *et al.* Evolution of Organic Aerosols in the Atmosphere. *Science* 326, 1525–1529 (2009).

29. Chacon-Madrid, H. J. & Donahue, N. M. Fragmentation vs. functionalization: chemical aging and organic aerosol formation. *Atmos. Chem. Phys.* 11, 10553–10563 (2011).

30. Seinfeld, J. H. & Pandis, S. N. *Atmospheric Chemistry and Physics: From Air Pollution to Climate Change*. (John Wiley & Sons, 2016).

31. Liu, P. F. *et al.* Ultraviolet and visible complex refractive indices of secondary organic material produced by photooxidation of the aromatic compounds toluene and m-xylene. *Atmos. Chem. Phys.* 15, 1435–1446 (2015).

32. Zhong, M. & Jang, M. Light absorption coefficient measurement of SOA using a UV–Visible spectrometer connected with an integrating sphere. *Atmospheric Environment* 45, 4263–4271 (2011).

33. Nakayama, T. *et al.* Laboratory studies on optical properties of secondary organic aerosols generated during the photooxidation of toluene and the ozonolysis of α-pinene. *J. Geophys. Res.* 115, D24204 (2010).

34. Sun, H., Biedermann, L. & Bond, T. C. Color of brown carbon: A model for ultraviolet and visible light absorption by organic carbon aerosol. *Geophys. Res. Lett.* 34, L17813 (2007).

35. Liu, S. *et al.* Hydrolysis of Organonitrate Functional Groups in Aerosol Particles. *Aerosol Science and Technology* 46, 1359–1369 (2012).

36. Nakayama, T. *et al.* Wavelength Dependence of Refractive Index of Secondary Organic Aerosols Generated during the Ozonolysis and Photooxidation of α-Pinene. *Sola* 8, 119–123 (2012).

37. Lu, J. W., Flores, J. M., Lavi, A., Abo-Riziq, A. & Rudich, Y. Changes in the optical properties of benzo[a]pyrene-coated aerosols upon heterogeneous reactions with NO2 and NO3. *Phys. Chem. Chem. Phys.* 13, 6484–6492 (2011).

38. Jacobson, M. Z. Isolating nitrated and aromatic aerosols and nitrated aromatic gases as sources of ultraviolet light absorption. *J. Geophys. Res.* 104, 3527–3542 (1999).

39. Claeys, M. *et al.* Chemical characterisation of humic-like substances from urban, rural and tropical biomass burning environments using liquid chromatography with UV/vis photodiode array detection and electrospray ionisation mass spectrometry. *Environ. Chem.* 9, 273–284 (2012).

40. Desyaterik, Y. *et al.* Speciation of "brown" carbon in cloud water impacted by agricultural biomass burning in eastern China. *J. Geophys. Res. Atmos.* 118, 7389–7399 (2013).

Chapter 2: The Effect of a Receding Saline Lake (The Salton Sea) on Airborne Particulate Matter Composition

2.0 Acknowledgement of Co-Authorship

This work was completed with contributions from Alexander L. Frie, Justin H. Dingle, Samantha C. Ying, and Roya Bahreini.

2.1 Introduction

The Salton Sea is an endorheic, saline lake, located in the southwest of the United States. The Sea has been intermittently filled with water on geological time scales and was last filled through an accidental diversion of the Colorado River in 1905.[1] For the past century, inflows dominated by agricultural runoff and municipal effluent maintained Salton Sea water levels. In 2003, the Quantification Settlement Agreement (QSA) incentivized agricultural water conservation in the region, resulting in a decrease in runoff inputs to the Sea. As part of the QSA, additional water diverted from the Colorado River is directed into the Sea to replace inflow reductions. The diversion of river water is scheduled to end before 2018, and the decrease of inflow is predicted to cause a significant decline in water level between 2018 and 2030.[2] This drop will expose large areas of dry lakebed (playa), potentially creating a vast area of highly emissive surfaces in a county that is already classified as nonattainment for particulate matter with aerodynamic diameters ≤ 10 μm (PM_{10}).[3] Due to drought, large areas of playa are already exposed and are acting as dust sources with an unknown effect on PM mass or composition.

Globally, dust emissions from exposed playas have negatively affected air quality in areas including Owens Lake, California, Sevier Lake, Utah, and the Aral Sea, Uzbekistan

and Kazakhstan.[4,5,6] Playas have a high potential to act as dust sources because playa surfaces are often unvegetated and typically have elevated levels of subsurface capillary action that generate irregular and emissive salt crusts.[7] The dust emissions from playas increase airborne particulate matter (PM) mass and raise health concerns, as increases in PM mass have been linked to cardiovascular disease, respiratory disease, and mortality.[8] In addition to increased mass loadings, the composition of PM emissions could increase particulate toxicity. [9,10,11] There is concern that metals and pesticides from Salton Sea sediments may be suspended in dust and increase PM toxicity; selenium, cadmium, molybdenum, nickel, and zinc and have all been previously observed at levels of ecological concern within Salton Sea Sediments.[12,13] Additionally, in other playas contaminants have been observed to accumulate after desiccation, potentially intensifying the toxicity of emissions. For example, at Owens Lake and Ash Meadows, accumulation of As has been observed in near-surface sediments and dust emissions.[4,14] PM sourced from playas is thought to be compositionally distinct from PM sourced from other dust sources, but the magnitude of changes to bulk PM composition has not been investigated at the Salton Sea or in other major playa systems.

Here we test the hypothesis that emissions from playas change PM_{10} composition near the Salton Sea, potentially influencing toxicity, dust microphysical processes, and nutrient deposition. We assess the composition of playa soils, desert soils, and PM_{10} collected at the Salton Sea during August 2015 and February 2016. Major sources of PM are identified using enrichment factors and positive matrix factorization (PMF), and the mass contribution of desert dust and playa dust sources are estimated.

2.2 Methodology and Approach

2.2.1 Sampling

The locations of all aerosol and soil sampling sites are shown in Figure A1.1 of Supplementary Information (SI). Aerosol samples were collected at Salton City (33.27275°N, -115.90062°W), CA and Bombay Beach (33.35264°N, -115.73419), CA, two population centers along the coast of the Salton Sea. These sites were chosen due to their proximity to the Salton Sea and the presence of Imperial Irrigation District (IID) air quality monitoring stations, which enabled easy sample collection and access to bulk PM_{10}, wind speed, wind direction, relative humidity (RH), and temperature data. Meteorological data were obtained from the California Environmental Protection Agency's, Air Resources Board, Air Quality and Meteorology Information System.[15] Aerosol samples were collected at Salton City (SC) during Aug. 22-27, 2015 (SCS) and Feb. 12-19, 2016 (SCW) and at Bombay Beach (BB) during Aug. 27-31, 2015 (BBS). During both sampling periods, the Salton Sea water level averaged ~71.4 m below sea level, corresponding to about 15,000 acres of exposed playa relative to year 2000 levels.[2,16] Aerosol samples were collected in two sets to capture the influence of different daily wind patterns: a day set between 08:00 LT (local time) and 18:00 LT and a night set between 19:00 LT and 07:00 LT. All samples were collected by a Micro-Orifice Uniform Deposition Impactor (MOUDI) sampler, which separates and collects aerosols by size into 11 stages, between 0.056-18 μm, onto 47 mm, 0.2 μm pore diameter, Pall Zefluor PTFE filters. During sampling, three summer and two winter sets of field blanks were also collected. Pre- and post-sampling, filters were kept in acid-washed Petri dishes and stored individually in anti-

static bags. Data from the night of August 24th and the day of Aug. 25th were not included due to water condensation within the MOUDI.

A total of 25 playa and 88 desert samples were collected from a wide area around the Salton Sea. Playa sites are characterized by a lack of vegetation and were recently submerged underneath the Salton Sea, whereas Desert sites are located farther from the sea. Soils were collected by sampling the top 1 cm layer of the surface soil- the section that would most likely undergo suspension. Soils were stored in quart Ziploc bags and left open to air dry at 22°C.

2.2.2 Filter Digestion and Elemental Analysis

Soil (seven playa and ten desert) and aerosol samples were acid digested to determine total metal and metalloid concentrations for enrichment factor calculations and as inputs for the PMF model. For soil samples, a small mass of soil (~500 µg) was digested. To increase the signal to noise ratio within aerosol samples, MOUDI filters in the following size ranges were combined for analysis: 0.056-0.18 µm, 0.18 - 0.56 µm, 1.0 - 3.2 µm, 3.2 - 10 µm. Filters collected in the size range of 0.56- 1.0 µm were analyzed individually. Filters with particles greater than 10 µm were excluded due to high field blank values. A two-step digestion was performed using HNO_3 + HF and aqua regia (i.e., HNO_3 + HCl). All acids were sourced from Fisher Chemical and were trace metal grade or better. For each digest, elemental concentrations of the following elements were determined by inductively coupled plasma mass spectroscopy (ICP-MS) (Agilent 7900): Ca, Na, As, Al, Cr, Fe, Mn, Ni, V, Ba, Cd, Co, Se, Ti, K. All analysis was performed using the summed concentrations of extracts from each period to get PM_{10} elemental concentrations. A more

detailed description of the digestion procedure and quantification steps is included in appendix 1.

2.2.3 X-ray Fluorescence Spectroscopy

To confirm representativeness of the smaller sample set analyzed by ICP-MS, a total of 113 soil samples (25 Playa and 88 Desert) were analyzed using energy dispersive X-ray fluorescence (ED-XRF) spectroscopy (SPECTRO XEPOS) to determine total solid phase Na, Al, K, Ca, Ti, V, Cr, Fe, As, Co, and Se concentrations. ED-XRF is commonly used as a high-throughput method to measure total elemental composition in solid phase samples and is useful for investigating overall trends in larger sample sets. ED-XRF was used here as a high throughput method to provide a more representative characterization of both playa and desert samples and to increase confidence in any differences observed between the two soil classifications. A more detailed description of the quantification steps is included in the appendix 1.

2.2.4 Enrichment Factors

Enrichment factors (EF) have been used widely in atmospheric and soil literature to track normalized changes in composition that are driven by anthropogenic or geologic forces.[17,18,5] Enrichment factors are often used to track anthropogenic contamination within PM and soils, but can also be used to monitor natural enrichment and fractionation processes. Mineralogical and chemical transformations can also lead to variations in EFs reflective of specific environmental conditions; thus, interpretation of EF results must be made within the context of the environmental conditions where samples were collected.[19] For this study, Al is used as the normalization element because it is relatively immobile in

soils and has been shown to be conserved upon emission. EF in soils and aerosol samples were calculated via:

$$EF = \frac{(M_{Measured}/Al_{Measured})}{(M_{UCC}/Al_{UCC})} \quad (2.1)$$

where $M_{measured}$ is the ICP-MS measured mass concentration of an element within a sample (ppm), $Al_{measured}$ is the ICP-MS measured mass concentration of Al within a sample (ppm), and M_{UCC} and Al_{UCC} are the analogous values for the Upper Continental Crust composition (UCC), as reported by Wedepohl.[20] Samples with enrichment factors of 1 have the same elemental ratios as UCC; values greater than or less than 1 indicate differences from the UCC.

2.2.5 Positive Matrix Factorization (PMF)

EPA's Positive matrix factorization (PMF 5.0) is a statistical method that uses factor analysis to determine the contribution of different sources to the measured elements at a receptor site. Unlike principle component analysis, PMF effectively only allows positive values, allowing small negative factor contributions (>-0.2) only to increase the goodness of the model fit. This allows PMF to be applied to environmental data, where negative contributions are not physically meaningful. For PMF, both data and uncertainty matrices are input into the model. The inclusion of an uncertainty matrix allows the PMF model to provide weights to samples by their signal-to-noise (S/N) ratio and reduce weighting of highly uncertain inputs. More detail about EPA PMF 5.0 can be found in Paatero and Tapper, Paatero, and Brown et al.[21,22,23] An extended description of the PMF parameters used for this study is included in the appendix 1.

2.3 Results and Discussion

2.3.1 Meteorological Data

Meteorological data provide an external context for PM measurements, as meteorological factors directly influence playa and desert emissions. For example, humidity and temperature changes can shift hydration states of playa minerals and influence their emissivity.[24] Additionally, wind direction and speed determine strength and likelihood of detection of emissions from specific sources.

Relative humidity (RH) at the sampling sites showed common diurnal variations, with a maximum RH observed in the early morning and a minimum RH in the afternoon (Figures A1.2a and A1.3). However, the magnitude and range of RH oscillation varied between sampling periods. During Bombay Beach Summer (BBS), Salton City Summer (SCS), and Salton City Winter (SCW) the average daily RH oscillation between 06:00 LT and 15:00 LT was 28.9 %, 18.0 %, and 10.7 %, respectively. The magnitude of RH oscillations is important as larger oscillations lead to larger hydration/dehydration shifts within the evaporite minerals of playa surfaces, weakening salt crusts and increasing emissivity. Given this, playa emissions could be higher during BBS and SCS relative to SCW.

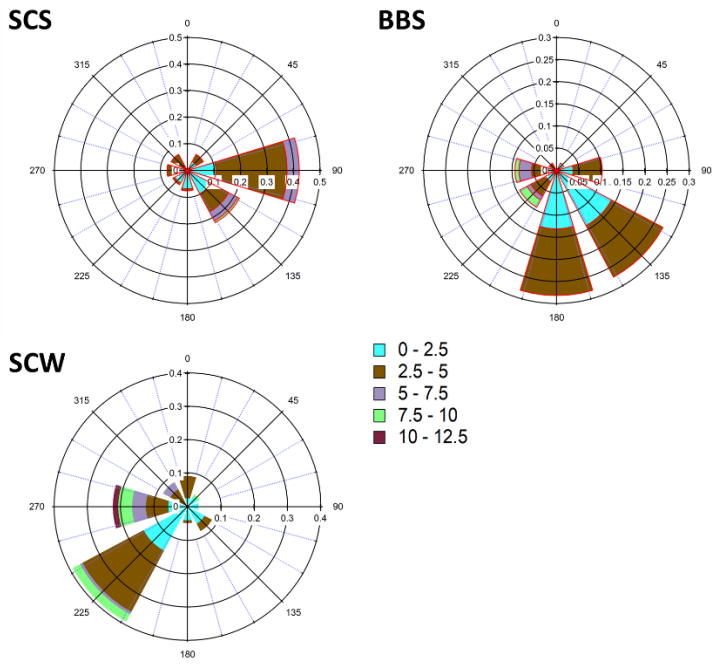

Figure 2.1. Wind roses for sampling periods Salton Sea Summer (SCS), Salton Sea Winter (SCW) and Bombay Beach Summer (BBS). Axis values represent the probability of wind being sourced from an octant and colors represent wind speed in m s^{-1}.

For wind direction analysis, directions were divided into 8 octants (North, Northeast, East, etc.) and probability of wind being sourced from each octant was calculated (Figures 2.1). Wind direction displayed a clear diurnal trend at all sites (Figures A1.4-S1.6). Additional discussion of these trends can be found in the appendix 1. It should be noted that the predominant wind directions during day BBS, day SCS, and night BBS were consistent with air masses passing over the Salton Sea and/or playas if a short-term linear path is assumed. If playa emissions were occurring, playa chemical signatures should be observable within samples collected during BBS and SCS. Conversely, the predominant wind directions during SCW would not directly cross the Salton Sea and playa, so playa emissions are not expected to be observed frequently during this period.

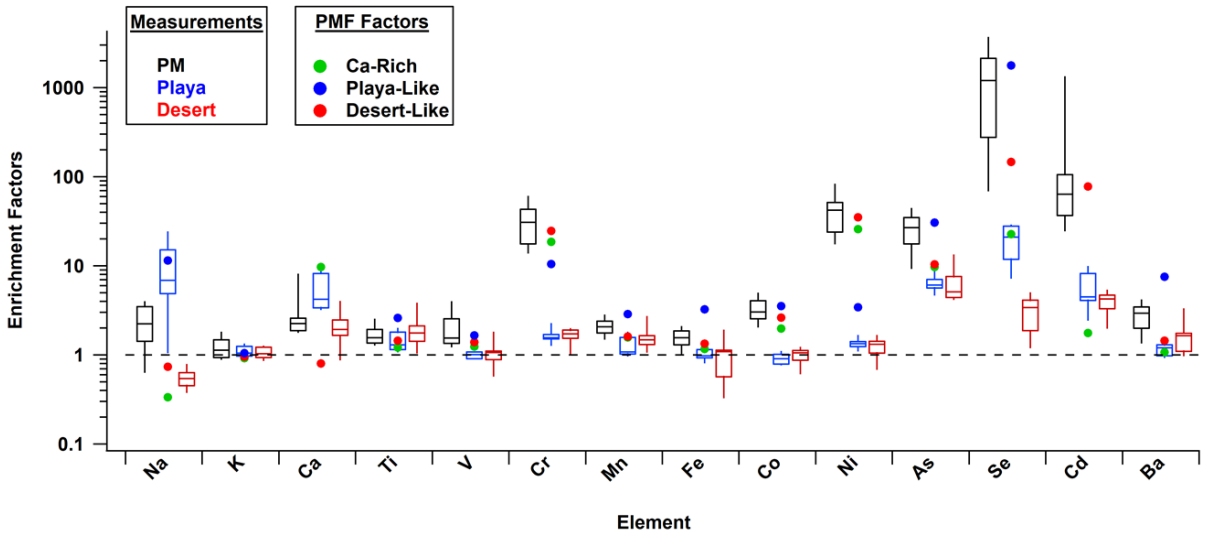

Figure 2.2. Enrichment factor distributions for each element from measurements of PM_{10} (black), playa soils (blue), and desert soils (red). Box and whiskers highlight 10th, 25th, 50th, 75th, and 90th percentiles. Respective EFs of the PMF modeled Ca-rich (green dots), playa-like (blue dots), and desert-like (red dots) factors superimposed. EF of the Se factor was not graphed because low Al attributions create non-meaningful EFs.

Median, hourly-averaged, wind speed was 2.55 m s^{-1}, 2.62 m s^{-1}, and 3.2 m s^{-1} for SCS, BBS, and SCW, respectively. SCW wind speed populations (Figures A1.2c) were skewed towards higher values due to short-term, high wind speed events occurring on 2/14/16 and 2/18/16. No significant wind speed differences were observed between day and night periods for SCW and BBS, but a significant difference was observed for SCS. For SCS, median day and night wind speeds were 3.2 m s^{-1} and 1.3 m s^{-1}, respectively.

2.3.2 Soils Characteristics

ED-XRF and ICP-MS elemental analysis revealed consistent and unique characteristics of playa and desert soils (Table A1.1 and A1.2). For both techniques, playa soils were observed to have significantly ($p \leq 0.05$) larger elemental abundances of Na, Ca,

and Se and desert soils were observed to have significantly larger abundances of Ti and Mn. The larger ED-XRF dataset also revealed significantly greater abundances of Al, Fe, K, V, and Cr within desert soils. Notably, arsenic was not significantly different between playa and desert soils using either techniques, and Cd was observed at near or below detection limits of both techniques. Given these trends, increased emissions of PM from playas are expected to increase abundances of Na, Ca, and Se in dust particles relative to typical desert soil emissions. Because of the observed consistencies in ED-XRF and ICP-MS analysis of the samples, and to allow intercomparison with the PM data, only ICP-MS data were used for EF calculations.

2.3.3 PM_{10} Data

Median, hourly PM_{10} mass concentrations from tapered element oscillating microbalance (TEOM) (Thermo-scientific, SER 1400) measurements during BBS, SCS, and SCW were respectively 28.7 μg m^{-3}, 23.3 μg m^{-3}, and 15.6 μg m^{-3} (Figures A1.7). Summer (BBS and SCS) PM_{10} concentrations were significantly ($p \leq 0.05$) higher than winter (SCW). Baseline concentrations were lower during winter months, but during SCW, two high mass events were observed on 2/18/16 and 2/14/16, skewing the distribution towards higher mass concentrations, likely due to higher wind speeds observed on these days. Significant diurnal variability in PM_{10} mass concentration was only observed during SCS, with median loadings of 25.7 μg m^{-3} and 20.4 μg m^{-3} (Figures A1.8) for night and day, respectively.

2.3.4 Elemental Mass Concentrations

PM_{10} median mass concentrations of elements measured via ICP-MS are included in Table A1.3. Mass concentrations of major elements (Al, Fe, Na, and Ca) were found to be within the range of previously observed values in rural areas of the American southwest.[25,26] Daytime vs. nighttime trends at the two sampling sites are not explicitly discussed because they were not qualitatively different.

Although trace elements, e.g., Cd, Se, Cr, As, Mn, and Ni, do not significantly increase the mass of PM, their concentrations are of interest due to their potential to increase toxicity. Median mass concentrations of each of these metals were below California EPA reference exposure levels (RELs) for chronic toxicity, by factors of 77, 14,000, 18, 250, 7, and 2 respectively (Table A1.3).[27] Nickel was the only element to breach its REL during sampling, during 3 of the 25 sampling periods. This suggests that PM mass increases may be the first health concern driven by playa emissions until individual elemental limits are surpassed. The disconnect between sediment contamination and atmospheric PM toxicity likely arises from the different pathways driving PM human toxicity and sediment-driven aquatic toxicity. The metals previously observed at levels of ecological concern in sediments were classified as such, in part, because of their ability to bioaccumulate within aquatic systems.[13,12,28] Conversely, PM toxicity is driven by size and composition of PM,[29] not compounding within the food chain. The crusts that form on playas are not simply dried sediments, but instead are new structures with high concentrations of evaporite minerals.[14,7] Therefore, the presence of contaminants within sediments does not always equate to toxic playas or atmospheric emissions.

Only Na and Se displayed significant differences ($p \leq 0.05$) between summer (SCS+BBS) and winter (SCW) sampling (Table A1.3). Average Na concentrations were 850 ± 670 ng m^{-3} and 370 ± 159 ng m^{-3} during the summer and winter, respectively. PM_{10} Na and its seasonality is discussed further in the discussion of EFs (Section 2.3.3.2). Average Se concentrations were 2.1 ± 2.7 ng m^{-3} in summer and 0.3 ± 0.4 ng m^{-3} in winter. Possible drivers of Se seasonality are discussed in section 2.3.4.

2.3.5 Enrichment Factors (EFs)

EF distributions for playa soil, desert soil, and PM_{10} are shown in Figure 2.2 and values are provided in Table A1.4. Playa soils were significantly ($p \leq 0.05$) more enriched in Na, Ca, Se than desert soils. Increased concentrations of these elements have previously been observed within Salton Sea sediments and waters;[30,31,13] these elements were likely deposited during the playa formation.

PM_{10} was significantly more enriched than both soil types in Se, V, Cr, Ni, As, Ba and Fe. Enrichment of the minor elements has been previously observed during simulated suspension of soil in the laboratory.[5,32] A soil suspension enrichment may have contributed to the observed enrichments in PM_{10}. As shown in Figure 2.3, minor and trace elements in PM_{10} were concentrated on smaller particles while crustal elements (Fe, Al, Ca, Ti) were concentrated on larger particles. Anthropogenic sources including vehicles (Fe, Pb, V), incinerators (Ni, As), biomass burning (K, Zn) and coal combustion (Se, Pb) are also possible contributors to metal enrichment.[33,13,34,35] Iron was the only major element significantly enriched in PM_{10} relative to both soil types. Traffic emissions present one possible source of Fe enrichment, as Fe has been observed in brake pad and vehicular

emissions.[36,37]A combination of suspension enrichment and anthropogenic contributions are reflected in the enrichments of PM_{10}.

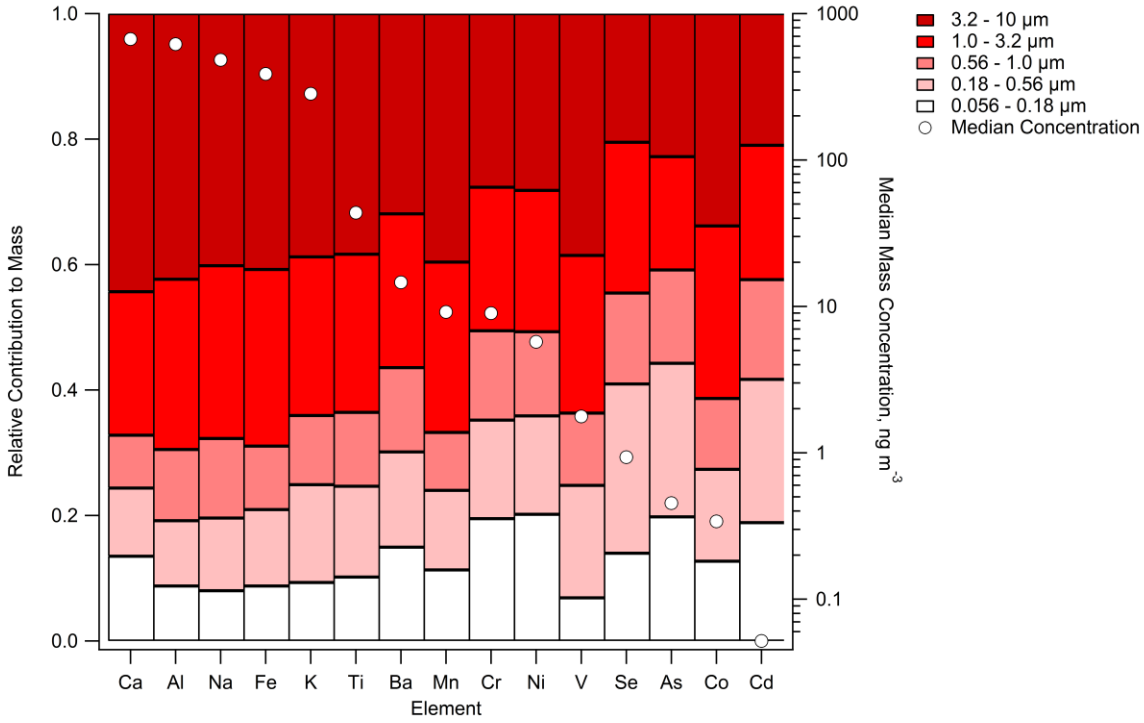

Figure 2.3. Relative mass contribution of different size classes of aerosols to individual elements (left axis) and median mass concentrations of individual elements (right axis).

PM_{10} was significantly enriched in Na relative to desert soils, but not playa soils. PM_{10} Na concentration is of interest because Na containing minerals including, but not limited to, halite (NaCl) have been observed in high concentrations within playas.[24,38,39] This study also observed Salton Sea playas with significantly ($p \leq 0.05$) higher Na concentrations than local desert soil (Section 2.3.2). Emissions from playa areas are expected to have relatively high Na concentrations, so Na can be utilized as a tracer for these emissions. PM_{10} Na enrichment may arise from mixing of two sources, i.e., playa and desert soil. This enrichment suggests that playa emissions are contributing significantly to

the Na within PM_{10}. The percentage of sodium attributed to playa emissions is discussed in section 2.3.5.

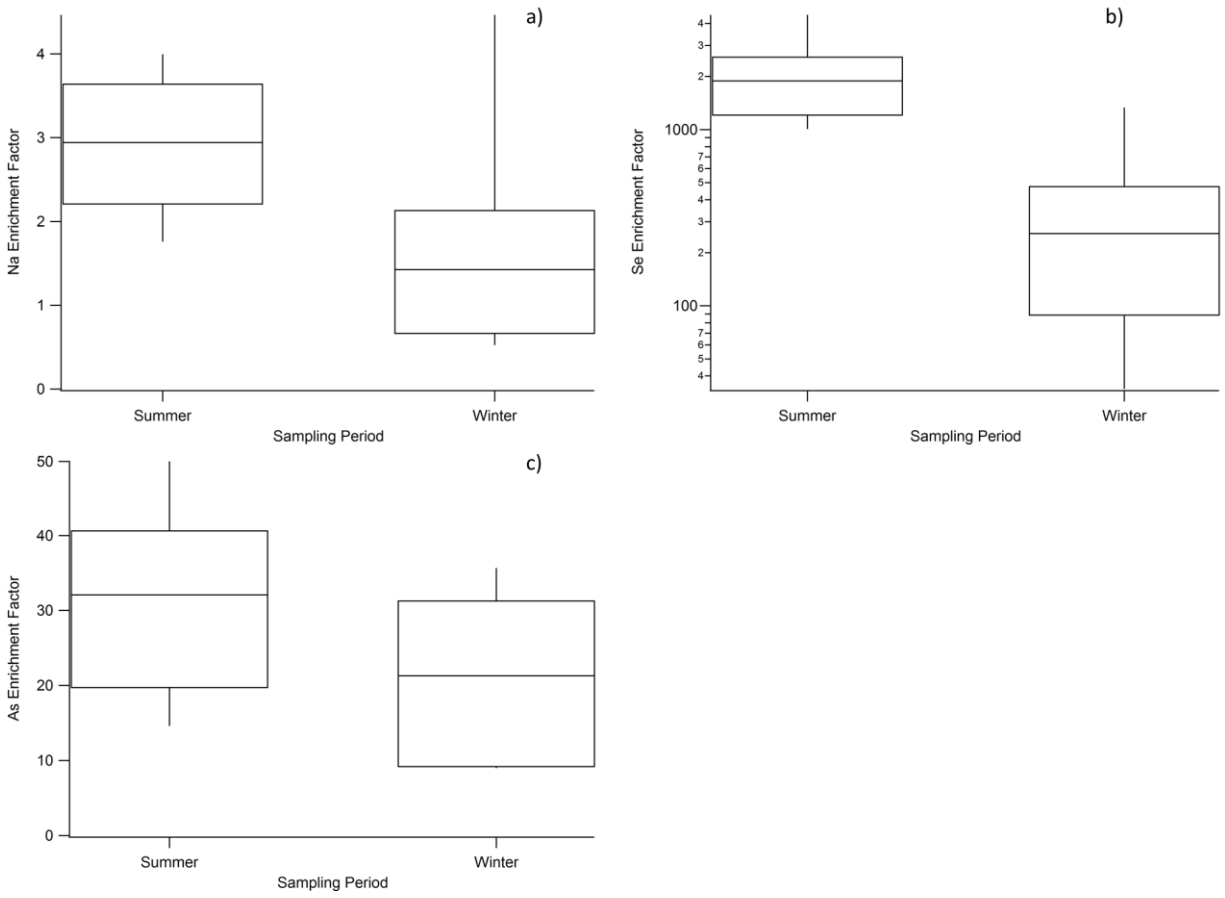

Figure 2.4. PM_{10} EF distributions of (a) sodium, (b) selenium, and (c) arsenic- elements with significant seasonal differences in EF distribution. Box and whiskers highlight 10^{th}, 25^{th}, 50^{th}, 75^{th}, and 90^{th} percentiles.

Summer (SCS+BBS) PM_{10} EFs were significantly greater than winter (SCW) for Se, Na, and As (Figure 2.4). The lack of a seasonal pattern in the EFs of major elements other than Na suggest that separate factors control the emissions of Na compared to other

major crustal elements. This would be expected if the Na was sourced from playa, as playa emissions are thought to be influenced by additional meteorological factors such as RH,[24] while dust emissions from non-playa sources are not.[40] Higher Na EFs during summer samplings are consistent with wind direction and RH observations, as wind directions during both SCS and BBS were predominantly from the direction of playas and larger diurnal RH oscillations were observed during these periods. Oscillations in RH are thought to affect the hydration state of playas, increasing irregularity in mineral structure and potentially increasing emissivity. Na EFs were weakly correlated with EFs of Se ($r=0.5$, $p=0.01$) and As ($r=0.4$, $p=0.04$), indicating a large proportion of Se and As were likely emitted from sources separate than those of Na. Selenium displayed the largest enrichment among the trace elements in PM_{10} and the strongest seasonal dependence: median summer and winter Se PM_{10} EFs were 1890 and 257, respectively.

2.3.6 Positive Matrix Factorization (PMF)

The four source factors produced by PMF, using precedents set previously in published source studies and knowledge of potential sources in the area, were identified as playa-like, desert-like, Se, and Ca-rich. Profiles of these factors are shown in Figure 2.5. Notably, elements normally associated with anthropogenic emissions (such V, As, Ni, Cr, and Ba), which were observed to be enriched in PM relative to playa and desert soils, were not isolated in an independent factor. This is likely due to the low concentrations and relatively high uncertainties associated with these elements.

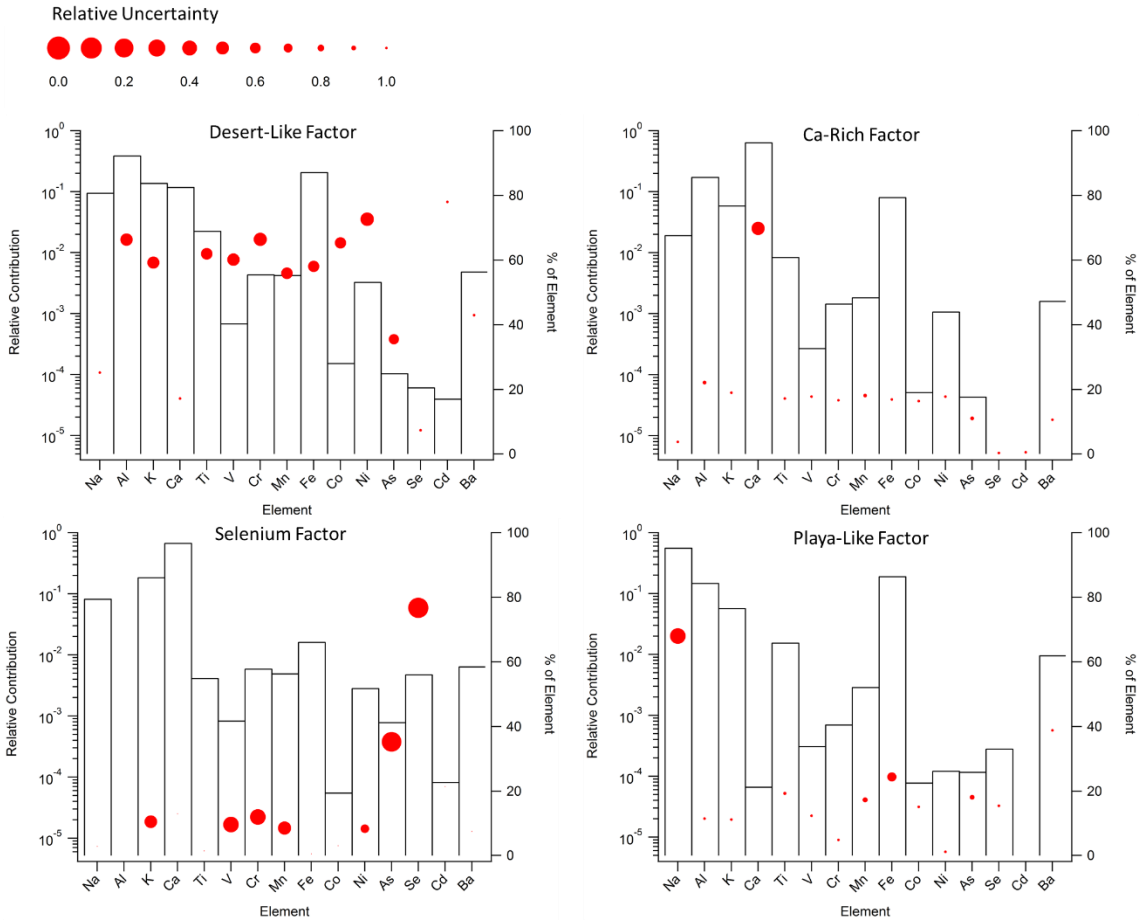

Figure 2.5. Positive matrix factorization (PMF) factor profiles, with the relative contribution of elements on the left axis, represented by bars, and the percentage of each element accounted for by a factor on the right axis, represented by red dots. The size of the red dots is inversely proportional to the relative uncertainty, and represents the confidence in the percentage mass of each element accounted for by each factor, with larger dots representing more confident attributions. The uncertainty is calculated by the displacement method.

The playa-like factor was characterized by a prominence of Na and the presence of dust tracers such as Fe, K, and Ti. The Na and K EFs of the playa factor were also within the distribution of EFs observed for playa soils, although EFs of other elements were higher than those observed in playa soils. These high enrichments likely arise from the high uncertainty in the attribution of elements other than Na to this factor. The playa-like factor is similar to sea spray factors, typically dominated by high concentrations of Na and/or Cl, observed in other PMF studies.[41,42] Here, the playa-like factor is not believed to be sea

spray as conditions for white-cap formation, i.e., wind speeds greater than 4 ms^{-1}, were not observed in high frequency during any sampling period, except for SCW.[43] On average, the playa-like factor contributed the least to samples from the SCW period when higher wind speeds were occasionally observed, suggesting a source different than sea spray. Furthermore, if sea spray were an important source, PM_{10} EFs of Na would be expected to be higher than those observed in the playa on at least some of the sampling days, but this was not observed. Similar to trends observed within the PM_{10} EF of Na, the contribution of the playa-like factor was higher on sampling days with the wind blowing over playa surfaces.

The desert-like factor was identified by the prominence of Al, Fe, K, and Ti, all of which are major elements in the Earth's crust and have been observed to be prominent in regional deserts' soils (Section 2.3.1)[20], and have been associated with crustal emissions in previous PMF studies.[44,45,46] Observation of a desert-like factor is expected because dust sourced from desert surfaces is thought to be a large component of PM mass in the rural southwest.[25,26] The desert-like factor's EFs of major elements (Na, K, Ti, Mn, Fe) was within the distribution of EFs for sampled desert soils (Figure 2.2), further supporting the conclusion that this factor represents the contribution of local soils. Notably, the desert-like factor was much more enriched in Co, Ni, Se, Cd, and Cr than the desert sample set (Figure 2.2); this likely occurs because no separate anthropogenic source was resolved. These elements are commonly associated with traffic, industry, and incineration and should not be interpreted as being sourced from natural dust emissions.

The Ca-rich factor is similar to Ca factors found in previous source apportionment studies and often attributed to construction or resuspension of road dust.[47,48] The sampling sites were close to population centers and an off-road vehicle park, so it is possible that anthropogenic activity also contributed to this factor. Additionally, other studies have attributed Ca-rich factors to secondary dust sources, such as limestone or gypsum deposits.[49,50] The Salton Sea and surrounding areas are found in the basin of the ancient lake Cahuilla, and the lacustrine deposits could contribute to a secondary dust source and this factor. Gypsum and other Ca-containing minerals are also present within Salton Sea playas,[24] but on days when the Ca-rich factor was most prominent, wind direction was not predominantly from the direction of the Salton Sea. These observations suggest that Salton Sea playas are not the major source of the Ca-rich factor and that it is likely a combination of anthropogenic and natural Ca sources.

The Se factor was identified by the prominence of Se; 77% of all sampled Se is attributed to this factor. Given that coal combustion is the major anthropogenic source of Se and the lack of coal usage in this region, the Se factor was likely not anthropogenic in nature. One potential Se source is Se volatilization and condensation onto PM.[51] High levels of Se volatilization would explain both the source independence and seasonal variability observed in Se PM mass concentrations, EFs, and the Se factor. Se volatilization has been previously observed in submerged sediments and capillary fringe soils, like those found in the subsurface of the playas.[52,53,54,55] Previous observations of Se volatilization report strong seasonal variability, with the highest rates of volatilization occurring during summer months. Summer median Se EFs were seven times greater than winter, suggesting

that Se volatilization from the sediments/soil and condensation onto PM is an important process at the Salton Sea. Previous investigations of Se volatilization at the Salton Sea by Schroeder et al. (2002) reported gradients of volatile Se species occurring within the water column, providing evidence that volatilization within sediments was occurring.[31] Despite this, Se volatilization from sediments was not previously thought to play a large role in the Salton Sea Se budget and mass balanced was achieved accounting for Se only within the aqueous phase, sediments, and biomass. If Salton Sea playa zones have a greater rate of Se volatilization than Salton Sea sediments, volatilization may become increasingly important during the exposure of playas. These data reveal that Se dynamics at Salton Sea need to be further investigated, as volatilization pathways may be stronger than previously estimated. These findings may have implications for the Salton Sea restoration plans.

2.3.7 Two-source Mixing Model and Na Attribution

If playa and desert sources are the dominant sources of Na and Al in PM at the Salton Sea, it is possible to construct a simple two source mixing model (TSM). Using the median playa and desert soil EFs as end points, the contribution of each respective source to Na can be estimated via :

$$EF_{PM} = EF_{Playa}(X) + EF_{Desert}\,(1 - X) \qquad (2.2)$$

where EF_{PM} is the observed Na EF for a sample within PM_{10}, EF_{playa} is the median Na EF of playa soils (6.9, standard deviation (SD) = 7.8) and EF_{desert} is the median Na EF of desert soils (0.54, SD = 0.13). X is the percentage of PM_{10} Na attributed to playa sources during a given sampling period.

TSM-based playa Na concentrations correlate very well (r=0.96, p=1.4E-14) with the playa-like Na concentrations from PMF. A high correlation between playa Na concentrations estimated by TSM and PMF confirm that a two-source system of soils and playa, and not sea salt, indeed controls the PM_{10} Na concentrations in the basin. Despite high correlations, TSM estimates lower sodium emissions from Playa (38% of PM_{10} Na) than PMF (~68% of PM_{10} Na). It is possible that TSM underestimates the playa contribution to Na as EF_{playa} is highly variable (SD=7.8). To match the TSM and PMF-based estimates of playa contributions to Na, EF_{playa} in equation 2.2 needs to be lowered to 4.2, which is still within the observed range of Na $EF_{playa.}$ The large variation in playa composition likely leads to a similarly large distribution of playa emission potentials and compositions. Therefore, the effective Na EF_{playa} of 4.2 may in fact be a more representative value of the Na EF of emissive playas.

2.3.8 Crustal and Playa Contributions to PM_{10}

To quantify the burden of PM_{10} emission sources at Salton Sea, the mass contributions of major sources need to be calculated. Elemental masses do not represent the complete mass represented by a factor, especially for mineral-based factors like the playa-like, desert-like, and Ca-rich factors because the digestion and analysis method could not measure bulk Si-, O-, N-, or C-based species. Despite this, PM mass associated with the Desert-like factor can be estimated using the elemental concentration of Al, Ca, Fe, and Ti in dusts and the formulation from the Interagency Monitoring of Protected Visual Environments (IMPROVE) program and modified by Clements et al.[56,57,58,25]

$$Crustal\ Mass = 10.92\ (Al) + 1.63\ (Ca) + 2.42\ (Fe) + 1.94\ (Ti) \quad (2.3)$$

where *Crustal Mass* is the PM_{10} mass concentration from crustal sources and *Al*, *Ca*, *Fe*, and *Ti* are the elemental mass concentrations of each element observed in PM_{10}. Using this method, and averaging over the sampling periods, the average crustal contribution was 45.2 ± 26.4% (13 ± 10 μg m^{-3}) of the total PM_{10} mass, as measured by the IID, indicating that on most days crustal sources played a major role in the observed PM_{10} mass loadings at these sites.

An integral goal of this study was to determine the PM_{10} mass contribution of playa sources around Salton Sea. No analogous equation exists to estimate playa contributions, in part because playa composition is variable between sites. Here, an equation was developed using our PMF results and the playa mineral frequencies described by Buck et al (2011).[24] Assuming this subset is representative of emissive playa areas around the Salton Sea, the ratio of Na to total mineral mass of a typical playa can be calculated. Next, using the PMF estimated Na concentration of the playa-like factor, the PM_{10} mass contribution of playa sources can be estimated by:

$$Playa\ Mass = k * Na_{Playa} \quad (2.4)$$

where *Playa Mass* is the PM_{10} mass concentration sourced from playas on a given day, *k* is 5.22 and represents the ratio of total playa mass to Na mass as observed by Buck et al. (2011), and Na_{Playa} is the mass concentration of Na that was attributed to playa sources by PMF on the day of interest. Using this estimation, playa sources contributed at an average of 8.9 ± 5.6%, (2.2 ±1.6 μg m^{-1}) to PM_{10} mass over all sampling periods. Although highly

variable, average summertime contribution of playa sources to PM_{10} mass at both sites was higher than in winter (11.9 ± 11.4 % vs. 5.13 ± 5.8%). The contribution of playa to PM at these sites is not negligible, but measurable at current levels of playa exposure. These contributions will likely increase with increasing exposures of the shoreline.

High dust emission events with prevailing winds crossing over the exposed playas were not sampled during this campaign. Since PM dust emissions caused by wind erosion are controlled in part by wind speed and the presence of saltating particles, playa emission rates are expected to increase under higher wind conditions. Therefore, the observations here may only represent the lower bounds of current playa contributions to PM_{10}. Future PM source apportionment studies need to resolve the contributions of playa areas during high mass events, as these contributions will likely be increasingly more important as the Salton Sea recedes and shoreline exposures grow in extent.

Notably, our results do not support that concept that playa emissions or PM in this region, are exceptionally toxic due to high levels of toxic metals (Section 2.3.3.1). Despite this, both TSM and PMF results provide evidence for a relatively strong impact of playa on PM Na concentrations and PM_{10} mass loadings. Such emissions could influence downwind biogeochemical and atmospheric processes and affect ecology and meteorology in downwind regions. For example, Na deposited in soils can influence biomass decomposition and perturb plant nutrient balance.[59,60] While suspended as PM, Na can also impact cloud formation.[61] With recent playa exposures in other regions, e.g., the Great Salt Lake in southwest U.S.A.,[62] Ebinur Lake in northern China,[63] and Lake Urmia in Iran,[64]

methodologies applied here can be used to determine PM compositional shifts and estimate the impact of playa exposures on PM concentration due to changes in lake size.

2.5 Appendix Information: Appendix 1 contains detailed methodology concerning digestions, ED-XRF and PMF; descriptions of temperature and wind conditions; Tables A1.1-A1.4: summary tables of elemental measurements and EFs; Figures A1.1-A1.10: map of sampling locations; multiple graphics presenting meteorological conditions; comparison of PMF EFs to measurement EFs

2.6 Works Cited

1. Babcock, E. A.; Geology of the Northeast Margin of the Salton Trough, Salton Sea, California. *Geological Soc. of Am. Bull*. 1974, 85, 321–332; DOI 10.1130/0016-7606

2. Cohen, M. *Hazard's Toll: The Costs of Inaction at the Salton Sea*, Pacific Institute: Oakland, CA, 2014

3. *US EPA, Green Book* Website; https://www.epa.gov/green-book

4. Reheis, M. C., Budahn, J. R., Lamothe, P. J., and Reynolds, R. L. Compositions of modern dust and surface sediments in the Desert Southwest, United States. *J. Geophys. Res-Earth* 2009, 114, F01028; DOI 10.1029/2008JF001009

5. Hahnenberger, M., and Perry, K. D. Chemical comparison of dust and soil from the Sevier Dry Lake, UT, USA, *Atmos. Environ.* 2015, 113, 90–97; DOI 10.1016/j.atmosenv.2015.04.054

6. Indoitu, R., Kozhoridze, G., Batyrbaeva, M., Vitkovskaya, I., Orlovsky, N., Blumberg, D., and Orlovsky, L. Dust emission and environmental changes in the dried bottom of the Aral Sea, *Aeolian Research* 2015, 17, 101-115; DOI 10.1016/j.aeolia.2015.02.004

7. Reynolds, R. L., Yount, J. C., Reheis, M., Goldstein, H., Chavez, P., Fulton, R., Whitney, J., Fuller, C., Forester, R. M. Dust emission from wet and dry playas in the Mojave Desert, USA. *Earth Surf. Proc. Land* 2007, 32, 1811–1827; DOI 10.1002/esp.1515, 2007

8. Kelly, F. J., and Fussell, J. C. Air pollution and public health: emerging hazards and improved understanding of risk. *Environ. Geochem. Health* 2015, 37, 631–649; DOI 10.1007/s10653-015-9720-1

9. Kelly, F. J., and Fussell, J. C. Size, source and chemical composition as determinants of toxicity attributable to ambient particulate matter. *Atmos. Environ. 2012,* 60, 504–526; DOI 10.1016/j.atmosenv.2012.06.039

10. Tsai, F. C., Apte, M. G., and Daisey, J. M. An exploratory analysis of the relationship between mortality and the chemical composition of airborne particulate matter. *Inhal. Toxicol 2000,* 12, 121–135

11. Cassee, F. R., Heroux, M.-E., Gerlofs-Nijland, M. E., and Kelly, F. J. Particulate matter beyond mass: recent health evidence on the role of fractions, chemical constituents and sources of emission. *Inhal. Toxicol* 2013, 25, 802–812; DOI 10.3109/08958378.2013.850127

12. Vogl, R. A., and Henry, R. N. Characteristics and contaminants of the Salton Sea sediments. *Hydrobiologia 2002,* 473, 47–54; DOI 10.1023/A:1016509113214

13. Xu, E. G., Bui, C., Lamerdin, C., and Schlenk, D. Spatial and temporal assessment of environmental contaminants in water, sediments and fish of the Salton Sea and its two primary tributaries, California, USA, from 2002 to 2012. *Sci. Total Environ 2016,* 559, 130–140; DOI 10.1016/j.scitotenv.2016.03.144

14. Breit, G., Goldstein, H., Reynolds, R., & Yount, J. Distribution of major anions and trace elements in the unsaturated zone at Franklin Lake Playa, California, USA. *Nat. Resour. Env. Iss.* 2009, 15, 93-103

15. *AQMIS, Air Quality and Meteorological Information System* Website https://www.arb.ca.gov/aqmis2/aqmis2.php, Last Access: 20 February 2017

16. U.S. Geological Survey, USGS Current Conditions for USGS 10254005 SALTON SEA NR WESTMORLAND CA, https://waterdata.usgs.gov/ca/nwis, Last Access: June 19, 2017

17. Reheis, M. C., Budahn, J. R., and Lamothe, P. J. Geochemical evidence for diversity of dust sources in the southwestern United States. *Geochim. Cosmochim. Ac.* 2002, 66, 1569–1587; DOI 10.1016/S0016-7037(01)00864-X

18. Belis, C. A., Karagulian, F., Larsen, B. R., and Hopke, P. K. Critical review and meta-analysis of ambient particulate matter source apportionment using receptor models in Europe. *Atmos. Environ. 2013,* 69, 94–108; DOI 10.1016/j.atmosenv.2012.11.009

19. Reimann, C., and Caritat, P. Intrinsic Flaws of Element Enrichment Factors (EFs) in Environmental Geochemistry. *Environ. Sci. and Technol* 2000, 34, 5084–5091; DOI 10.1021/es001339o

20. Wedepohl, K. H. The composition of the continental crust. *Geochim. Cosmochim. Ac*. 1995, 59, 1217–1232; DOI 10.1016/0016-7037(95)00038-2

21. Paatero, P., and Tapper, U. Positive matrix factorization: A non-negative factor model with optimal utilization of error estimates of data values. *Environmetrics* 1994, 5, 111–126; DOI 10.1002/env.3170050203

22. Paatero, P., Eberly, S., Brown, S. G., and Norris, G. A. Methods for estimating uncertainty in factor analytic solutions. *Atmos. Meas. Tech.* 2014, 7, 781–797, DOI 10.5194/amt-7-781-2014

23. Brown, S. G., Eberly, S., Paatero, P., and Norris, G. A. Methods for estimating uncertainty in PMF solutions: examples with ambient air and water quality data and guidance on reporting PMF results. *Sci. Total Environ.* 2015, 518–519, 626–635; DOI 10.1016/j.scitotenv.2015.01.022

24. Buck, B. J., King, J., and Etyemezian, V. Effects of Salt Mineralogy on Dust Emissions, Salton Sea, California. *Soil. Sci. Soc. Am. J.* 2011, 75, 1971; DOI 10.2136/sssaj2011.0049

25. Clements, A. L., Fraser, M. P., Upadhyay, N., Herckes, P., Sundblom, M., Lantz, J., and Solomon, P. A. Characterization of summertime coarse particulate matter in the Desert Southwest Arizona, USA. *J. Air Waste 2013*, 63, 764-777; DOI dx.doi.org/10.1080/10962247.2013.787955

26. Engelbrecht, J. P., Kavouras I. G., ShaferD. S., Campbell, D., Campbell, S., McCurdy, G., Kohl, S. D., Nikolich, G., Sheetz, L., Gertler, A. W. Chemical Variability of PM10 and PM2.5 in Southwestern Rural Nevada, USA. *Water, Air, and Soil Poll.* 2015, 226, 217: DOI 10.1007/s11270-015-2481-8

27. *Cal EPA, OEHHA Chemical Database*; https://oehha.ca.gov/air/chemicals. Last Access 2/23/2017

28. Hamilton, S. J. Review of selenium toxicity in the aquatic food chain. *Sci. Total Environ.* 2004, 326, 1–31; DOI 10.1016/j.scitotenv.2004.01.019

29. Valavanidis, A., Fiotakis, K., & Vlachogianni, T Airborne Particulate Matter and Human Health: Toxicological Assessment and Importance of Size and Composition of Particles for Oxidative Damage and Carcinogenic Mechanisms. *J. Environ. Sci. Heal*. C. 2008, 26, 339–362; DOI 10.1080/10590500802494538

30. Marticorena, B., and Bergametti, G. Modeling the atmospheric dust cycle: 1. Design of a soil-derived dust emission scheme. *J. Geophys. Res-Atmos.*1995, 100, 16415–16430; DOI 10.1029/95JD00690

31. Schroeder, R. A., Orem, W. H., and Kharaka, Y. K. Chemical evolution of the Salton Sea, California: nutrient and selenium dynamics. *Hydrobiologia* 2002, 473, 23–45, https://doi.org/10.1023/A:1016557012305

32. LeBlanc, L. A., and Schroeder, R. A. Transport and distribution of trace elements and other selected inorganic constituents by suspended particulates in the Salton Sea Basin, California, 2001. *Hydrobiologia* 2008, 604, 123–135; https://doi.org/10.1007/s10750-008-9319-y

33. Lawrence, C. R., and Neff, J. C. The contemporary physical and chemical flux of aeolian dust: A synthesis of direct measurements of dust deposition. Chem. Geol. 2009, 267, 46-63; DOI 10.1016/j.chemgeo.2009.02.005

34. Linak, W., and Wendt, J. Toxic Metal Emissions from Incineration - Mechanisms and Control. *Prog. Energ. Combust.*1993, 19, 145–185; DOI 10.1016/0360-1285(93)90014-6

35. Echalar, F., Gaudichet, A., Cachier, H., and Artaxo, P Aerosol Emissions by Tropical Forest and Savanna Biomass Burning: Characteristic Trace Elements and Fluxes. *Geophysical Research Letters* 1995, 22, 3039–42; DOI10.1029/95GL03170

36. Chellam, S., Kulkarni, P., and Fraser, M. P. Emissions of organic compounds and trace metals in fine particulate matter from motor vehicles: A tunnel study in Houston. *Texas. J. Air Waste Manage.* 2005, 55, 60–72

37. Hulskotte, J. H. J., Roskam, G. D., and Denier van der Gon, H. A. C. Elemental composition of current automotive braking materials and derived air emission factors. *Atmos. Environ.* 2014, 99, 436–445; DOI 10.1016/j.atmosenv.2014.10.007

38. King, J., Etyemezian, V., Sweeney, M., Buck, B. J., and Nikolich, G. Dust emission variability at the Salton Sea, California, USA. *Aeolian Research* 2011, 3, 67–79; DOI 10.1016/j.aeolia.2011.03.005

39. Gill, T. E., Gillette, D. A., Niemeyer, T., and Winn, R. T. Elemental geochemistry of wind-erodible playa sediments, Owens Lake, California. Nucl. Instru. and Meth. B 2002, 189, 209–213; DOI 10.1016/S0168-583X(01)01044-8

40. Lough, G. C., Schauer, J. J., Park, J. S., Shafer, M. M., Deminter, J. T., and Weinstein, J. P. Emissions of metals associated with motor vehicle roadways; *Environ. Sci. and Technol.* 2005, 39, 826–836, DOI 10.1021/es048715f

41. Chan, Y., Hawas, O., Hawker, D., Vowles, P., Cohen, D. D., Stelcer, E., Simpson, R., Christensen, E. Using multiple type composition data and wind data in PMF analysis to apportion and locate sources of air pollutants. *Atmos. Environ*. 2011, 45, 439–449; DOI 10.1016/j.atmosenv.2010.09.060

42. Mooibroek, D., Schaap, M., Weijers, E. P., and Hoogerbrugge, R. Source apportionment and spatial variability of PM2.5 using measurements at five sites in the Netherlands. *Atmos. Environ*. 2011, 45, 4180–4191; DOI 10.1016/j.atmosenv.2011.05.017

43. O'Dowd, C. D., and Leeuw, G. Marine aerosol production: a review of the current knowledge. *Philos. T. Roy. Soc. A.* 2007, 365, 1753–1774; DOI 10.1098/rsta.2007.2043

44. Alleman, L. Y., Lamaison, L., Perdrix, E., Robache, A., and Galloo, J.-C. PM10 Metal Concentrations and Source Identification Using Positive Matrix Factorization and Wind Sectoring in a French Industrial Zone. *Atmos. Res.* 2010, 96, 612–625; DOI 10.1016/j.atmosres.2010.02.008

45. Zhang, R., Jing, J., Tao, J., Hsu, S.-C., Wang, G., Cao, J., Lee, C. S. L., Zhu, L., Chen,Z., Zhao, Y., Shen, Z. Chemical characterization and source apportionment of PM2.5 in Beijing: seasonal perspective. *Atmos. Chem. Phys.* 2013, 13, 7053–7074; DOI 0.5194/acp-13-7053-2013

46. Polissar, A. V., Hopke, P. K., and Paatero, P. Atmospheric aerosol over Alaska - 2. Elemental composition and sources, *J. Geophys. Res-Atmo.* 1998, 103, 19045–19057; DOI 10.1029/98JD01212

47. Ramadan, Z., Song, X. H., and Hopke, P. K. Identification of sources of Phoenix aerosol by positive matrix factorization. *J. Air Waste Manage.* 2000, 50, 1308–1320

48. Peng, X., Shi, G.-L., Zheng, J., Liu, J.-Y., Shi, X.-R., Xu, J., and Feng, Y.-C. Influence of quarry mining dust on PM2.5 in a city adjacent to a limestone quarry: Seasonal characteristics and source contributions. *Sci. Total Environ.* 2016, 550, 940–949 DOI 10.1016/j.scitotenv.2016.01.195

49. Chen, A, L.-W., Watson, J. G., Chow, J. C., DuBois, D. W., and Herschberger, L. Chemical mass balance source apportionment for combined PM2.5 measurements from U.S. non-urban and urban long-term networks. *Atmos. Environ.* 2010, 44, 4908–4918; DOI 10.1016/j.atmosenv.2010.08.030

50. Kelly, K. E., Kotchenruther, R., Kuprov, R., and Silcox, G. D. Receptor model source attributions for Utah's Salt Lake City airshed and the impacts of wintertime secondary ammonium nitrate and ammonium chloride aerosol. *J. Air Waste Manage*. 2013, 63, 575–590; DOI 10.1080/10962247.2013.774819

51. Wen, H., & Carignan, J.; Reviews on atmospheric selenium: Emissions, speciation and fate, Atmos.Environ. 2007, 41, 7151–7165; DOI 10.1016/j.atmosenv.2007.07.035

52. Johnson, P. I., Gersberg, R. M., Rigby, M., and Roy, S. The fate of selenium in the Imperial and Brawley constructed wetlands in the Imperial Valley (California). *Ecol. Eng.* 2009, 35, 908–913; DOI 0.1016/j.ecoleng.2008.12.020

53. Hansen, D., Duda, P. J., Zayed, A., and Terry, N. Selenium removal by constructed wetlands: Role of biological volatilization. *Environ. Sci. and Technol*. 1998, 32, 591–597; DOI 10.1021/es970502l

54. Banuelos, G. S., & Lin, Z.-Q. Acceleration of selenium volatilization in seleniferous agricultural drainage sediments amended with methionine and casein. *Environmental Pollution*, 2009, 150, 306–312; DOI 10.1016/j.envpol.2007.02.009

55. Zhang, Y., & Frankenberger, W. T. Effects of Soil Moisture, Depth, and Organic Amendments on Selenium Volatilization, *J. Environ. Qual.* 1999, 28, 1321; DOI 10.2134/jeq1999.00472425002800040037x

56. Debell, L. J., Gebhart. K. A., Hand. J. L., Malm. W. C., Pitchford, M. L., Schichtel, B. A., and White, W. H. IMPROVE (Interagency Monitoring of Protected Visual Environments): Spatial and seasonal patterns and temporal variability of haze and its constituents in the United States: Report IV, CIRA Report ISSN: 0737-5352-74. Colo. State Univ., Fort Collins, 2006

57. Hand, J. L., Copeland, S. A., Day, D. E., Dillner, A. M., Indresand, H., Malm, W. C., McDade, C. E., Moore, C. T., Pitchford, M. L., Schichtel, B. A., Watson, J. G. Spatial and Seasonal Patterns and Temporal Variability of Haze and its Constituents in the United States: Report V June 2011, 2011

58. Eldred, B. Evaluation of the equation for soil composite: Internal memo to IMPROVE staff, 2003

59. Jia, Y., Kong, X., Weiser, M. D., Lv, Y., Akbar, S., Jia, X., Tian, K., He, Z., Lin., H., Bei, Z., Tian, X. Sodium limits litter decomposition rates in a subtropical forest: Additional tests of the sodium ecosystem respiration hypothesis. *Appl. Soil Ecol.* 2015, 93, 98–104; DOI 10.1016/j.apsoil.2015.04.012

60. Subbarao, G. V., Ito, O., Berry, W. L., & Wheeler, R. M. Sodium - A functional plant nutrient, *Crit. Rev. Plant Sci*. 2003, 22, 391–416; DOI /10.1080/07352680390243495

61. Koehler, K. A., Kreidenweis, S. M., DeMott, P. J., Prenni, A. J., and Petters, M. D. Potential impact of Owens (dry) Lake dust on warm and cold cloud formation. *J. Geophys. Res-Atmos*. 2007, 112, D12210; DOI 10.1029/2007JD008413

62. Hahnenberger, M., & Nicoll, K. Meteorological characteristics of dust storm events in the eastern Great Basin of Utah, USA. *Atmos. Environ.* 2012, 60, 601–612; DOI 10.1016/j.atmosenv.2012.06.029

63. Liu, D., Abuduwaili, J., Lei, J., & Wu, G. Deposition Rate and Chemical Composition of the Aeolian Dust from a Bare Saline Playa, Ebinur Lake, Xinjiang, China. *Water, Air, and Soil Poll.* 2011, 218(1–4), 175–184; DOI 10.1007/s11270-010-0633-4

64. Stone, R. Saving Iran's Great Salt Lake. *Science* 2015 *349*(6252), 1044–1047; DOI 10.1126/science.349.6252.1044

Chapter 3: Dust Sources in the Salton Sea Basin: A Clear Case of an Anthropogenically Impacted Dust Budget

3.0 Acknowledgement of Co-Authorship

This work was completed with contributions from Alexander L. Frie, Alexis C. Garrison, Michael V. Schaefer, Steve Bates, Jon Botthoff, Mia Maltz, Samantha C. Ying, Timothy Lyons, Emma Aronson, and Roya Bahreini.

3.1 Introduction

Atmospheric mineral dust particles, aerosols sourced from the suspension of soils, play several important roles in the earth system. Suspended mineral dust decreases air quality by increasing particulate matter (PM) concentrations and shifts the Earth's radiation budget by absorbing and scattering radiation.[1] When dust particles deposit, they can be sources of essential nutrients or deadly toxicants and also change the Earth's surface albedo.[2-5] Developing an understanding of dust is increasingly important as emissions have been increasing in recent decades.[6,7] Despite this, knowledge of mineral dust composition and emission into the atmosphere is limited.[8-10] To better constrain mineral dust influences on air quality, climate, and downwind environments, dust sources and their controls must be identified. Here, we characterize the sources of dust in the Salton Sea Basin in the American Southwest.

The Salton Sea Basin in southeastern California is classified as non-attainment for particulate matter less than 10 μm (PM_{10}) by the US Environmental Protection Agency.[11] Mineral dust emissions are thought to be the major driver of poor air quality, and are often attributed to natural sources. Compounding this issue is a large endorheic lake, the Salton Sea, which is shrinking due to changes in water management. The shrinking of endorheic

lakes is not a localized phenomenon, but a process occurring on a global scale.[12] The dry lakebeds (playas) are often significant dust sources and represent a clear anthropogenic impact on the dust budget.[13-15] This was observed at Owen's Lake in California in the 20th century when the lakebed became the largest point-source of PM_{10} in North America.[16] Salton Sea playas present a possible dust source of a similar scale.

To understand the dust dynamics and anthropogenic impacts in the Salton Sea Basin, dust sources and their controls must be quantified. Here, the impacts of specific dust sources are explored on a regional scale. These results provide insight into the relative importance, composition, and seasonal trends of sources.

3.2 Methods

3.2.1 Sample Collection and Treatment

Dust deposition samplers were constructed based on the design by Reheis and Kihl.[17] Briefly, a Teflon coated bundt pan (25.4 cm diameter) was inset with a coarse Kevlar mesh. Quartz marbles were placed on top of the mesh. The pan was protected from avian disruption using two crossed Tanglefoot coated straps domed over the pan. All samplers were deployed at a height of ~ 2.5 m, as in Aciego et al.[18]

Samplers were deployed in duplicates at five sites in the Salton Sea Basin of California: Sonny Bono (SB), Wister (WI), Dos Palmas (DP), Boyd Deep Canyon (BD), and Palm Desert (PD) (Table 1). Samplers were collected approximately monthly from April 28th 2017 until May 2nd 2018, yielding 11 sample sets from all sites except Dos Palmas (Table A2.1). Twice access to Dos Palmas was limited, therefore only 9 sample sets were collected at this site. Occasionally, samplers had been disturbed and were

unusable (e.g. bird feces were present) and were excluded from the analysis. It is worth noting that "month" used to describe the temporal space of the samples does not correspond to an exact calendar month as a duration of sampling, but rather to the calendar month in which a sampler was deployed the most days. Upon collection, the samplers were extracted with water, dried, and the remaining solid was weighed (Mettler AE 260, 10^{-4} g). One sample, SB April 2018, was physically extracted using a nylon brush to maintain the integrity of soluble minerals and allow physical analysis. Sample treatment is dicussed further in the Appendix 2.

Table 3.1 Sampling sites' location, management, qualitative class, dominant mass source and observed mass flux. Management abbreviations area as follows: University of California (UC), United States Bureau of Land Management (BLM), California Fish and wildlife (CAFW), United States Fish and Wildlife (USFW).

Site	Lat.	Long.	Management	Class	Dominate Mass Source	Flux (mg m^2 yr^{-1})
Sonny Bono (SB)	-115.6	USFW	On-Playa	*Playa*	89	
Wister (WI)	-115.60	CAFW	Managed Wetland	*Colorado & Local Alluvium*	17	
Dos Palmas (DP)	-115.84	BLM	Open Colorado Desert	*Local Alluvium*	16	
Palm Desert (PD)	-116.35	UC	Urban	*Local Alluvium*	30	
Boyd Deep (DP)	-116.37	UC	Protected Canyon	*Local Alluvium*	11	

3.2.2 Flux Estimates

Dust Flux was calculated as described by Reheis and Kihl (Eq. 3.1).[17,19]

$$Flux = \frac{Mass*(1-f_{org})}{Area*Years} \quad (3.1)$$

Where Mass is the dust mass collected in the pan, f_{org} is the fraction of organic matter as

measured via ashing (SI), *Area* is the planar area of the pan, and years is the length of pan deployment. It should be noted that the fluxes are not a quantitative net measurement of the difference between emission and deposition, but the term used to describe mass measurements from these samplers.[16-18,20,21]

3.2.3 Chemical and Physical Analysis

Samples were analyzed for total elemental and soluble anion content. One sample, representing playa emissions, was also analyzed with Scanning Electron Microscopy (SEM) and X-ray diffraction (XRD).

To measure elemental content, samples were digested then analyzed with inductively coupled plasma mass spectroscopy (ICP-MS, Aligent 7900) for total As, Al, Ba, Ca, Cd, Co, Cu, Cr, Fe, K, V, Mg, Mn, Mo, Na, Ni, Pb, Se, Sn, Sb, Sr, Ti, U, Th, Zn. To measure soluble anion content, samples were extracted with ultrapure water and the resulting solution was analyzed for sulfate (SO_4^{2-}), phosphate (PO_4^{3-}), nitrate (NO_3^-), nitrite (NO_2^-), and chloride (Cl^-) using ion chromatography (IC) (Dionex Aquion, Thermo Scientific). All elemental concentrations are presented on a dry mass basis (e.g. mg kg^{-1}).

The physically extracted SB April 2018 sample was analyzed with SEM (NovaNanoSEM 450) combined with Energy-Dispersive X-ray Spectroscopy (AztecSynergy, Oxford Instruments) (SEM-EDS). SEM-EDS data are reported as a qualitative measure of the physical and chemical nature of playa emissions. To investigate the mineralogy, the sample was also analyzed using X-ray diffraction (Siemens D500). Additional information concerning the digestion procedure and the analyses by the ICP-MS, IC, and XRD are included in Appendix 2.

3.2.4 Data Analysis Tools

Positive matrix factorization (EPA PMF 5.0) (PMF) and crustal enrichment factors (EFs) were used to investigate the sources of, and chemical variation within, the sampled dusts. PMF is a source apportionment model which identifies source profiles and contributions by exploring sources of variation within a sample set.[22] PMF is analogous to principle component analysis but unique and powerful for three main reasons. First, PMF does not allow significant negative contributions of sources, and only identifies sources with a physical meaning in an environmental context. Second, PMF weighs data using an uncertainty matrix such that more certain measurements are more influential.[23] Third, PMF does not require source profiles to be known, so it can arrive at a solution without assuming specific sources are present. Here, total elemental and soluble anion mass (mg pan^{-1}) for each sample were input into PMF. Mass, f_{org}, Sn, NO_3^-, and NO_2^- were input as weak variables due to high signal to noise ratios. Construction of the uncertainty matrix is discussed in detail in appendix 2.

PMF was tested with 2-9 factors to find the best fit to the data. A 7-factor model was chosen as the best fit because factors were able to be related to identifiable sources. Additionally, displacement uncertainty analysis indicated a stable solution, scaled residues were generally low and normally distributed, and Q/Q_{exp} values only slightly decreased upon adding additional factors (Figure A2.1). The uncertainties in source factor profiles and source contributions were estimated using the displacement error analysis method.[23]

EFs were used to explore compositional variation between samples. EFs explore differences between a sample and a given geologic baseline. EFs are defined as the ratio of

an element to a known, low-mobility element, such as Al or Ti, divided by the same ratio in a given geologic baseline. Here, the average composition of the upper continental crust (UCC) as reported by Wedephol (1995) is used as the baseline, and Al is used as the reference element (Eq.3.2)[24]

$$EF = \frac{(M_{Measured}/Al_{Measured})}{(M_{UCC}/Al_{UCC})} \quad (3.2)$$

Where $M_{measured}$ is the concentration of an element in the sample, $Al_{measured}$ is the concentration of Al in the sample, M_{UCC} is the UCC concentration of the element, and Al_{UCC} is the UCC concentration of Al.[24] Although EFs are insightful, shifting antecedent geology can lead to false interpretations due to natural variability in baseline concerntrations.[25] Additionally, the significance of an EF is dependent on an element's bulk concentration and geologic variability. For example, trace elements often only need small concentration increases to yield large enrichments, but major elements would be unable to reach similar enrichments without the presence of unrealistically high values. This means EFs should be viewed in the context of the specific species and the sampling location.

3.3 Results and Discussion

3.3.1 Annual Mass Flux

Annual dust deposition fluxes (Section 2.2) were 89 g m^{-2} yr^{-1} for SB, 17 g m^{-2} yr^{-1} for WI, 16 g m^{-2} yr^{-1} for DP, 30 g m^{-2} yr^{-1} for PD and 11 g m^{-2} yr^{-1} for BD. All fluxes were higher than the median and average values observed by Reheis for sites in CA and NV from 1984 – 1999 (Figure A2.3),[19] indicating that dust fluxes in this region are relatively

high compared to the surrounding area. Fluxes were within the ranges of those observed previously in playa basins in the American southwest (Figure A2.3).[19]

Of particular interest is the comparison of the on-playa site of the Salton Sea Basin (SB) to the on-playa site at Owens Lake (T-62).[16] The average flux observed on-playa at Owens Lake from 1991-2002 was 356 ± 174 g m^{-2} yr^{-1}.[19] This flux is higher than the flux observed at SB (89 g m^{-2} yr^{-1}), but the flux at SB is approaching the magnitude of observations at Owen's Lake. This suggests Salton Sea playas are a major dust source, even at the current exposed playa levels, and are approaching the scale of Owens Lake's emissions.

Variability in dust emissions is controlled by environmental conditions including antecedent precipitation and concurrent wind speed.[26,27] To explore conditions during sampling, data from local long-term precipitation (5 stations, average of 81 years of data, 1902-2018) and wind (3 stations, average of 18 years of data, 1999-2018) stations were examined (Tables S2 and S3). Station data were obtained from the National Oceanic and Atmospheric Association's (NOAA) National Centers for Environmental Information (NCEI).[28]

In this region, winter precipitation is theorized to suppress the following season's non-playa dust emissions (e.g. alluvial fans) and increase the following season's playa emissions. The reduction in non-playa emissions is thought to be driven by increased vegetative cover while the increased playa emissions are due to increased salt and sediment delivery and/or water table height fluctuations.[13,27] Although it is unknown if the playa relationship would hold in Salton Sea playas given that significant water is present within

the Sea year round. Winter (September-March) precipitation was high (on average 77th percentile) prior to sampling in 2016-17 and low (on average at 31st percentile) during 2017-18 sampling (Table A2.22). Therefore, relative to precipitation, non-playa dust emissions would be expected to be low during 2017 and high during 2018, the inverse would be expected for playa emissions.

Generally, higher wind speeds correspond to higher dust emissions.[27,29] Among the wind stations examined, seasonal wind speeds are highest between calendar months March and April (Figure A2.3). During sampling, basin- wide extraordinary high windspeeds were observed in calendar months August and September (>89th percentile of NCEI data at all sites) and extraordinary low windspeeds were observed in November (<12th percentile at all sites) (Table A2.2). For all other months, wind speeds were non-extreme (between 20th-80th percentiles). Relative to wind speed, conditions can be considered within the normal ranges for most months of our sampling, but relatively high wind speeds were observed during September and August. Thus, we can interpret the dust fluxes observed here as approximately "typical" dust fluxes for the region.

3.3.2 Enrichment Factors

EFs were calculated for all samples and demonstrate differences in source properties (Figure 3.1) both spatially and temporally. Qualitatively, EFs can be divided by spatial trends and enrichment intensity.

Many elements (Na, Ca, K, Mg, Sr, Se, U) displayed strong decreasing EF trends from south to north, with the highest enrichments occurring at WI or SB (Figure 3.1).

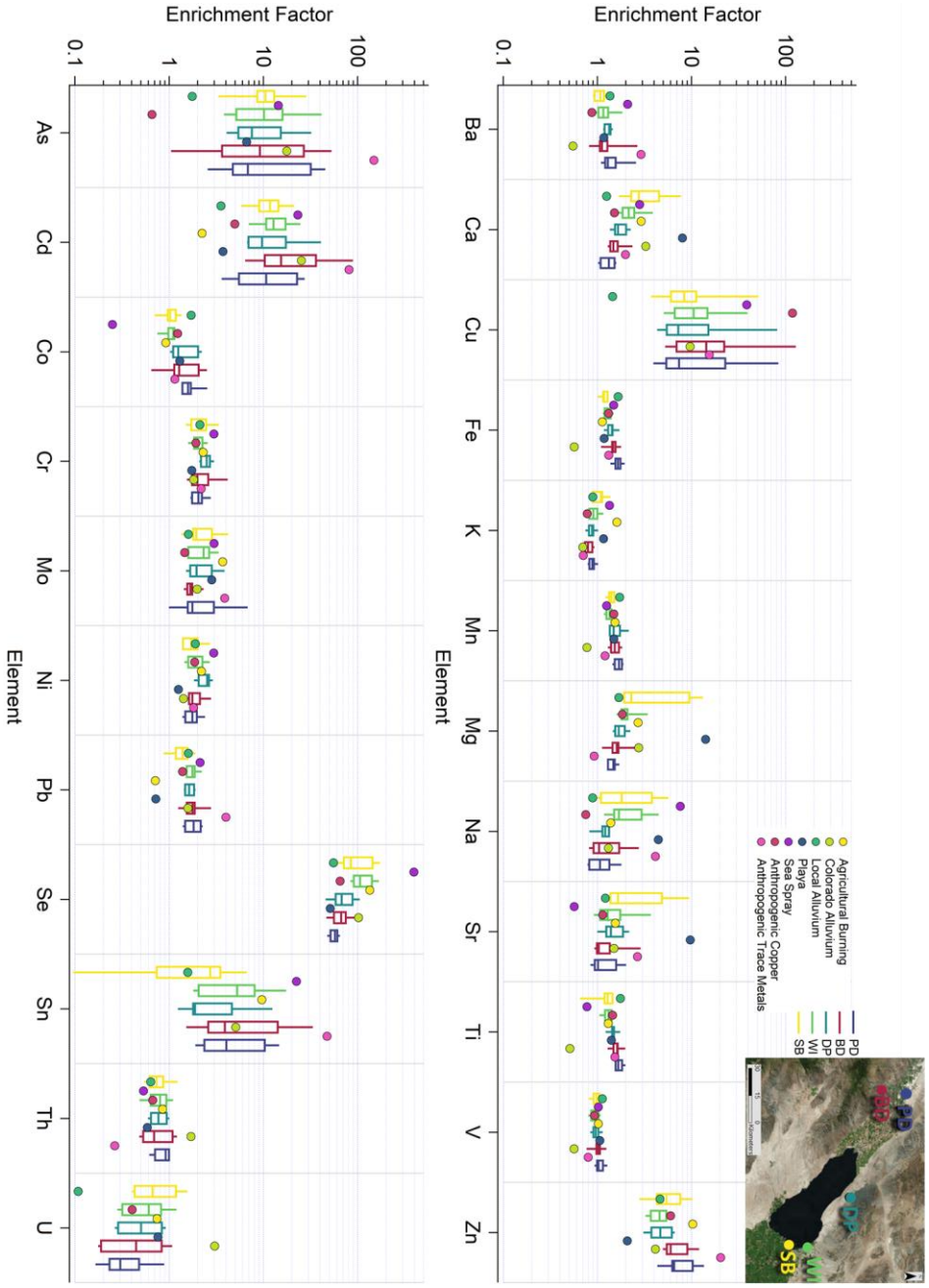

Figure 3.1 Box and whisker plots of enrichment factors at each site and enrichment factors associated with PMF factors (dots). Within the box and whiskers, the centerline represents the median of the data, the top and bottom of the box correspond to the 75th and 25th percentiles, respectively, and the top and bottom whisker correspond to the 90th and 10th percentiles respectively. Antinomy (Sb) has been excluded from this graph due multiple BDL values creating meaningless EFs. The inset map details the locations of the sampling sites.

Notably, these elements are commonly associated with evaporite minerals (Na, Ca, K, Mg, Sr), have been observed at high concentrations in Salton Sea sediments or water (Se, U, Ca, Na),[30,31] or have been observed in Salton Sea playas (Na, Ca, Se).[32,33] This trend likely reflects the importance of playa and sea spray emissions to PM composition within the southern sections of the Salton Sea Basin.

Other elements (Ti, Fe, Co, Ba, Sn) displayed strong decreasing trends from north to south, with the highest enrichments occurring at PD or BD. Notably, many of these elements are associated with "traditional" crustal emissions (Ti, Fe, Co, Ba). It is possible that this spatial enrichment trend is the capturing of a compositional gradient within dust sources that exists between the north and south of the basin. This possibility is further explored in sections 3.5.2 and 3.5.3.

A third class of elements were highly enriched (EF >10) (Cu, As, Cd, Sb, Se) at all sites, indicating high background values or basin-wide sources. Among these, As displayed similar enrichments in local soils, which suggest that its high EF may be a reflection of the local soil characteristics.[32] Copper, Sb, and Cd are commonly associated with anthropogenic sources, and observed most strongly at PD, so their broad distribution suggests basin-wide anthropogenic influence.[34-37] Selenium is also associated with anthropogenic emissions but microbial Se volatilization could occur in Salton Sea sediments and playas, leading to an increase in Se content of ambient PM after atmospheric oxidation.[31,32,38] These processes would be likely most important during hot months and near the Salton Sea. Selenium EFs were highest at WI and during summer months (Figure A2.4) suggesting microbial Se volatilization as the dominant Se source. Overall, EFs

suggest compositional gradients of crustal sources across the Salton Sea Basin, the broad influence of anthropogenic activities, and possible biogenic emissions of Se.

3.3.3 Source Identification and Distribution

Seven dust sources were identified using PMF and knowledge of potential sources in the region (Figure 3.2): *Playa, Colorado Alluvium, Local Alluvium, Agricultural Burning, Sea Spray, Anthropogenic Trace Metals,* and *Anthropogenic Copper* (Italicized text refers specifically to the PMF identified source). Notably, three of these sources are crustal. This contrasts many PMF-based studies in urban environments which identify only a single crustal source.[39,40] The identification of multiple crustal sources reveals the potential of PMF to resolve individual crustal sources beyond a broad type.

In the following discussion, confidence in attributions is defined by the relative negative uncertainty as given by the displacement method.[23,41] Intervals were defined as confident (<0.25), semi-confident (<0.5), low-confidence (<0.75), and (<1) no-confidence (Table A2.4). A No-confidence attribution means that the species has a possible zero contribution to the factor. Weak variables other than mass are not discussed.

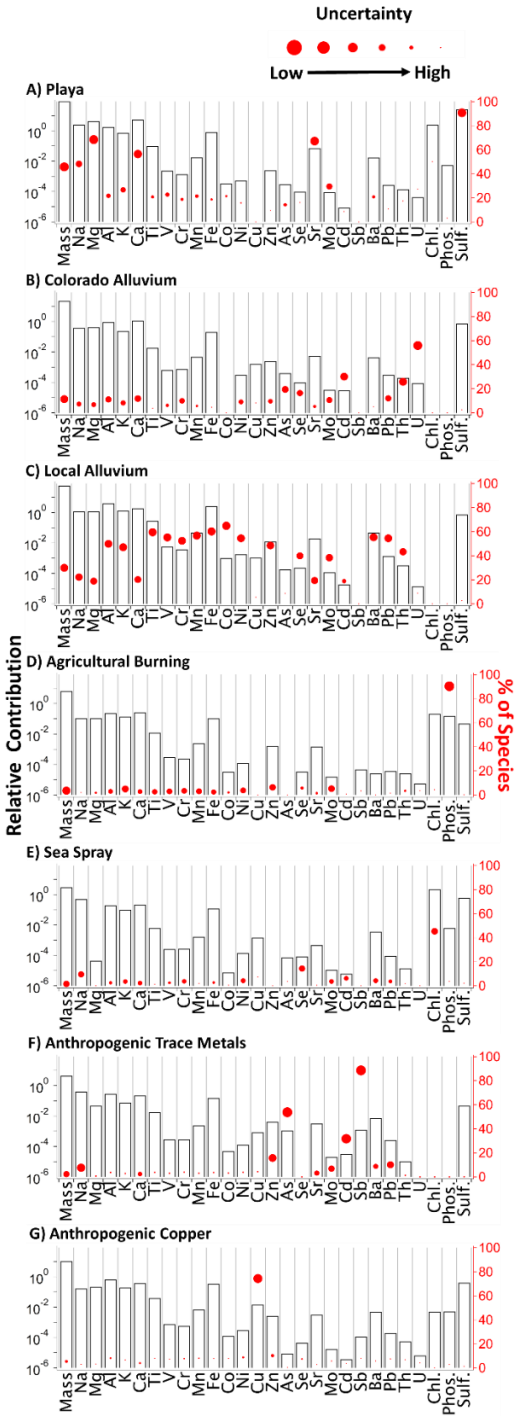

Figure 3.2. PMF source factor profiles of A) *Playa*, B) *Colorado Alluvium* C) *Local Alluvium*, D) *Agricultural Burning* E) *Sea Spray* F) *Anthropogenic Trace Metals*, and G) *Anthropogenic Copper*. Bars represent the relative contribution of each species within a factor and dots represent the percent of the total measured species attributed to the factor. Dots are inversely sized by the negative displacement uncertainty. The largest dots represent the most certain species within a factor.

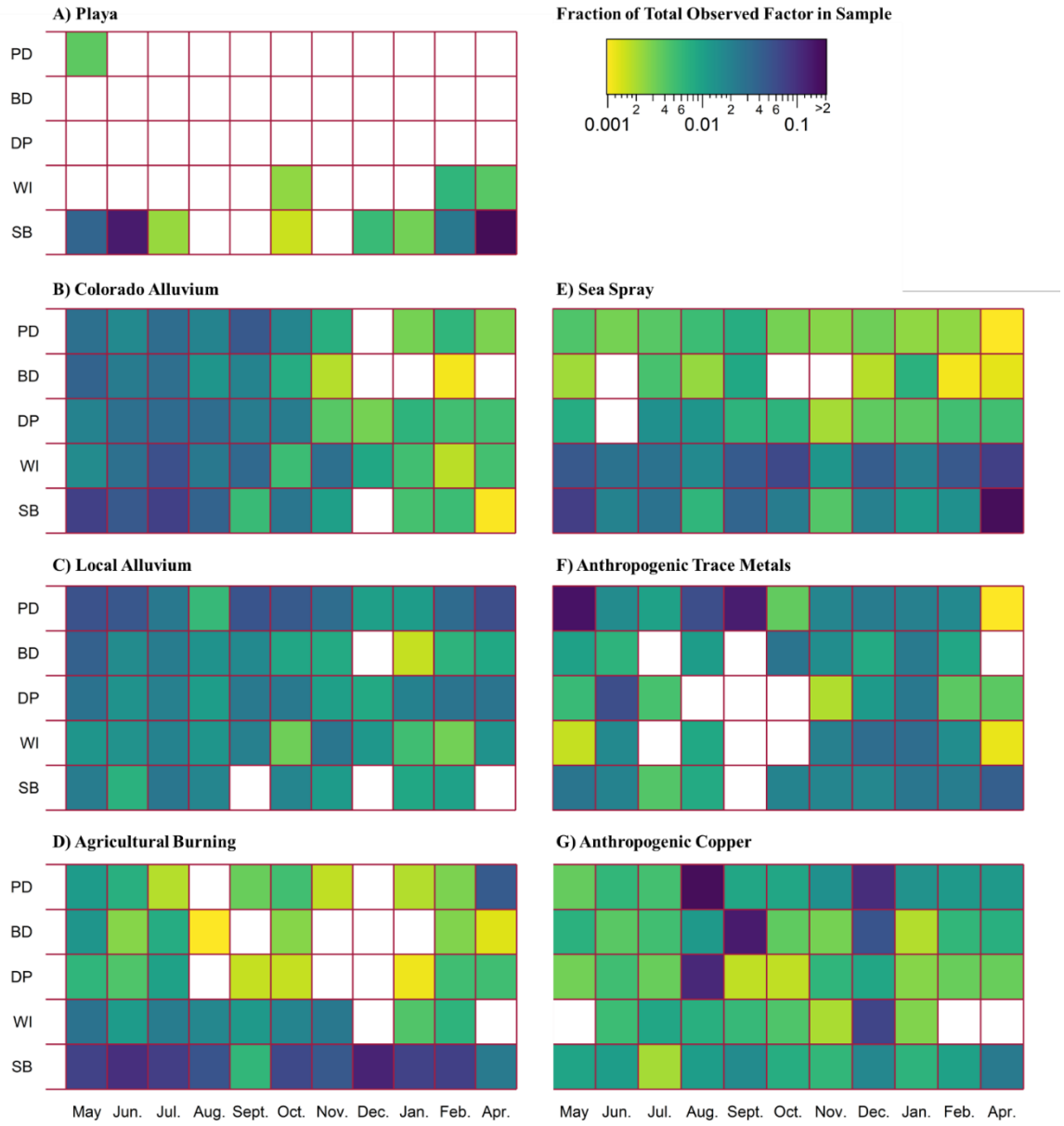

Figure 3.3. Fraction of PMF source factor observed within each sample, normalized by sampling length for A) *Playa*, B) *Colorado Alluvium* C) *Local Alluvium*, D) *Agricultural Burning* E) *Sea Spray* F) *Anthropogenic Trace Metals*, and G) *Anthropogenic Copper*. Values below 0.001 are displayed as white and above 0.2 as dark blue.

3.3.3.1 *Playa*

The *Playa* source was identified by confident attributions of Mg and SO_4^{2-}, and semi-confident attributions of Na, Ca, and Sr (Figure 3.2A, Table A2.4). These elements are all tracers of evaporite minerals (e.g. $MgSO_4$, $CaSO_4$, NaCl) which are known to be common in playas.[32,33,42] *Playa* was more enriched in Mg and Ca than in Na, indicating that Mg- and Ca-based species are important to playa composition. *Playa* also had a high mass fraction of soluble SO_4^{2-} (~29%). Given the high concentrations of Mg and sulfate in *Playa*, $MgSO_4$ minerals may be an important component of emissive playas at the Salton Sea. The nature of the minerals associated with this source is further discussed in section 3.3.4.

Playa displayed the most limited spatial and temporal distribution among all sources (Figure 3.3A) and was observed strongly during May 2017, June 2017, February 2018, and April 2018 sampling periods at SB (Figure 3.4A). These results suggest that Salton Sea playa emissions are most important during spring and summer months, consistent with the expected high emissions between March and June when regional high wind events tend to occur (Figure A2.2).[13,27] PMF attributed 36-47% of the total sampled mass to *Playa*. The large mass attribution is driven by a high mass flux observed at SB during the April sampling period (Figures 3.4A). Spatially, *Playa* was almost solely observed at SB and WI. This distribution is sensible, as predominant atmospheric transport trends in the months when *Playa* was observed were from west to east (Figure A2.5) such that playa emissions were unlikely to be observed at the other study sites.

To understand the potential downwind implications, forward trajectories were simulated daily from March 1st 2018 to June 30th 2018 at 20:00 (Local Time) when windspeeds, and theoretically playa emissions, are highest (Figure A2.6 & A2.7).[43] This analysis reveals Salton Sea playa emissions are possibly transported throughout the American Southwest, affecting areas of Utah, Arizona, and Southern Nevada including Las Vegas. The effects could include degradation of air quality, shifts in precipitation, and possible ecological damage due to transport and deposition of salt-rich PM.[44,45]

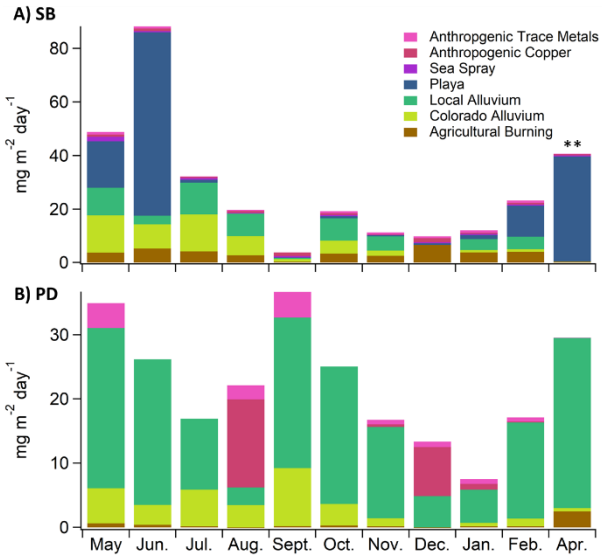

Figure 3.4 PMF attributions of mass during each sampling period for A) Sonny Bono and B) Palm Desert sites. PMF attributions are averaged between the duplicate samples for each sampling period. It should also be noted that some factors have highly uncertain mass attributions (Figure 3.2).
** SB April 2018 is displayed as 1/10th of its value given its high mass concentration compared to the other samples

3.3.3.2 *Colorado Alluvium*

The *Colorado Alluvium* source was identified by confident attributions of U and semi-confident attributions of Al, Ca, As, Se, Cd, Sn, Pb, and Th (Figure 3.2B, Table A2.4). Many of these elements are commonly associated with soil or crustal emissions (Ca, Al,

Pb, Th, U).[24] Much of the Salton Sea Basin is covered in alluvium from the Colorado River and sediments from the ancient Lake Cahuilla. These soils have a low concentration of Al, Fe, and Ti and high concentration of Ca (Figures A2.9-A2.12).[46] Conversely, multiple alluvial fans exist at the north end of the basin that are known dust sources;[47,48] dust from these sources (*Local Alluvium*) would likely be granitic in origin and thus be relatively rich in Al, Fe, and Ti. This compositional difference means dust from *Colorado Alluvium* can be easily distinguished from *Local Alluvium* by Al, Fe, Ti, and Ca content. *Colorado Alluvium* corresponds to alluvium deposited by the Colorado River and Ancient Lake Cahuilla. Shifts in the importance of *Colorado Alluvium* and *Local Alluvium* explain the EF gradients discussed in section 3.3.4.

Notably, 56 % of U measured in this study was attributed to *Colorado Alluvium* (Figure 3.2B). This high U contribution is possibly caused by the historical and ongoing use of Colorado River alluvial soils for agriculture, which may drive U enrichments in the soil and groundwater through application of phosphate.[49,50] The U enrichment in this factor suggests that dust emissions by *Colorado Alluvium* are closely linked with agricultural activities.

Colorado Alluvium shows basin wide importance accounting for 8-28% of the total sampled mass (Figures 3.2B and A2.8). Furthermore, it shows a strong seasonality across all sites (Figure 3.3B), with minimum contributions occurring during December - February and maximum contributions during May - August sampling periods. Ostensibly, these findings result from seasonal wind patterns and customary agricultural practices, as winds are strongest in spring-summer (Figure A2.3 and Table A2.2), and local agricultural

practices promote summer emission. Most of the land covered by the *Colorado Alluvium* to the north and south of the sea is currently farmed, with crops covering the fields in winter (Figure A2.13). Management of crop cover during the dust season may be a potential method for regional dust suppression.

3.3.3.3 *Local Alluvium*

The *Local Alluvium* source was identified by semi-confident attributions of Na, Mg, Al, K, Ca, Ti, V, Cr, Mn, Fe, Co, Ni, Zn, Se, Sr, Mo, Sn, Ba, Pb, and Th (Figure 3.2C, Table A2.4). All of these elements are present in soils, and some are common crustal tracers (Ca, Al, Fe, Ca, Mg, Pb, etc.).[24] *Local Alluvium* is different from *Colorado Alluvium* in multiple ways. Most importantly, it has much higher Al, Ti, and Fe mass concentrations. As discussed above, Al, Ti and Fe all have higher concentrations in the surrounding mountains and the associated alluvium than in the alluvium from the Colorado River (Figures A2.9-A2.12). [46]

Local Alluvium has the strongest contributions (71% of the observed mass) at PD (Figure 3.4B). This is likely due to the alluvial fan associated with the Whitewater River at the northern tip of the basin and just north of the Palm Desert, which is a known dust source.[47,48,51] *Local Alluvium* is also observed at the other sites, accounting for 20-44% of the total sampled mass (Figures 3.2C and A2.8); the strength of this source can be explained by the ubiquitous presence of alluvial fans around the basin. Additionally, this source is likely intensified by land use practices such as off-highway vehicle (OHV) sue. In addition to instantaneous emissions, OHV use can destroy protective soil crusts and increase the emission potential of surfaces.[52-54]

Temporally, *Local Alluvium* is strongest when wind speeds are high (spring-summer) and appears strongly in the September and October PD samples, which coincided with regionally high wind events (Figures 3.3C and A2.3, Table A2.2). Although *Local Alluvium* decreases in winter months, its contribution does not decrease as strongly as the *Colorado Alluvium,* likely because local alluvium is not as developed for agricultural use and OHV activity increases in winter.

3.3.3.4 *Agricultural Burning*

The *Agricultural Burning* source was identified by semi-confident attributions of PO_4^{3-}, K, Zn, Mo, and low confidence attributions of many crustal species (Figure 3.2D, Table A2.4). Potassium is commonly associated with biomass burning emissions[37,55] and biomass burning events are also known to be important mechanisms of P redistribution[56]. The crustal elements associated with this factor, which likely represent co-emitted dusts, are similar to that of *Colorado Alluvium,* with high Ca and low Ti, Al, and Fe (Figure 3.1, Table A2.4) and can be explained by agricultural biomass burning on farmed Colorado Alluvial Soils in the Salton Sea basin.

Agricultural Burning was strongly observed at SB and WI, accounting for 4% and 5% of the observed mass at each site, respectively (Figure 3.3D and A2.8). This is likely due to the proximity of these sites to active agricultural regions, which are mostly south of the Salton Sea. *Agricultural Burning* is relatively strong at all sites during May, June, and July sampling periods. However, the contributions are relatively weak at all sites, other than SB, during December - February. This seasonality could be driven by differences in predominant wind patterns, which are northerly in winter (Figure A2.5). The continued

observation of *Agricultural Burning* at SB might be because of its proximity to agricultural areas, so it may be more sensitive to smaller scale, local emissions even when predominant transport is away from the site. Basin wide, PMF attributed 2-7% of the total mass flux to *Agricultural Burning.*

3.3.3.5 *Sea Spray*

Sea Spray was identified by confident attributions of Cl^-, Na, and Se (Figure 3.2E, Table A2.4). This source likely results from wave breaking at the Salton Sea as it is most strongly observed at SB and WI (Figure 3.3E). Na and Cl^- are known dissolved ions in the sea, and Se is known to have relatively high concentrations in Salton Sea because the sea's major water source, the Colorado River, has high Se concenrations.[57] Sea Spray is a commonly identified aerosol source.[58-60] It is possible that some of this source is playa emissions, as playa formed from evaporating Salton Sea water would have a similar composition. Overall, *Sea Spray* has a relatively minor contribution to the total sampled dust mass (1-14%) (Figure A2.8) but contributes to a large component of total sampled Na (5-32%) and soluble Cl^- (25-100%) near the Salton Sea (Figure 3.2E).

3.3.3.6 *Anthropogenic Trace Metals*

The *Anthropogenic Trace Metals* source was identified by confident attributions of Sb, As, and Cd and semi-confident attributions of Na, Zn, and Pb (Figure 3.2F). These species have been associated with anthropogenic activities such as vehicle emissions, incinerators, and industry.[61-63] PMF attributed 1-11% of the total sampled mass to *Anthropogenic Trace Metals* (Figure 3.2F and S8).

Anthropogenic Trace Metals was most strongly observed at PD but had some contribution at all sites (Figures 3.3F and S8). The high contribution of *Anthropogenic Trace Metals* at PD is consistent with PD being the most urbanized site. *Anthropogenic Trace Metals* displayed a confined spatial distribution during the summer but was observed more strongly at all sites during the November-February sampling periods. This shift in contribution coincides with the shift in back trajectory directions from westerly to northerly winds during winter (Figure A2.5) and reveals the influence of emissions from the urbanized areas located upwind and to the north of the basin during these months. This indicates an increased influence of anthropogenic emissions throughout the basin during winter.

3.3.3.7 *Anthropogenic Copper*

The *Anthropogenic Copper* source, accounting for only 1-10% of the total sampled mass, was identified by confident attributions of Cu (Figure 3.2G). Cu is often associated with anthropogenic activities, particularly motor vehicle use and industrial production.[64-67] Although *Anthropogenic Copper* is observed in almost all samples, it has no broad trends, and occurs strongly within the DP Aug., BD Sept., BD Dec., PD Dec., and WI Dec samples (Figure 3.3G and S8). The sporadic strong detection of *Anthropogenic Copper* indicates that it may represent a mobile and localized source, such as vehicular brake dust. Copper increases toxicity in PM[68] so even small contributions of *Anthropogenic Copper* may have particularly potent health effects. Future work should attempt to indentify the source of copper in the Salton Sea Basin to constrain the impact of this source on human health.

3.3.4 SEM and XRD of Playa Emissions

SEM and XRD analysis of the physically extracted April 2018 SB sample (Section 2.1), which was dominated by *Playa*, reveals the nature of captured playa emissions. SEM-EDS analysis qualitatively shows Mg-S-O aggregates dominate the sample (Figure A2.14). This observation confirms our conclusion based on the ICP-MS and IC measurements that $MgSO_4$ minerals are a key component of emissive playas at the Salton Sea. XRD analysis of the April 2018 sample also reveals the presence of multiple evaporite minerals including hexahydrite ($MgSO_4 \cdot 6H_2O$), Epsomite ($MgSO_4 \cdot 7H_2O$), halite (NaCl), gypsum ($CaSO_4 \cdot 2H_2O$), and bassanite ($CaSO_4 \cdot 0.5H_2O$) (Figure A2.15).

$MgSO_4$ minerals (hexahydrite) have previously been observed in emissive playas at the Salton Sea by Buck et al.[33] Additionally, Goldstein et al. observed selective removal of SO_4^{2-} from playa soils by wind erosion,[69] but this is the first direct observation of $MgSO_4$ within emitted playa dusts. Together, these observations suggest the presence of hexahydrite or epsomite may be a possible predictor of the emissivity of Salton Sea playas. This is of interest as $MgSO_4$ minerals were not originally assessed as emissive crust types at the Salton Sea although other sulfate minerals, e.g. $NaSO_4$, were.[70] This finding reinforces the principle that mineral structure dynamics are key to playa emission potential and therefore should be the focus of future studies.

3.4 Implications

This work increases the resolution of dust source apportionment in the Salton Sea, not only identifying “desert”, “natural” or “crustal” emissions, but allocating dusts to specific sources. Among the PMF-resolved source factors, 6 of the 7 sources which

contribute to 55 to 80 % of total mass, are directly influenced or caused by anthropogenic activities. *Colorado Alluvium* and *Agricultural Burning* emissions are directly controlled by agricultural practices. *Playa* and *Sea Spray* emissions are a direct result of historic and current water management practices. *Anthropogenic Copper* and *Anthropogenic Trace Metals* are a result of current human activities. Additionally, *Local Alluvium* is likely controlled, in part, by the human disruption of natural surfaces, such as OHV use. These findings demonstrate the complexity and significant anthropogenic controls on the dust budget in the region and reinforce the need for a detailed understanding of the dynamics of dust sources not only in the Salton Sea Basin but globally.

PM_{10} within the Salton Sea basin exceeded national standards prior to exposure of the playas surrounding the Salton Sea. Here we have shown playa emissions are causing an increase in dust fluxes and undoubtedly degrade air quality. Playa emissions display extreme seasonality, with highest emissions during spring and early summer. This seasonality could be used to inform potential playa dust suppression efforts and lead to more efficient dust mitigation. Additionally, this work supports previous findings that sulfate-, and specifically $MgSO_4$-, containing playas are a particularly emissive playa type.[33,69]

3.5 Works Cited

1 Pachauri, R. K., Allen, M. R. , Barros, V. R. , Broome, J. , Cramer, W. , Christ, R. , Church, J. A. , Clarke, L. , Dahe, Q. , Dasgupta, P. , Dubash, N. K. , Edenhofer, O. , Elgizouli, I. , Field, C. B. , Forster, P. , Friedlingstein, P. , Fuglestvedt, J. , Gomez-Echeverri, L. , Hallegatte, S. , Hegerl, G. , Howden, M. , Jiang, K. , Jimenez Cisneroz, B. , Kattsov, V. , Lee, H. , Mach, K. J. , Marotzke, J. , Mastrandrea, M. D. , Meyer, L. , Minx, J. , Mulugetta, Y. , O'Brien, K. , Oppenheimer, M. , Pereira, J. J. , Pichs-Madruga, R. , Plattner, G. K. , Pörtner, H. O. , Power, S. B. , Preston, B. , Ravindranath, N. H. , Reisinger, A. , Riahi, K. , Rusticucci, M. , Scholes, R. , Seyboth, K. , Sokona, Y. , Stavins, R. , Stocker, T. F. , Tschakert, P. , van Vuuren, D. and van Ypserle, J. P. *Climate change 2014: synthesis report. Contribution of Working Groups I, II and III to the fifth assessment report of the Intergovernmental Panel on Climate Change*. (IPCC, 2014).

2 Chadwick, O. A., Derry, L. A., Vitousek, P. M., Huebert, B. J. & Hedin, L. O. Changing sources of nutrients during four million years of ecosystem development. *Nature* 397, 491-497, doi:10.1038/17276 (1999).

3 Lawrence, C. R. & Neff, J. C. The contemporary physical and chemical flux of aeolian dust: A synthesis of direct measurements of dust deposition. *Chemical Geology* 267, 46-63, doi:10.1016/j.chemgeo.2009.02.005 (2009).

4 Minder, J. R., Letcher, T. W. & Skiles, S. M. An evaluation of high-resolution regional climate model simulations of snow cover and albedo over the Rocky Mountains, with implications for the simulated snow-albedo feedback. *Journal of Geophysical Research-Atmospheres* 121, 9069-9088, doi:10.1002/2016jd024995 (2016).

5 Painter, T. H., Skiles, S. M., Deems, J. S., Bryant, A. C. & Landry, C. C. Dust radiative forcing in snow of the Upper Colorado River Basin: 1. A 6 year record of energy balance, radiation, and dust concentrations. *Water Resources Research* 48, doi:10.1029/2012wr011985 (2012).

6 Clow, D. W., Williams, M. W. & Schuster, P. F. Increasing aeolian dust deposition to snowpacks in the Rocky Mountains inferred from snowpack, wet deposition, and aerosol chemistry. *Atmospheric Environment* 146, 183-194, doi:10.1016/j.atmosenv.2016.06.076 (2016).

7 Achakulwisut, P., Shen, L. & Mickley, L. J. What Controls Springtime Fine Dust Variability in the Western United States? Investigating the 2002-2015 Increase in Fine Dust in the US Southwest. *Journal of Geophysical Research-Atmospheres* 122, 12449-12467, doi:10.1002/2017jd027208 (2017).

8 Schepanski, K. Transport of Mineral Dust and Its Impact on Climate. *Geosciences* 8, doi:10.3390/geosciences8050151 (2018).

9 Ginoux, P., Prospero, J. M., Gill, T. E., Hsu, N. C. & Zhao, M. Global-scale attribution of anthropogenic and natural dust sources and their emission rates based on MODIS Deep Blue aerosol products. *Reviews of Geophysics* 50, RG3005, doi:10.1029/2012RG000388 (2012).

10 Shao, Y. P. *et al.* Dust cycle: An emerging core theme in Earth system science. *Aeolian Research* 2, 181-204, doi:10.1016/j.aeolia.2011.02.001 (2011).

11 Nonattainment Areas for Criteria Pollutants. United States Environmental Protection Agency: (2019.

12 Wang, J. D. *et al.* Recent global decline in endorheic basin water storages. *Nature Geoscience* 11, 926-+, doi:10.1038/s41561-018-0265-7 (2018).

13 Reynolds, R. L. *et al.* Dust emission from wet and dry playas in the Mojave Desert, USA. *Earth Surface Processes and Landforms* 32, 1811-1827, doi:10.1002/esp.1515 (2007).

14 Mardi, A. H. *et al.* The Lake Urmia environmental disaster in Iran: A look at aerosol pollution. *Science of the Total Environment* 633, 42-49, doi:10.1016/j.scitotenv.2018.03.148 (2018).

15 Bullard, J., Baddock, M., McTainsh, G. & Leys, J. Sub-basin scale dust source geomorphology detected using MODIS. *Geophysical Research Letters* 35, doi:10.1029/2008gl033928 (2008).

16 Reheis, M. C. Dust deposition downwind of Owens (dry) Lake, 1991-1994: Preliminary findings. *Journal of Geophysical Research-Atmospheres* 102, 25999-26008, doi:10.1029/97jd01967 (1997).

17 Reheis, M. C. & Kihl, R. Dust deposition in southern Nevada and California, 1984–1989: Relations to climate, source area, and source lithology. *Journal of Geophysical Research-Atmospheres* 100, 8893-8918, doi:10.1029/94jd03245 (1995).

18 Aciego, S. M. *et al.* Dust outpaces bedrock in nutrient supply to montane forest ecosystems. *Nature Communications* 8, doi:10.1038/ncomms14800 (2017).

19 Reheis, M. C. (U.S. Geological Survey Open-File Report 03-138).

20 Reheis, M. C., Budahn, J. R. & Lamothe, P. J. Geochemical evidence for diversity of dust sources in the southwestern United States. *Geochimica et Cosmochimica Acta* 66, 1569-1587, doi:10.1016/S0016-7037(01)00864-X (2002).

21 Reheis, M. C., Budahn, J. R., Lamothe, P. J. & Reynolds, R. L. Compositions of modern dust and surface sediments in the Desert Southwest, United States. *Journal of Geophysical Research-Earth Surface* 114, F01028, doi:10.1029/2008JF001009 (2009).

22 Paatero, P. & Tapper, U. Positive matrix factorization: A non-negative factor model with optimal utilization of error estimates of data values. *Environmetrics* 5, 111-126, doi:10.1002/env.3170050203 (1994).

23 Brown, S. G., Eberly, S., Paatero, P. & Norris, G. A. Methods for estimating uncertainty in PMF solutions: examples with ambient air and water quality data and guidance on reporting PMF results. *The Science of the Total Environment* 518-519, 626-635, doi:10.1016/j.scitotenv.2015.01.022 (2015).

24 Wedepohl, K. H. The composition of the continental crust. *Geochimica et Cosmochimica Acta* 59, 1217-1232, doi:10.1016/0016-7037(95)00038-2 (1995).

25 Reimann, C. & De Caritat, P. Intrinsic flaws of element enrichment factors (EFs) in environmental geochemistry. *Environmental Science & Technology* 34, 5084-5091, doi:10.1021/es001339o (2000).

26 Okin, G. S. & Reheis, M. C. An ENSO predictor of dust emission in the southwestern United States. *Geophysical Research Letters* 29, doi:10.1029/2001gl014494 (2002).

27 Reheis, M. C. & Urban, F. E. Regional and climatic controls on seasonal dust deposition in the southwestern U.S. *Aeolian Research* 3, 3-21, doi:10.1016/j.aeolia.2011.03.008 (2011).

28 National Centers For Environmental Information: Climate Data Online Accessed at: https://www.ncdc.noaa.gov/cdo-web

29 Pu, B. & Ginoux, P. Climatic factors contributing to long-term variations in surface fine dust concentration in the United States. *Atmospheric Chemistry and Physics* 18, 4201-4215, doi:10.5194/acp-18-4201-2018 (2018).

30 LeBlanc, L. A. & Schroeder, R. A. Transport and distribution of trace elements and other selected inorganic constituents by suspended particulates in the Salton Sea Basin, California, 2001. *Hydrobiologia* 604, 123-135, doi:10.1007/s10750-008-9319-y (2008).

31 Schroeder, R. A., Orem, W. H. & Kharaka, Y. K. Chemical evolution of the Salton Sea, California: nutrient and selenium dynamics. *Hydrobiologia* 473, 23-45, doi:10.1023/A:1016557012305 (2002).

32 Frie, A. L., Dingle, J. H., Ying, S. C. & Bahreini, R. The Effect of a Receding Saline Lake (The Salton Sea) on Airborne Particulate Matter Composition. *Environmental Science & Technology* 51, 8283-8292, doi:10.1021/acs.est.7b01773 (2017).

33 Buck, B. J., King, J. & Etyemezian, V. Effects of Salt Mineralogy on Dust Emissions, Salton Sea, California. *Soil Science Society of America Journal* 75, 1971, doi:10.2136/sssaj2011.0049 (2011).

34 Thorpe, A. & Harrison, R. M. Sources and properties of non-exhaust particulate matter from road traffic: A review. *Science of the Total Environment* 400, 270-282, doi:10.1016/j.scitotenv.2008.06.007 (2008).

35 Iijima, A. *et al.* Particle size and composition distribution analysis of automotive brake abrasion dusts for the evaluation of antimony sources of airborne particulate matter. *Atmospheric Environment* 41, 4908-4919, doi:10.1016/j.atmosenv.2007.02.005 (2007).

36 Querol, X. *et al.* Spatial and temporal variations in airborne particulate matter (PM10 and PM2.5) across Spain 1999-2005. *Atmospheric Environment* 42, 3964-3979, doi:10.1016/j.atmosenv.2006.10.071 (2008).

37 Watson, J. G. & Chow, J. C. Source characterization of major emission sources in the Imperial and Mexicali Valleys along the US/Mexico border. *Science of The Total Environment* 276, 33-47, doi:10.1016/S0048-9697(01)00770-7 (2001).

38 Rael, R. M., Tuazon, E. C. & Frankenberger, W. T. Gas-phase reactions of dimethyl selenide with ozone and the hydroxyl and nitrate radicals. *Atmospheric Environment* 30, 1221-1232, doi:10.1016/1352-2310(95)00447-5 (1996).

39 Gugamsetty, B. *et al.* Source Characterization and Apportionment of PM10, PM2.5 and PM0.1 by Using Positive Matrix Factorization. *Aerosol and Air Quality Research* 12, 476-491, doi:10.4209/aaqr.2012.04.0084 (2012).

40 Kocak, M., Mihalopoulos, N. & Kubilay, N. Origin and source regions of PM10 in the Eastern Mediterranean atmosphere. *Atmospheric Research* 92, 464-474, doi:10.1016/j.atmosres.2009.01.005 (2009).

41 Paatero, P., Eberly, S., Brown, S. G. & Norris, G. A. Methods for estimating uncertainty in factor analytic solutions. *Atmos. Meas. Tech.* 7, 781-797, doi:10.5194/amt-7-781-2014 (2014).

42 Gill, T. E., Gillette, D. A., Niemeyer, T. & Winn, R. T. Elemental geochemistry of wind-erodible playa sediments, Owens Lake, California. *Nuclear Instruments & Methods in Physics Research Section B-Beam Interactions with Materials and Atoms* 189, 209-213, doi:10.1016/S0168-583X(01)01044-8 (2002).

43 Stein, A. F. *et al.* NOAA'S HYSPLIT Atmospheric Transport and Dispersion Modeling System. *Bulletin of the American Meteorological Society* 96, 2059-2077, doi:10.1175/bams-d-14-00110.1 (2015).

44 Pratt, K. A. *et al.* Observation of playa salts as nuclei in orographic wave clouds. *Journal of Geophysical Research: Atmospheres* 115, D15301, doi:10.1029/2009JD013606 (2010).

45 Gaston, C. J. *et al.* Laboratory Studies of the Cloud Droplet Activation Properties and Corresponding Chemistry of Saline Playa Dust. *Environmental Science & Technology* 51, 1348-1356, doi:10.1021/acs.est.6b04487 (2017).

46 Smith, S. M. (1997).

47 Wasklewicz, T. A. & Meek, N. Provenance of aeolian sediment: The upper Coachella Valley, California. *Physical Geography* 16, 539-556, doi:10.1080/02723646.1995.10642570 (1995).

48 Beheiry, S. A. Sand Forms In Coachella-Valley, Southern California. *Annals of the Association of American Geographers* 57, 25-48, doi:10.1111/j.1467-8306.1967.tb00589.x (1967).

49 Tunney, H., Stojanovic, M., Popic, J. M., McGrath, D. & Zhang, C. S. Relationship of soil phosphorus with uranium in grassland mineral soils in Ireland using soils from a long-term phosphorus experiment and a National Soil Database. *Journal of Plant Nutrition and Soil Science* 172, 346-352, doi:10.1002/jpln.200800069 (2009).

50 Schipper, L. A. *et al.* Rates of accumulation of cadmium and uranium in a New Zealand hill farm soil as a result of long-term use of phosphate fertilizer. *Agriculture Ecosystems & Environment* 144, 95-101, doi:10.1016/j.agee.2011.08.002 (2011).

51 Katra, I., Scheidt, S. & Lancaster, N. Changes in active eolian sand at northern Coachella Valley, California. *Geomorphology* 105, 277-290, doi:10.1016/j.geomorph.2008.10.004 (2009).

52 Avecilla, F., Panebianco, J. E. & Buschiazzo, D. E. Meteorological conditions during dust (PM10) emission from a tilled loam soil: Identifying variables and thresholds. *Agricultural and Forest Meteorology* 244, 21-32, doi:10.1016/j.agrformet.2017.05.016 (2017).

53 Goossens, D. Effect of soil crusting on the emission and transport of wind-eroded sediment: field measurements on loamy sandy soil. *Geomorphology* 58, 145-160, doi:10.1016/s0169-555x(03)00229-0 (2004).

54 Goossens, D. & Buck, B. Dust emission by off-road driving: Experiments on 17 arid soil types, Nevada, USA. *Geomorphology* 107, 118-138, doi:10.1016/j.geomorph.2008.12.001 (2009).

55 Hess, A., Tarik, M., Foppiano, D., Edinger, P. & Ludwig, C. Online Size and Element Analysis of Aerosol Particles Released from Thermal Treatment of Wood Samples Impregnated with Different Salts. *Energy & Fuels* 30, 4072-4084, doi:10.1021/acs.energyfuels.6b00174 (2016).

56 Anderson, L. D., Faul, K. L. & Paytan, A. Phosphorus associations in aerosols: What can they tell us about P bioavailability? *Marine Chemistry* 120, 44-56, doi:10.1016/j.marchem.2009.04.008 (2010).

57 Engberg, R. A. Selenium budgets for Lake Powell and the upper Colorado River Basin. *Journal of the American Water Resources Association* 35, 771-786, doi:10.1111/j.1752-1688.1999.tb04173.x (1999).

58 Chan, Y. C. *et al.* Using multiple type composition data and wind data in PMF analysis to apportion and locate sources of air pollutants. *Atmospheric Environment* 45, 439-449, doi:10.1016/j.atmosenv.2010.09.060 (2011).

59 O'Dowd, C. D. & Leeuw, G. d. Marine aerosol production: a review of the current knowledge. *Philosophical Transactions of the Royal Society of London A: Mathematical, Physical and Engineering Sciences* 365, 1753-1774, doi:10.1098/rsta.2007.2043 (2007).

60 de Leeuw, G. *et al.* Production Flux of Sea Spray Aerosol. *Reviews of Geophysics* 49, doi:10.1029/2010rg000349 (2011).

61 Taiwo, A. M., Harrison, R. M. & Shi, Z. B. A review of receptor modelling of industrially emitted particulate matter. *Atmospheric Environment* 97, 109-120, doi:10.1016/j.atmosenv.2014.07.051 (2014).

62 Pan, Y. P. *et al.* Trace elements in particulate matter from metropolitan regions of Northern China: Sources, concentrations and size distributions. *Science of the Total Environment* 537, 9-22, doi:10.1016/j.scitotenv.2015.07.060 (2015).

63 Chang, C. Y., Chiang, H. L., Su, Z. J. & Wang, C. F. A sequential extraction method measures the toxic metal content in fly ash from a municipal solid waste incinerator. *Journal of the Chinese Chemical Society* 52, 921-926, doi:10.1002/jccs.200500128 (2005).

64 Lough, G. C. *et al.* Emissions of metals associated with motor vehicle roadways. *Environmental Science & Technology* 39, 826-836, doi:10.1021/es048715f (2005).

65 Hulskotte, J. H. J., Roskam, G. D. & van der Gon, H. A. C. D. Elemental composition of current automotive braking materials and derived air emission factors. *Atmospheric Environment* 99, 436-445, doi:10.1016/j.atmosenv.2014.10.007 (2014).

66 Kabir, E. *et al.* Current Status of Trace Metal Pollution in Soils Affected by Industrial Activities. *Scientific World Journal*, doi:10.1100/2012/916705 (2012).

67 Gonzalez, R. O. *et al.* New Insights from Zinc and Copper Isotopic Compositions into the Sources of Atmospheric Particulate Matter from Two Major European Cities. *Environmental Science & Technology* 50, 9816-9824, doi:10.1021/acs.est.6b00863 (2016).

68 Sheesley, R. J., Schauer, J. J., Hemming, J. D., Geis, S. & Barman, M. A. Seasonal and spatial relationship of chemistry and toxicity in atmospheric particulate matter using aquatic bioassays. *Environmental Science & Technology* 39, 999-1010, doi:10.1021/es049873+ (2005).

69 Goldstein, H. L., Breit, G. N. & Reynolds, R. L. Controls on the chemical composition of saline surface crusts and emitted dust from a wet playa in the Mojave Desert (USA). *Journal of Arid Environments* 140, 50-66, doi:10.1016/j.jaridenv.2017.01.010 (2017).

70 Schully, B. *et al.* in *Final Panel Report on Fugitive Dust Issues* (Salton Sea Science Office, United States Geological Survey, 2002).

Chapter 4: Brown Carbon Formation from Nighttime Chemistry of Unsaturated Heterocyclic Volatile Organic Compounds

4.0 Acknowledgement of Co-authorship

Credit for this chapter is shared equally between Huanhuan Jiang and Alexander L. Frie. Other contributors include Avi Lavi, Jin Y. Chen, Haofei Zhang, Roya Bahreini, and Ying-Hsuan Lin.

4.1 INTRODUCTION

Aerosol's radiative effects are the most uncertain components of current climate models.[2] One of the drivers of this uncertainty is the incomplete understanding of aerosol formation and aging processes that influence aerosols' chemical composition and optical properties. Light-absorbing organic aerosols, known as brown carbon (BrC), are estimated to account for ~20% of aerosol-driven atmospheric heating.[3] The chemical nature of BrC chromophores has been the focus of many recent studies, with field, laboratory, and modeling studies identifying aromatics, conjugated systems, and highly functionalized species, such as organic nitrates, as moieties responsible for absorption of tropospheric solar radiation.[3-17] Specifically, nitroaromatic compounds have been recognized as significant components of BrC.[14]

One previously unexplored pathway of BrC and nitroaromatic formation is the nitrate radical (NO_3)-initiated oxidation of unsaturated heterocyclic compounds. Unsaturated heterocyclic compounds contain heteroatoms (N, O and S) within their ring structures and represent a unique family of reactive compounds. These compounds are emitted during biomass burning events, with estimated emission factors of 5–37% of total

emitted carbon for furans.[18] High levels of NO_x emissions in biomass burning plumes can readily react with O_3 to form NO_3 radicals, the dominant atmospheric oxidant during nighttime.[15,19,20] Thus, heterocyclic compounds and NO_3 radicals are likely to co-occur in the nighttime atmosphere. Major unsaturated heterocyclic compounds are known to react quickly with NO_3 radicals,[21] forming condensable nitro- or nitrate-containing reaction products that are likely to absorb light in the UV-Visible range.[8,11,22]

Here, the NO_3 oxidation of unsaturated heterocyclic compounds is investigated as a probable and previously unrecognized source of BrC. Through a series of chamber experiments, we characterized chemical and optical properties of SOA from NO_3-initiated oxidation of pyrrole, furan, and thiophene as model compounds for 5-membered unsaturated heterocyclic compounds. We used both online and offline techniques to evaluate single scattering albedo (SSA, λ=375 nm), refractive index (m, λ=375 nm) and mass absorption coefficients (MAC, 290-700 nm) to provide a broad picture of the optical characteristics of SOA. Molecular composition of SOA was analyzed to identify potential chromophores.

4.2 METHODS

4.2.1 Controlled Chamber Experiments

Experiments were performed under dry conditions (RH=2-16%) within a ~1.3 m^3 FEP Teflon chamber located at University of California, Riverside. Before each experiment, the chamber was filled with zero air (Airgas). O_3 was generated through corona discharge (Enaly, 1000BT-12) and injected into the chamber until a concentration of ~1500 ppbv O_3 was reached. Next, 2 L of NO (Praxair, 482 ppmv in air) was injected into the

chamber. The chamber was equilibrated for an hour to allow reservoirs of NO_3 and N_2O_5 to develop. As shown in Figure A1.1, more than 9 ppbv NO_3 can be generated after one hour as simulated using a kinetic box model.[23-25] Then, pyrrole (TCI America, >99%), furan (TCI America, >99%,) or thiophene (Alfa Aesar, 99%) was added into a glass bulb and the vapors were introduced into the chamber by flowing ultra-zero air (Aadco Instruments Inc., 747-30) through the bulb to achieve an effective chamber concentration of ~200 ppbv. Under these conditions, the oxidation of all precursors is dominated by the NO_3 pathway (Table 4.1). Aerosol size distributions, NO_2, NO and O_3 were continuously monitored during experiments with a scanning electron mobility spectrometer (SEMS, Brechtel Manufacturing Inc.), NO_x analyzer (Thermo 42i-LS) and an O_3 analyzer (Thermo 49i), respectively. A summary of experimental conditions is provided in Table 4.2.

Table 4.1. The estimated lifetimes of pyrrole, furan and thiophene in the presence of ~750 ppbv O_3 and ~1000 pptv NO_3 radicals

Rate constants	pyrrole	furan	thiophene
k (with $\mathbf{O_3}$) (cm^3 $molecule^{-1}$ s^{-1}) [21]	1.6×10^{-17}	2.4×10^{-18}	$<6\times10^{-20}$
k (with $\mathbf{NO_3}$) in (cm^3 $molecule^{-1}$ s^{-1}) [21]	4.9×10^{-11}	1.4×10^{-12}	3.2×10^{-14}
lifetime for the reaction with $\mathbf{O_3}$ (s)	3.4×10^{3}	2.3×10^{4}	$>9.0\times10^{5}$
lifetime for the reaction with $\mathbf{NO_3}$ (s)	8.3×10^{-1}	2.9×10^{1}	1.3×10^{3}

Table 4.2 Summary of experimental conditions and results.

Precursor	$[O_3]_{eq}$ [a] ppb	$[NO_x]_{eq}$ [b] ppb	AM_{max} [c] μg m^{-3}	$Å_{290/550}$ [d]	Average $Å_{290/550}$ [e]	<MAC> [f] $cm^2\ g^{-1}$	Average <MAC> [g] $cm^2\ g^{-1}$	n_{375} [h]	k_{375} [h]	SSA_{375} [i]
Pyrrole	750	350	558	5.83	5.71±0.29	3,720	3,370±670	1.41 ± 0.03	0.017 ± 0.002	0.86 ± 0.01
Pyrrole	1200	300	770	5.93		2,600		1.34 ± 0.04	0.013 ± 0.002	0.86 ± 0.01
Pyrrole	1160	310	615	5.38		3,800		1.40 ± 0.01	0.014 ± 0.003	0.87 ± 0.011
Furan	590	330	17	7.81	6.78±1.12	1,330	1,070±240	- [j]	- [j]	- [j]
Furan	560	160	43	6.95		850		-	-	-
Furan	800	170	47	5.59		1,040		-	-	-
Thiophene	530	350	264	5.70	5.50±0.18	2,610	2,950±470	1.44 ± 0.01	0.003 ± 0.002	0.98 ± 0.01
Thiophene	420	280	218	5.34		2,770		1.45 ± 0.01	0.002 ± 0.001	0.98 ± 0.01
Thiophene	750	330	285	5.47		3,480		1.47 ± 0.02	0.003 ± 0.002	0.98 ±0.01

[a] $[O_3]_{eq}$: the measured equilibrium O_3 concentration.
[b] $[NO_x]_{eq}$: the measured equilibrium NO_x concentration.
[c] AM_{max}: the maximum aerosol mass concentration during the experiment.
[d] $Å_{290/550}$: the absorption Ångström exponent calculated using the MAC at 290 nm and 550 nm.
[e] Average $Å_{290/550}$: the average $Å_{290/550}$ calculated from triplicate experiments± the corresponding standard deviation.
<MAC>: the averaged MAC over the range of 290-700 nm, as calculated by Eq. (4.3).
[f] Average <MAC>: the average <MAC> value calculated from triplicate experiments ± the corresponding standard deviation.
[g] n_{375} and k_{375}: the averaged n_{375} and k_{375} over the experiment when mode changed <10 % in consecutive SEMS runs and optical coefficients were above PAX detection limits.
[h] SSA_{375}: the averaged SSA_{375} over the experiment when x_{375}>1.
[i] During the furan experiment, more than 50% of $\beta_{abs,375}$ measurements were below the PAX detection limit with the remaining values being only marginally higher. Thus, n_{375}, k_{375} and SSA_{375} were not reported for furan experiment.

4.2.2 Online Chemical and Optical Characterization

Gas-phase reaction products were analyzed in real time by an iodide-adduct high-resolution time-of-flight chemical ionization mass spectrometer (HR-ToF-CIMS, Tofwerk AG, Aerodyne Research Inc.) with iodide (I^-) as a reagent ion. I^- ions were introduced into the ion-molecule reaction region of the HR-ToF-CIMS by first passing dry N_2 over a diffusion tube filled with methyl iodide, then passing the flow through a ^{210}Po radiation source (NRD) and into the ion molecule reaction region (IMR) of the instrument. To humidify the sample stream, a 0.5 L min^{-1} nitrogen stream humidified with a bubbler was mixed with the sample stream prior to the inlet. The total inlet flow of CIMS was 2.2 L min^{-1}. The operating pressures of the instrument were as follows: the IMR region at 100 ± 2 mbar, the SSQ region at ~2.2 mbar, the BSQ region at ~0.01 mbar, and the TOF region at ~10^{-6} mbar.

Scattering and absorption coefficients at 375 nm ($\beta_{scat,375}$ and $\beta_{abs,375}$) were measured at 1 Hz using a photoacoustic extinctiometer (PAX) (Droplet Measurement Technologies, Boulder, CO). PAX measurements were averaged to the SEMS scan time (140 s). PAX detection limits, defined as 3 times the standard deviation of scattering and absorption measurements of filtered air averaged to 140 s, were 1.29 Mm^{-1} and 1.08 Mm^{-1}, respectively for $\beta_{scat,375}$ and $\beta_{abs,375}$. The single scattering albedo at 375 nm (SSA_{375}) was calculated using Eq. 4.1.

$$SSA_{375} = \frac{\beta_{scat,375}}{\beta_{scat,375}+\beta_{abs,375}} \quad (4.1)$$

The size parameter (x) is useful in understanding SSA dynamics due to SSA's dependency on particle size and measurement wavelength. x relates the mode diameter of the size distribution (d_{mode}) to the corresponding wavelength (λ) of optical measurements, i.e., λ=375 nm for PAX, as shown in Eq. 4.2.

$$x_\lambda = \frac{\pi d_{mode}}{\lambda} \tag{4.2}$$

4.2.3 Calculation of Refractive Index

RI values are measures of the interactions of a material with radiation. The RI consists of two components, a real component which describes scattering (n) and an imaginary component which describes absorption (k). RI values were calculated using an optical closure procedure and applying Mie Theory.[26-30] RI values were calculated by minimizing the absolute difference between the observed and theoretical optical coefficients of a size distribution over a range of RI inputs, at times when the mode change between consecutive SEMS measurements was lower than 10%.[26-29] For pyrrole and thiophene experiments, n_{375} and k_{375} values were calculated when PAX measurements were above the detection limits for both $\beta_{scat,375}$ and $\beta_{abs,375}$. Additional Details are included in appendix 3.

Uncertainties in refractive index values were calculated by forcing calculation inputs by instrumental uncertainties to the most extreme value. For example, the lower bounds of k values are determined by maximizing particle diameter and particle count, and minimizing observed absorption. Uncertainties used in these calculations were 6 % for absorption coefficients, 4.5% for scattering coefficients, 3% for particle diameter, and 10% for particle count.[31] Uncertainties associated with the first and last calculations of refractive

indices for each experiment are included in Table 4.3. Average observed uncertainties were $k^{+0.004}_{-0.003}$ and $n^{+0.06}_{-0.05}$ for pyrrole as $k^{+0.001}_{-0.001}$ and $n^{+0.07}_{-0.06}$ for Thiophene.

Table 4.3. Estimated uncertainties in calculated refractive index values for the initial and final refractive index calculations. Table order corresponds to that of Table 4.2.

Precursor	Initial k_{375}	Final k_{375}	Initial n_{375}	Final n_{375}
Pyrrole	$0.023^{+0.007}_{-0.005}$	$0.015^{+0.004}_{-0.003}$	$1.45^{+0.08}_{-0.06}$	$1.37^{+0.06}_{-0.05}$
Pyrrole	$0.018^{+0.005}_{-0.004}$	$0.012^{+0.003}_{-0.003}$	$1.43^{+0.07}_{-0.06}$	$1.31^{+0.04}_{-0.04}$
Pyrrole	$0.004^{+0.001}_{-0.001}$	$0.015^{+0.004}_{-0.003}$	$1.41^{+0.07}_{-0.05}$	$1.40^{+0.06}_{-0.04}$
Thiophene	$0.009^{+0.003}_{-0.002}$	$0.002^{+0.001}_{-0.000}$	$1.41^{+0.08}_{-0.06}$	$1.45^{+0.07}_{-0.06}$
Thiophene	$0.007^{+0.003}_{-0.001}$	$0.002^{+0.001}_{-0.000}$	$1.45^{+0.08}_{-0.06}$	$1.43^{+0.07}_{-0.05}$
Thiophene	$0.009^{+0.004}_{-0.002}$	$0.04^{+0.001}_{-0.001}$	$1.44^{+0.09}_{-0.06}$	$1.43^{+0.07}_{-0.05}$

4.2.4 Offline Optical Characterization

Aerosol samples were collected onto polytetrafluoroethylene membrane filters (Zefluor, Pall Laboratory, 47 mm, 1.0 μm pore size), after the particle volume concentration peaked. Filters were extracted in methanol and analyzed for UV-Vis absorbance (Beckman DU-640). This process is further detailed in the appendix 3.

4.2.5 Calculation of Mass Absorption Coefficient and Absorption Angstrom Exponent

Calculation of the solution-based MAC from UV-Vis spectra has been reported previously.[32,33] The effective MAC ($cm^2\ g^{-1}$) is calculated using Eq 4.3.[32,33]

$$\mathrm{MAC}(\lambda) = \frac{\mathrm{A}(\lambda)\times \ln 10}{b \times C_{\mathrm{m}}} \tag{4.3}$$

where $\mathrm{A}(\lambda)$ is the absorbance at wavelength (λ) of filter extracts, b is the path length (1 cm), and C_{m} ($g\ cm^{-3}$) is the mass concentration of extracted SOA compounds in solution. C_{m} is determined by the filter sampling flow rate, average aerosol mass concentration during filter collection, sampling time, and extraction efficiency. The light-absorbing

properties of aerosols are estimated by the average MAC (expressed as <MAC>) over the wavelengths range of 290–700 nm (λ_{upper}-λ_{lower}), as shown in Eq 4.4.

$$\langle MAC \rangle = \frac{\int_{\lambda_{lower}}^{\lambda_{upper}} \mathrm{MAC}(\lambda) d\lambda}{\lambda_{upper} - \lambda_{lower}} \tag{4.4}$$

To understand the wavelength dependence of absorption, the absorption Angstrom (Å) exponent from 290 to 550 nm was estimated (Eq. 4.5).[33]

$$\mathrm{Å}_{290/550} = \frac{-ln(\frac{MAC(290nm)}{MAC(550nm)})}{ln(\frac{290nm}{550nm})} \tag{4.5}$$

4.2.6 Offline Chemical Characterization

The molecular composition of filter extracts was characterized using liquid chromatography (LC) coupled with a diode array detector (DAD) and a high-resolution time-of-flight mass spectrometer (HR-TOFMS, Agilent 6230 Series). The instrument was equipped with an electrospray ionization source (ESI), and the detector was operated under the negative (−) ion mode. The TOFMS acquired mass spectra from *m/z* 63-1050. The chromatographic separations were carried out using Waters XBridge BEH C-18 column (2.1mm ID, 50 mm length, 2.5 um particle size) at 45°C. The mobile phases consisted of eluent (A) 0.1% acetic acid in water and eluent (B) 0.1% formic acid in methanol. The applied 15-min gradient elution program was as follows: the concentration of eluent B was 0% for the first 2 min, increased to 90% from 2-12 min, held at 90% from 12-14 min, and then decreased back to 0% from 14-15 min, and held at 0% from 15-20 min. The post-run time was 2 min. The LC flow rate and injected sample volume were 0.25 mL min^{-1} and 20 µL, respectively. Prior to LC-DAD-ESI-HR-TOFMS analysis, the TOFMS instrument was

calibrated using a commercially available ESI-L low concentration tuning mixture (Agilent Technology, Part number G1969-85000). This external calibration was done in the low-mass range (m/z <1700) mode.

4.2.7 Secondary Organic Aerosol Yield

SOA yield was calculated as shown in Eq. 4.6.

$$Y_{SOA} = \frac{\rho \times \mathrm{OA_{Vol}}}{(m_{VOC}/V_{\mathrm{cham}})} \quad (4.6)$$

where Y_{SOA} is the aerosol yield, ρ is the assumed aerosol density (1.3 µg cm^{-3}),[34] OA_{vol} is the volume concentration in µl m^{-3}, m_{VOC} (µg) is the mass of VOC injected into the chamber, and V_{cham} (m^3) is the estimated volume of the chamber. $V_{cham.}$ uncertainty was assumed to be 0.3 m^3 and density uncertainty 0.15 µg cm^{-3}. Uncertainties in the m_{VOC} were assumed to be the smallest unit of measurement on the injection syringe (0.1 µl) multiplied by the dentisty of the VOC injected. Uncertainties in the OA_{vol} were calculated as the standard deviation of OA_{vol} within the 3 experimental replicates.

4.2.8 Total Potential SOA and Absorption Cross-Section Emission Factors

To estimate the relative importance of each precursor to SOA mass, the potential for SOA production (SOA_{pot}, g of SOA potentially produced per kg of fuel burned) from the NO_3 oxidation of furan, pyrrole, and thiophene released from 6 fuels are calculated (Table 4.3), as shown in Eq. 4.7.

$$\mathrm{SOA_{pot}} = \left(\frac{EF_C}{F_C}\right) \times Y_{\mathrm{SOA}} \quad (4.7)$$

where EF_c is the carbon emission factor in g kg^{-1} reported by Hatch et al. (2015),[18] F_c is the fraction of molecular weight accounted by carbon, and Y_{SOA} is the SOA yield estimated in this study.

To estimate the relative importance of each precursor to the SOA absorption cross-section in burning of a specific fuel, we calculate the absorption cross-section emission factor (EF_{absC}, cm^2 of absorption per kg of fuel burned) (Table 4.4), using SOA_{pot} and our <MAC> values, as shown in Eq. 4.8.

$$EF_{absC} = \left(\frac{EF_C}{F_c}\right) \times Y_{SOA} \times < MAC > = SOA_{pot} \times < MAC > \quad (4.8)$$

4.3 Results and Discussion

4.3.1 NO_3-Initiated SOA Formation from Heterocyclic Precursors

By assuming all of the injected VOC reacted with NO_3 radicals and propagating experimental uncertainties, the lower bound of SOA yields (Eq. 4.6) were estimated to be 109 ± 29 % for pyrrole, 7 ± 3% for furan, and 35 ± 8% for thiophene, assuming a density of 1.3 g cm^{-3}.[34] These values are estimates and are likely inter-comparable, but caution should be used when comparing to more quantitative yield measures from other studies due to our small chamber size and potentially high particle wall-loss rates.

The low SOA mass production from furan is consistent with the low SOA yields from OH oxidation of furan reported in other studies.[35,36] Together these observations reveal that furan may not be a major contributor to SOA mass under a variety of common oxidation conditions. Conversely, the larger SOA mass formed from thiophene and pyrrole indicates that NO_3 chemistry with these compounds may be an important SOA source, particularly in biomass burning plumes where these compounds are readily found.[18]

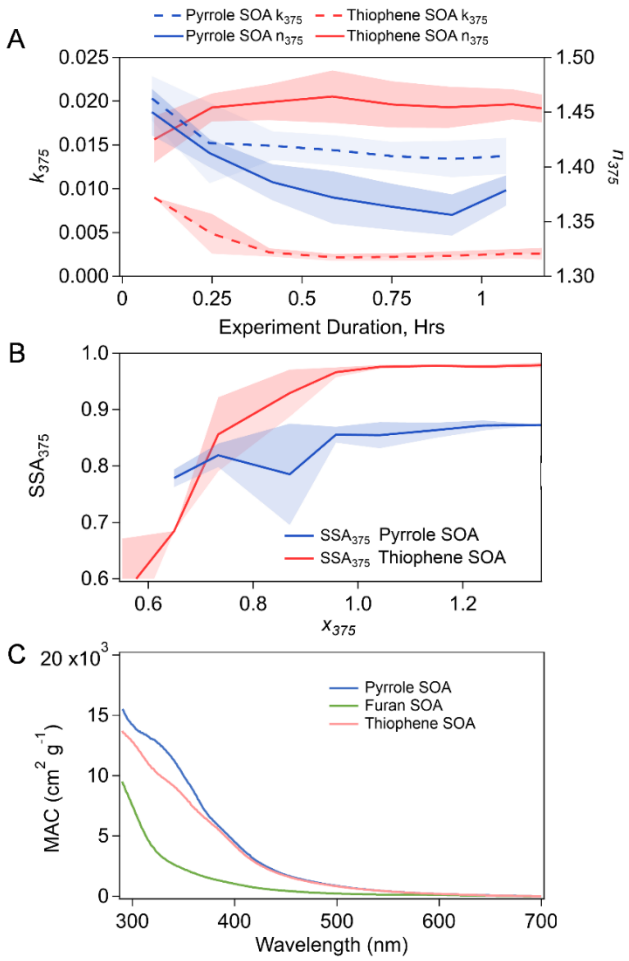

Figure 4.1 (A) Calculated refractive indices of pyrrole and thiophene SOA over the course of experiments. (B) Single scattering albedo values for pyrrole and thiophene relative to the size parameter at 375 nm (x_{375}). Values shown are averaged over all experiments for the given compound. Shaded areas represent 1 standard deviation and describe that variability between experiments. (C) Mass absorption coefficients (MAC) as a function of wavelength for pyrrole-, furan-, thiophene-derived SOA.

4.3.2 Optical Properties of SOA

SSA_{375}, n_{375}, and k_{375} for pyrrole and thiophene experiments are displayed in Figure 4.1A and 4.1B. For the following discussion, SSA_{375} values are averaged for all measurements where $x_{375}>1$ because the size dependency of SSA is expected to be minimal within this region.[37] The n_{375} values fell within the ranges previously observed for organic

aerosols, with average values of 1.41 ± 0.05, and 1.44 ± 0.02 for pyrrole and thiophene SOA, respectively.

Pyrrole SOA was the most absorbing among the three tested precursors, with an average SSA_{375} of 0.86±0.01 and k_{375} of 0.015±0.003. These values are similar to those previously observed for peat biomass burning (SSA_{375}: 0.93 and 0.85, and k_{375}: 0.009–0.015 depending on fuel packing density) by Sumlin et al. (2018).[38] Notably, the k_{375} values for pyrrole SOA decreased with exposure time and seem to be inversely related to SOA mass. This decrease in k_{375} could be driven by dilution of chromophores as more scattering components condense or by bleaching of existing chromophores. Bleaching might be driven by the oxidation of conjugated species by an oxidant (O_3 or NO_3) or particle phase processes such as hydrolysis of organonitrates.[39]

Thiophene SOA was slightly absorbing, with an average SSA_{375} of 0.98±0.01 and k_{375} of 0.003 ± 0.002. Thiophene k_{375} values are similar to those observed by Liu et al. (2015)[22] for toluene SOA (k_{405}=0.0041±0.0005) and *m*-xylene SOA (k_{405}=0.0030 ±0.0003) formed from OH oxidation in the presence of NO_x.[22] These compounds are aromatic anthropogenic proxies, indicating that thiophene SOA products have similar absorption properties to SOA from anthropogenic precursors.

The majority of $\beta_{abs,375}$ measurements for furan SOA were below the PAX detection limit, which was likely caused by the low mass production of furan SOA in the chamber (Section 4.1) and its low light absorption at 375 nm (Section 4.3).

4.3.3 The Absorption Spectra of BrC

Similar to previously studied BrC SOA, samples collected from oxidation of unsaturated heterocyclic compounds absorb strongly in UV and near UV ranges, and the absorbance decreased as the wavelengths increased (Figure 4.1C).[16,17] The absorbance spectra of pyrrole and thiophene SOA showed a shoulder at ~330 nm. The <MAC> values of pyrrole, thiophene and furan SOA averaged over 290-700 nm were 3,370±670 $cm^2\ g^{-1}$, 2,950±470 $cm^2\ g^{-1}$, and 1,070±240 $cm^2\ g^{-1}$, respectively (Table 4.2). Notably, the offline MAC of furan SOA over the whole spectra and at 375 nm was significantly lower than in the other systems, which explains its negligible $\beta_{abs,375}$ values (Section 4.2). These <MAC> are much higher than those of SOA (200–500 $cm^2\ g^{-1}$) derived from biogenic and anthropogenic VOCs under low or intermediate NO_x conditions, but similar to the SOA from anthropogenic VOCs with high NO_x (VOC/NO_x<5 ppbC/ppb) conditions (Table A4.1).[32,40-42] The average $Å_{290/550}$ of pyrrole SOA (5.71±0.29) was similar to thiophene SOA (5.50±0.18), but lower than furan SOA (6.78±1.12) (Table 4.2).

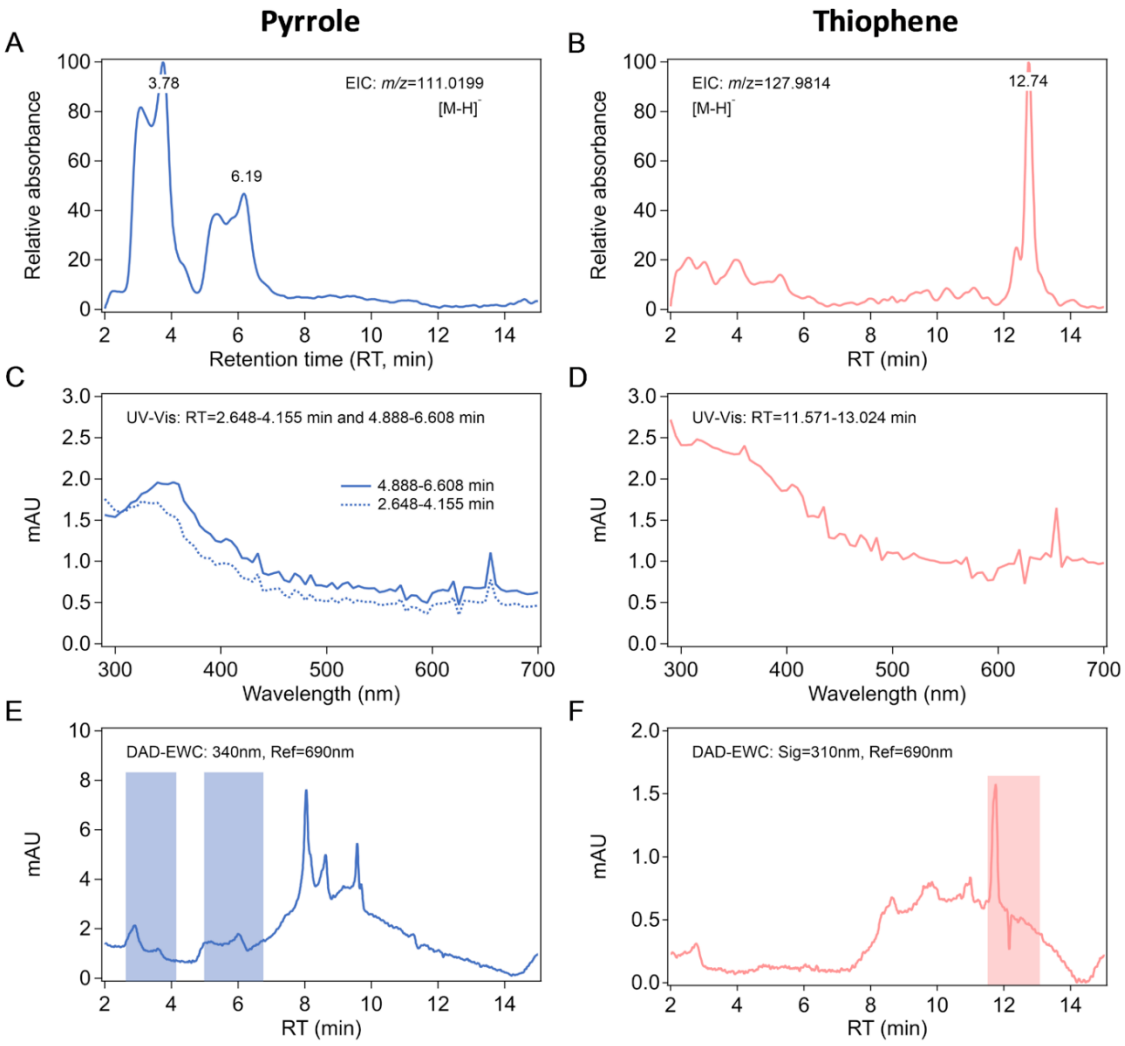

Figure 4.2 The extracted ion chromatograms (EICs) for (A) $C_4H_4N_2O_2$ in pyrrole SOA and (B) $C_4H_3NO_2S$ in thiophene SOA, the extracted UV-Vis spectra (mAU, milli-Absorbance) of (C) pyrrole SOA at RT=2.648-4.155 min and RT=4.888-6.608 min and (D) thiophene SOA at RT=11.571-13.024 min, and the extracted wavelength chromatograms (EWCs) for (E) pyrrole SOA and (F) thiophene SOA.

4.3.4 Molecular Composition of BrC

Potential chromophores such as nitropyrrole ($C_4H_4N_2O_2$), and nitrothiophene ($C_4H_3NO_2S$) were observed in the SOA extracts by LC-DAD/ESI-HR-TOFMS (Figure 4.2A and 2B), and the presence of nitropyrrole in the gas phase was confirmed by the HR-ToF-CIMS data (Figure A1.2). Nitrofuran was not detectable by LC/ESI-MS likely due to

the low mass yield of furan SOA. For nitropyrrole, multiple isomers were present (i.e., 2- and 3-nitropyrrole) and the extracted ion chromatograms (EIC) showed two major peaks (3.78 min and 6.19 min).

The extracted UV-Vis spectra of pyrrole SOA (RT=2.648-4.155 min and 4.888-6.608 min) and thiophene SOA (RT=11.571-13.024 min) showed significant absorption in the range of 300-350 nm (Figures 2C and 2D). For comparison, the UV-Vis spectra of two standard compounds (i.e., 2-nitropyrrole and 2-nitrothiophene) were measured (Figure A1.3) and peaked at 337 nm and 314 nm, respectively. These peaks are consistent with the substantial absorption by the corresponding extracts of pyrrole and thiophene SOA in similar wavelength ranges. Furthermore, the extracted wavelength chromatograms (EWC) of pyrrole and thiophene SOA (Figures 4.2E and 4.2F) peak at the times of nitropyrrole and nitrothiophene elution (Figures 4.2A and 4.2B). This evidence confirms the contribution of nitro-containing heterocyclic compounds and their isomers to the observed <MAC> values of SOA in this study.

Organonitrates are also potential chromophores in pyrrole and thiophene SOA. Liu et al. suggested that organonitrates could contribute significantly to the absorption of visible light.[8] In this study, organonitrates were not detected by LC/ESI-MS, probably due to the hydrolysis of ONO_2 groups in aqueous solutions during the sample workup and analysis procedure.[43] However, some organonitrates, such as nitrate-thiophene, nitrate-pyrrole, and nitrate-furan, were detected in the gas phase by HR-ToF-CIMS. (Figure A1.2). Additionally, multiple unidentified absorption peaks in EWCs of pyrrole SOA (RT=8-10 min) and thiophene SOA (RT=9-11 min) reveal possible unknown chromophores.

4.4 Atmospheric Implications

This study demonstrates that the NO_3-initiated oxidation of unsaturated heterocyclic compounds is a source of secondary BrC. This pathway reveals a new source of nitroaromatic compounds in BrC aerosols and adds to our understanding of nighttime organic aerosol browning.[14,15] Considering the relatively high emission factors of pyrrole (up to 0.11 g/kg), thiophene (up to 0.01 g/kg) and furan (up to 0.31 g/kg) from burning of various fuels,[18] BrC from the oxidation of these precursors may be ubiquitous in biomass burning plumes.

To estimate the relative importance of each precursor to the ambient SOA and light absorption, the potential of SOA production (SOA_{pot}, g of SOA potentially produced per kg of fuel burned, Eq. 4.7, Table 4.4) and absorption cross-section emission factor (EF_{absC}, cm^2 of absorption per kg of fuel burned, Eq. 4.8, Table 4.5) were calculated for the six fuels burned by Hatch et al (2015),[18] assuming the precursors are all consumed through the NO_3 pathway. Pyrrole's SOA_{pot} is at least twice and its EF_{absC} is at least an order of magnitude more than those of furan and thiophene for tested fuels. The EF_{absC} of toluene, a VOC with a relatively high emission factor, was also estimated as a reference; pyrrole's SOA_{pot} and EF_{absC} are comparable to those of toluene for these six fuels.[18,41,44] Furthermore, SOA_{pot} from the NO_3 oxidation of furan, pyrrole, and thiophene was 5-23% that of the SOA_{pot} from the OH oxidation of all biomass burning SOA precursors estimated by Hatch et al. (2015).[18] These results demonstrate that SOA from heterocyclic precursors, particularly pyrrole, may significantly contribute to nighttime SOA production and SOA light absorption.

Effects of nighttime atmospheric processing on heterocyclic VOCs and its potential to produce BrC SOA are currently understudied. Future research is warranted to quantify nitro and organonitrate products from this group of precursors in ambient samples, study their fates and reactivities, and model their formation processes.

Table 4.4 The potential SOA production (SOA_{pot}, g kg^{-1}) from the NO_3 oxidation of pyrrole, furan, thiophene and toluene released from fuel burning. The SOA_{pot} is calculated assuming all VOC is consumed.

Precursor+oxidant	Black Spruce	Ponderosa Pine	Giant Cutgrass	Wire Grass	Rice Straw	Indonesian Peat
Pyrrole+NO_3	0.063	0.168	0.035	0.021	0.076	0.084
Furan+NO_3	0.023	0.031	0.002	0.006	0.008	0.031
Thiophene+NO_3	0.002	0.003	0.004	0*	0.002	0.006
Toluene+high NO_x**	0.031	0.037	0.008	0.002	0.011	0.069
All VOCs+OH [18]	1.37	1.70	0.29	0.12	0.40	2.15

* No thiophene emissions were observed for the burning of wire grass.
** The Y_{SOA} of toluene under high NO_x conditions (VOC/NO_x=5 ppbC/ppb) was taken from the study of Jiang et al.[44] Note that the Y_{SOA} of toluene could be even lower at lower VOC/NO_x ratios.

Table 4.5 Absorption cross-section emission factor (EF_{absC}, $cm^2\ kg^{-1}$) of aerosols derived from the NO_3 oxidation of pyrrole, furan, thiophene and toluene released from fuel burning.

Precursor+oxidant	Black Spruce	Ponderosa Pine	Giant Cutgrass	Wire Grass	Rice Straw	Indonesian Peat
Pyrrole+NO_3	214	566	117	69	255	283
Furan+NO_3	25	33	2	7	9	33
Thiophene+NO_3	6	8	12	0	5	18
Toluene+high NO_x**	94	110	23	7	33	209

* No thiophene emissions were observed for the burning of wire grass.
** The <MAC> of high-NO_x toluene SOA was taken from the study of Liu et al.[41] Note that the VOC/NO_x=1.2-1.5, but Liu et al. did not report the corresponding Y_{SOA} values under these conditions.

4.5 Works Cited

1 Jiang, H. *et al.* Brown Carbon Formation from Nighttime Chemistry of Unsaturated Heterocyclic Volatile Organic Compounds. *Environmental Science & Technology Letters* **6**, 184-190, doi:10.1021/acs.estlett.9b0001710.1021/acs.estlett.9b00017</p> (2019).

2 Pachauri, R. K., Allen, M. R. , Barros, V. R. , Broome, J. , Cramer, W. , Christ, R. , Church, J. A. , Clarke, L. , Dahe, Q. , Dasgupta, P. , Dubash, N. K. , Edenhofer, O. , Elgizouli, I. , Field, C. B. , Forster, P. , Friedlingstein, P. , Fuglestvedt, J. , Gomez-Echeverri, L. , Hallegatte, S. , Hegerl, G. , Howden, M. , Jiang, K. , Jimenez Cisneroz, B. , Kattsov, V. , Lee, H. , Mach, K. J. , Marotzke, J. , Mastrandrea, M. D. , Meyer, L. , Minx, J. , Mulugetta, Y. , O'Brien, K. , Oppenheimer, M. , Pereira, J. J. , Pichs-Madruga, R. , Plattner, G. K. , Pörtner, H. O. , Power, S. B. , Preston, B. , Ravindranath, N. H. , Reisinger, A. , Riahi, K. , Rusticucci, M. , Scholes, R. , Seyboth, K. , Sokona, Y. , Stavins, R. , Stocker, T. F. , Tschakert, P. , van Vuuren, D. and van Ypserle, J. P. . *Climate Change 2014: Synthesis report. Contribution of Working Groups I, II and III to the Fifth Assessment Report of the Intergovernmental Panel on Climate Change*. (IPCC, 2014).

3 Feng, Y., Ramanathan, V. & Kotamarthi, V. R. Brown Carbon: A Significant Atmospheric Absorber of Solar Radiation? *Atmos. Chem. Phys.* **13**, 8607-8621, doi:10.5194/acp-13-8607-2013 (2013).

4 Lavi, A. *et al.* Characterization of Light-Absorbing Oligomers from Reactions of Phenolic Compounds and Fe(III). *ACS Earth and Space Chemistry* **1**, 637-646, doi:10.1021/acsearthspacechem.7b00099 (2017).

5 Zhang, X. L. *et al.* Light-absorbing Soluble Organic Aerosol in Los Angeles and Atlanta: A Contrast in Secondary Organic Aerosol. *Geophys. Res. Lett.* **38**, doi:10.1029/2011gl049385 (2011).

6 Zhang, X. L., Lin, Y.-H., Surratt, J. D. & Weber, R. J. Sources, Composition and Absorption Ångström Exponent of Light-absorbing Organic Components in Aerosol Extracts from the Los Angeles Basin. *Environ. Sci. Technol.* **47**, 3685-3693, doi:10.1021/es305047b (2013).

7 Sun, H., Biedermann, L. & Bond, T. C. Color of Brown Carbon: A Model for Ultraviolet and Visible Light Absorption by Organic Carbon Aerosol. *Geophys. Res. Lett.* **34**, L17813, doi:10.1029/2007GL029797 (2007).

8 Liu, S. *et al.* Hydrolysis of Organonitrate Functional Groups in Aerosol Particles. *Aerosol Sci. Technol.* **46**, 1359-1369, doi:10.1080/02786826.2012.716175 (2012).

9 Nakayama, T. *et al.* Wavelength Dependence of Refractive Index of Secondary Organic Aerosols Generated during the Ozonolysis and Photooxidation of α-Pinene. *Sola* **8**, 119-123, doi:10.2151/sola.2012-030 (2012).

10 Lu, J. W., Flores, J. M., Lavi, A., Abo-Riziq, A. & Rudich, Y. Changes in the Optical Properties of Benzo[a]pyrene-Coated Aerosols upon Heterogeneous Reactions with NO2 and NO3. *Phys. Chem. Chem. Phys.* **13**, 6484-6492, doi:10.1039/C0CP02114H (2011).

11 Jacobson, M. Z. Isolating Nitrated and Aromatic Aerosols and Nitrated Aromatic Gases as Sources of Ultraviolet Light Absorption. *J. Geophys. Res-Atmos.* **104**, 3527-3542, doi:10.1029/1998JD100054 (1999).

12 Claeys, M. *et al.* Chemical Characterisation of Humic-like Substances from Urban, Rural and Tropical Biomass Burning Environments using Liquid Chromatography with UV/vis Photodiode Array Detection and Electrospray Ionisation Mass Spectrometry. *Environ. Chem.* **9**, 273-284, doi:10.1071/EN11163 (2012).

13 Desyaterik, Y. *et al.* Speciation of "Brown" Carbon in Cloud Water Impacted by Agricultural Biomass Burning in Eastern China. *J. Geophys. Res.-Atmos.* **118**, 7389-7399, doi:10.1002/jgrd.50561 (2013).

14 Lin, P. *et al.* Molecular Chemistry of Atmospheric Brown Carbon Inferred from a Nationwide Biomass Burning Event. *Environ. Sci. Technol.* **51**, 11561-11570, doi:10.1021/acs.est.7b02276 (2017).

15 Bluvshtein, N. *et al.* Broadband Optical Properties of Biomass-burning Aerosol and Identification of Brown Carbon Chromophores. *J. Geophys. Res-Atmos.* **122**, 2016JD026230, doi:10.1002/2016JD026230 (2017).

16 Laskin, A., Laskin, J. & Nizkorodov, S. A. Chemistry of Atmospheric Brown Carbon. *Chem. Rev.* **115**, 4335-4382, doi:10.1021/cr5006167 (2015).

17 Moise, T., Flores, J. M. & Rudich, Y. Optical Properties of Secondary Organic Aerosols and Their Changes by Chemical Processes. *Chem. Rev.* **115**, 4400-4439, doi:10.1021/cr5005259 (2015).

18 Hatch, L. E. *et al.* Identification and Quantification of Gaseous Organic Compounds Emitted from Biomass Burning using Two-Dimensional Gas Chromatography-time-of-flight Mass Spectrometry. *Atmos. Chem. Phys.* **15**, 1865-1899, doi:10.5194/acp-15-1865-2015 (2015).

19 Stockwell, C. E. *et al.* Trace Gas Emissions from Combustion of Peat, Crop Residue, Domestic Biofuels, Grasses, and Other Fuels: Configuration and Fourier Transform Infrared (FTIR) Component of the Fourth Fire Lab at Missoula Experiment (FLAME-4). *Atmos. Chem. Phys.* **14**, 9727-9754 (2014).

20 Brown, S. S. & Stutz, J. Nighttime Radical Observations and Chemistry. *Chem. Soc. Rev.* **41**, 6405-6447, doi:10.1039/c2cs35181a (2012).

21 Atkinson, R., Aschmann, S. M., Winer, A. M. & Carter, W. P. Rate Constants for the Gas-phase Reactions of Nitrate Radicals with Furan, Thiophene, and Pyrrole at 295+/-1 K and Atmospheric Pressure. *Environ. Sci. Technol.* **19**, 87-90 (1985).

22 Liu, P. *et al.* Ultraviolet and Visible Complex Refractive Indices of Secondary Organic Material Produced by Photooxidation of the Aromatic Compounds Toluene and m-Xylene. *Atmos. Chem. Phys.* **15**, 1435-1446 (2015).

23 Jenkin, M. E., Saunders, S. M., Wagner, V. & Pilling, M. J. Protocol for the Development of the Master Chemical Mechanism, MCM v3 (Part B): Tropospheric Degradation of Aromatic Volatile Organic Compounds. *Atmos. Chem. Phys.* **3**, 181-193, doi:10.5194/acp-3-181-2003 (2003).

24 Carter, W. P. L. *et al.* Atmospheric Chemistry and Chemical Mechanisms. 2 (University of California, Riverside SRI International, Environment Canada, 1999).

25 Carter, W. P. L. A Detailed Mechanism for the Gas-phase Atmospheric Reactions of Organic Compounds. *Atmos. Environ. A- Gen.* **24**, 481-518, doi:https://doi.org/10.1016/0960-1686(90)90005-8 (1990).

26 Denjean, C. *et al.* A new experimental approach to study the hygroscopic and optical properties of aerosols: application to ammonium sulfate particles. *Atmos. Meas. Tech.* **7**, 183-197, doi:10.5194/amt-7-183-2014 (2014).

27 Denjean, C. *et al.* Aging of secondary organic aerosol generated from the ozonolysis of alpha-pinene: effects of ozone, light and temperature. *Atmos. Chem. Phys.* **15**, 883-897, doi:10.5194/acp-15-883-2015 (2015).

28 De Haan, D. O. *et al.* Brown Carbon Production in Ammonium- or Amine-Containing Aerosol Particles by Reactive Uptake of Methylglyoxal and Photolytic Cloud Cycling. *Environ. Sci. Technol.* **51**, 7458-7466, doi:10.1021/acs.est.7b00159 (2017).

29 Zarzana, K. J., Cappa, C. D. & Tolbert, M. A. Sensitivity of Aerosol Refractive Index Retrievals Using Optical Spectroscopy. *Aerosol Sci. Technol.* **48**, 1133-1144, doi:10.1080/02786826.2014.963498 (2014).

30 Bohren, C. F. & Huffman, D. R. *Absorption and Scattering of Light by Small Particles*. (John Wiley & Sons, 2008).

31 Dingle, J. H., Zimmerman, Stephen, Frie, Alexander L. , Min, Justin , Jung, Heejung, Bahreini, Roya. Complex Refractive Index, Single Scattering Albedo, and Mass Absorption Coefficient of Secondary Organic Aerosols Generated from Oxidation of Biogenic and Anthropogenic Precursors. *Aerosol Science and Technology*, doi:10.1080/02786826.2019.1571680 (2019).

32 Lin, Y.-H. *et al.* Light-Absorbing Oligomer Formation in Secondary Organic Aerosol from Reactive Uptake of Isoprene Epoxydiols. *Environ. Sci. Technol.* **48**, 12012-12021, doi:10.1021/es503142b (2014).

33 Chen, Y. & Bond, T. Light Absorption by Organic Carbon from Wood Combustion. *Atmos. Chem. Phys.* **10**, 1773-1787 (2010).

34 Nakao, S. *et al.* Density and Elemental Ratios of Secondary Organic Aerosol: Application of a Density Prediction Method. *Atmos. Environ.* **68**, 273-277, doi:https://doi.org/10.1016/j.atmosenv.2012.11.006 (2013).

35 Gomez Alvarez, E., Borras, E., Viidanoja, J. & Hjorth, J. Unsaturated Dicarbonyl Products from the OH-initiated Photo-oxidation of Furan, 2-Methylfuran and 3-Methylfuran. *Atmos. Environ.* **43**, 1603-1612, doi:10.1016/j.atmosenv.2008.12.019 (2009).

36 Jiang, X. *et al.* Secondary Organic Aerosol Formation from Photooxidation of Furan: Effects of NOx Level and Humidity. *Atmos. Chem. Phys. Discuss.* **2018**, 1-27, doi:10.5194/acp-2018-477 (2018).

37 Moosmuller, H. & Sorensen, C. M. Small and Large Particle Limits of Single Scattering Albedo for Homogeneous, Spherical Particles. *J. Quant. Spectrosc. Ra.* **204**, 250-255, doi:10.1016/j.jqsrt.2017.09.029 (2018).

38 Sumlin, B. J. *et al.* UV-Vis-IR Spectral Complex Refractive Indices and Optical Properties of Brown Carbon Aerosol from Biomass Burning. *J. Quant. Spectrosc. Ra.* **206**, 392-398, doi:10.1016/j.jqsrt.2017.12.009 (2018).

39 Hems, R. F. & Abbatt, J. P. D. Aqueous Phase Photo-oxidation of Brown Carbon Nitrophenols: Reaction Kinetics, Mechanism, and Evolution of Light Absorption. *Acs Earth and Space Chemistry* **2**, 225-234, doi:10.1021/acsearthspacechem.7b00123 (2018).

40 Updyke, K. M., Nguyen, T. B. & Nizkorodov, S. A. Formation of Brown Carbon via Reactions of Ammonia with Secondary Organic Aerosols from Biogenic and Anthropogenic Precursors. *Atmos. Environ.* **63**, 22-31, doi:https://doi.org/10.1016/j.atmosenv.2012.09.012 (2012).

41 Liu, J. *et al.* Optical Properties and Aging of Light-absorbing Secondary Organic Aerosol. *Atmos. Chem. Phys.* **16**, 12815-12827 (2016).

42 Nguyen, T. B. *et al.* Formation of Nitrogen- and Sulfur-containing Light-Absorbing Compounds Accelerated by Evaporation of Water from Secondary Organic Aerosols. *J. Geophys. Res-Atmos.* **117**, doi:doi:10.1029/2011JD016944 (2012).

43 Baker, J. W. & Easty, D. M. Hydrolysis of Organic Nitrates. *Nature* **166**, 156, doi:10.1038/166156a0 (1950).

44 Jiang, H., Jang, M. & Yu, Z. Dithiothreitol activity by particulate oxidizers of SOA produced from photooxidation of hydrocarbons under varied NOx levels. *Atmos. Chem. Phys.* **17**, 9965-9977, doi:10.5194/acp-17-9965-2017 (2017).

Chapter 5: Refractive Index Confidence Explorer (RICE): A Tool for Propagating Uncertainties through Full Size Distribution Aerosol Refractive Index Calculations

5.0 Acknowledgement of Co-authorship

This work was completed with contributions from Alexander L. Frie and Roya Bahreini.

5.1 Introduction

The largest uncertainties in modern climate models are aerosol direct and indirect effects.[1] The direct effects occur when a suspended particle attenuates incoming solar radiation, causing heating or cooling in the atmosphere and affecting the global radiation budget, local cloud cover, weather, and surface temperatures.[2–4] The magnitude of aerosols' direct radiative effect is partially controlled by their concentration, size distribution, vertical distribution , and refractive index (*m*); because of this it is crucial to constrain uncertainties in aerosol *m* values.

Refractive indices (*m*) are a compositionally controlled measure of how a material interacts with light and are defined as the ratio of the speed of light through a vacuum to the speed of light through the material.[5] *m* values are composed of a real component *(n*), describing scattering, and an imaginary component (*k*), describing absorption (Eq. 5.1).

$$m = n + ik \tag{5.1}$$

The absorbing component describes the transformation of radiation to heat energy. For atmospheric applications, *n* is considered to control cooling and *k* warming. Although *m* values of many aerosol components are well constrained, *m* values for organic aerosols (OA) are uncertain due to both the complexity of OA composition and the uncertainties associated with in-situ *m* measurement techniques.[6]

Significant interest in OA optical properties developed after the discovery of brown carbon (BrC), organic aerosols that have a significant absorbing capability in the UV-visible range.[7] Originally OA was thought to be purely scattering and only elemental carbon or black carbon (BC) species were thought to appreciably absorb in visible-near UV.[7] Observations in the early 2000's revealed that ambient OA did have a measurable absorption component.[8–11] Following these observations, several studies have focused on measurements of the complex refractive indices of both primary organic aerosol (POA) and secondary organic aerosol (SOA) BrC. Summaries of these observations can be readily found in Flores et al. (2014), Laskin et al. (2015), and Moise et al. (2015) and references therein.[6,12,13] In these studies, *n* values of OA over solar wavelengths of ~300-800 nm typically span a range from 1.3 to 1.6 and *k* values from 0-0.1.

Most in-situ *m* calculations rely on variations of the optical closure method (OCM), to derive aerosol refractive index values. By assuming particle sphericitiy these methods can apply Mie theory to describe the optical behavior of particles and calculate *m* of aerosol particles.[14] Mie theory mathematically represents the expected scattering and absorption of spherical particles when particle diameters are on the same scale as the radiation wavelength, as they are in aerosols. Simply stated, OCMs iteratively predict the expected scattering and absorption of a population of aerosols with an observed size distribution and assumed *m* values using Mie theory. These values are then compared to the observed scattering and absorption coefficients ($ß_{scat}$, $ß_{abs}$); the *m* value which best predicts the observed coefficients is then selected as the *m* of the aerosol population, or the "retrieved" *m*. The accuracy and precision of an OCM is strongly dependent on the accuracy and

precision of the optical and size distribution measurements but also depends on *n*, *k*, and the properties of the size distribution.

One common OCM method, hereafter referred to as the size selected OCM (SSOCM), relies on sampling several mono-disperse aerosol distributions. The effects of error and uncertainty on *m* retrieval via this method, examined in detail in Zarzana et al., reveals the importance of using a minimum number of diameters for SSOCM.[15] Sources of error via this method have also been thoroughly explored in Mason et al. and Miles et al.[16,17]; common sources of error include the influence of doubly charged particles and over/under counting of particle concentrations. The applicability of the SSOCM is limited under field conditions, when particle composition and *m* can change rapidly, leading to an inability to sample the multiple paired size and optical measurements under similar conditions.[18] Due to this, other quicker methods of calculating *m* in aerosols have been developed.

One relatively quicker method is the full distribution optical closure method (FDOCM). Rather than size selecting, FDOCM method uses the complete aerosol size distribution data and the corresponding optical properties to retrieve *m*. FDOCM has been recently applied to field and chamber data.[19–26] Although the same sources of error and uncertainty exist for this method, no robust analysis of the effects of all the relevant uncertainties has been performed. In this work, a tool to estimate the uncertainty of *m* values retrieved from the FDOCM method is presented and the ability of the FDOCM method to retrieve precise refractive index values under typical uncertainty conditions is evaluated over a wide range of *m* values and representative size distributions.

5.2 Methods

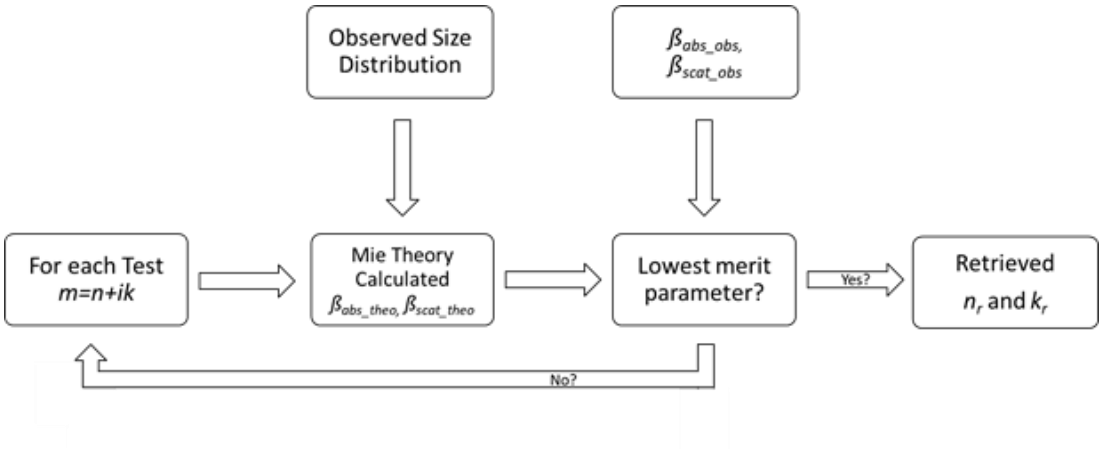

Figure 5.1. General schematic of *n* and *k* retrieval

5.2.1 Basic Refractive Index Calculation

Refractive index fitting discussed hereafter is based upon Mie Theory scattering of a well-mixed sphere, as described in detail in Bohren and Huffman (1998).[14] For a given size distribution the optical coefficients ($ß_{scat}, ß_{abs}$) are calculated (Eq. 5.2):

$$ß_{scat} = \sum_{i=1}^{i=end} Q_{scat}\left(d_{p(i)}, \lambda, n, k\right) * N_{(i)} * \frac{\left(\pi * {d_{p(i)}}^2\right)}{4} \quad (5.2a)$$

$$ß_{abs} = \sum_{i=1}^{i=end} Q_{abs}\left(d_{p(i)}, \lambda, n, k\right) * N_{(i)} * \frac{\left(\pi * {d_{p(i)}}^2\right)}{4} \quad (5.2b)$$

where Q_{scat} and Q_{abs} are the scattering and absorption efficiencies as calculated using Mie theory; these relate the amount of radiation attenuated by each process to the particle diameter (d_p) for a given wavelength (λ), *n*, and *k*. N_i is the number of particles within each size bin; $d_{p(i)}$is the midpoint particle diameter of a size bin, which is varied from $d_{p(i)}$, the smallest bin diameter, to $d_{p(end)}$, the largest bin diameter.

To calculate the unknown *m* of an aerosol population (Figure 5.1), theoretical optical coefficients ($ß_{scat\_Theo}$,$ß_{abs\_Theo}$) are compared to the observed values ($ß_{scat\_obs}$, $ß_{abs\_obs}$) through a merit parameter over a range of *m* inputs. The *m* value that minimizes the merit parameter is chosen as the retrieved *m* (m_r). Multiple merit parameters have been used for *m* retrievals. Examples include the summed difference (Δ) and chi squared (χ^2): [19–24,2625,27]

$$\Delta = \left(ß_{scat\_obs} - ß_{scat\_theo} \right) + \left(ß_{abs\_obs} - ß_{abs\_theo} \right) \quad (5.3)$$

$$\chi^2 = \left(\frac{ß_{scat\_obs} - ß_{scat\_theo}}{\sigma_{scat} * ß_{scat\_obs}} \right)^2 + \left(\frac{ß_{abs\_obs} - ß_{abs\_theo}}{\sigma_{abs} * ß_{abs\_obs}} \right)^2 \quad (5.4)$$

Where σ_{scat} and σ_{abs} are the relative uncertainties in the $ß_{scat}$ and $ß_{abs}$ measurements. In the following analysis χ^2 is used as the merit parameter.

5.2.2 Refractive Index Confidence Explorer (RICE) Description

Refractive Index Confidence Explorer **(**RICE) is a tool which estimates the uncertainties within the FDOCM. The goal of RICE is to constrain the possible *m* values ($m_{true}=n_{true}+ik_{true}$) which could have yielded the retrieved *m* ($m_{r=}n_r + ik_r$) under the given uncertainty conditions. RICE applies a probabilistic and iterative approach where FDOCM inputs are varied randomly within their analytical uncertainty ranges. The output is an estimate of a statistically relevant range (e.g. 95 % confidence Interval) of m_{true} values which could have produced the given m_r.

RICE calculates the m_{true} probability distribution through the following steps. The operator supplies an m_r, a size distribution, and the relative measurement uncertainties of $ß_{scat}$, $ß_{abs}$, d_p, and *N* (i.e., σ_{scat}, σ_{abs}, σ_{dp}, σ_N, respectively). RICE then determines the

correct n_{true} and k_{true} sampling space using a relativity quick spin-up setting. With a smaller number of iterations (I_{spin}) and a coarser $i^0 \times j^0$ "matrix" of m_{true} values (M_{spin}), where i^o represent the number of n_{true} and j^0 the number of k_{true} values tested in this space (Section 5.2.3) Once the sampling space meets RICE's criteria for fit parameters (Section 5.2.4), RICE applies a finer resolution $i \times j$ matrix size (M_{final}), and a greater number of iterations (I_{final}). Finally, RICE outputs the confidence interval of a certain width around m_r corresponding to a pre-defined confidence interval (e.g., 95%).

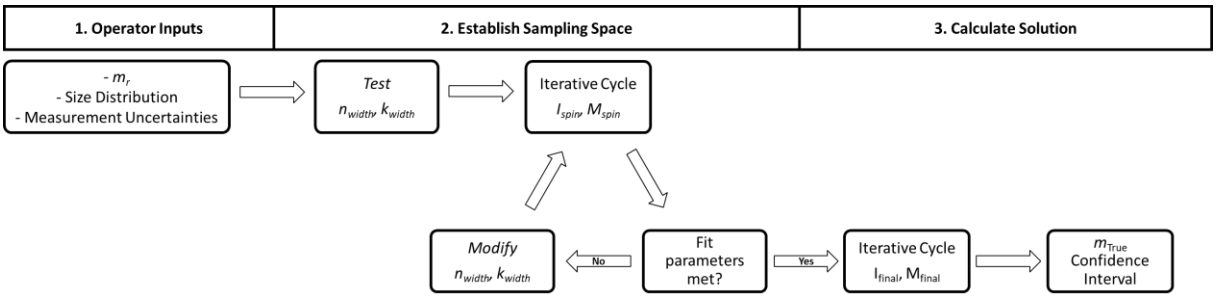

Figure 5.2. General schematic of RICE for a single m_r value.

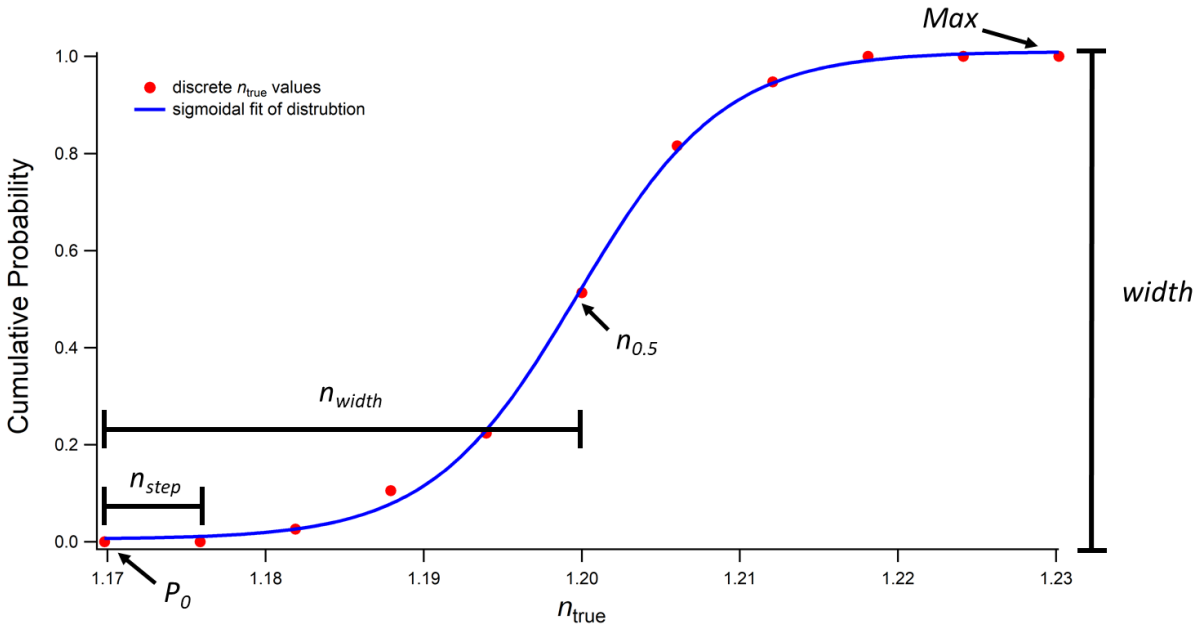

Figure 5.3. Example cumulative probability distribution and the associated sigmoidal fit parameters. n_{width}, n_{step}, $n_{0.5}$, *Max*, P_0, and *Height* are annotated.

5.2.3 Iterative Cycle

RICE performs the following steps for each point within the input m_r (Figure 5.2). An initial sampling space around m_r (n_{width}, k_{width}) is established. This is the space RICE first samples m_{true} values which could possibly provide m_r.

$$n_{width} = (n_r - 1) * \left(\sigma_{scat} + \sigma_{dp} + \sigma_N \right)/2 \quad (5.5a)$$

$$k_{width} = (k_r) * (\sigma_{abs} + \sigma_{dp} + \sigma_N)/2 \quad (5.5b)$$

After establishing an initial n_{width} and k_{width}, a series of discrete n_{true} and k_{true} values are chosen within the $n_r \pm n_{width}$ and $k_r \pm k_{width}$ space. These values are chosen at equal intervals of n_{step} and k_{step} around m_r (Figure 5.3 highlights examples for n).

$$n_{step} = \frac{n_{width}}{\left(trunc\left(\frac{\sqrt{i\,x\,j}}{2}\right)\right)} \quad (5.6a)$$

$$k_{step} = \frac{k_{width}}{\left(trunc\left(\frac{\sqrt{i\,x\,j}}{2}\right)\right)} \quad (5.6b)$$

Where *trunc*() is a function which truncates a value to an integer. For each iteration, every n_{true} and k_{true} combination (m_{true}) is tested for the ability to produce m_{r} under the given uncertainty.

For each iteration, RICE performs the following calculations (Figure 5.4). First, each d_p and N value associated with the size distribution are perturbed using the Wavemetrics Igor Pro's Gaussian noise (gnoise) function and the associated uncertainties (σ_{dp} and σ_N respectively). This creates perturbed values for each iteration (d_{p_I}, N_I). For d_{p_I}, all size bins are perturbed by the same value with the assumption that individual bin size uncertainties are uniform. For N_I the perturbation is unique to each bin. This creates a possible "true" size distribution for each iteration. It should be noted that to decrease analysis time, only bins which contribute to >=1% of $ß_{abs}$ or $ß_{scat}$ at the median m_{true} or the most extreme tested m_{true} values are used by RICE. Values of d_{p_I} and N_I are then used to calculate optical coefficients for each discrete m_{true} value using Mie theory (Section 5.2.1). The calculated optical coefficients are then adjusted using the gnoise function to simulate the observation of the "true" optical properties observed under the expected analytical uncertainties ($ß'_{scat\_I}$ and $ß'_{abs\_I}$). $ß'_{scat\_I}$ and $ß'_{abs\_I}$ are considered as the "observed" optical coefficients for a closure calculation as detailed in section 5.2.1. In this closure investigation, the Mie calculation is performed using the original size distribution

parameters (d_p and N) and all the m_{true} values as possible solutions. Note that in RICE, values of m retrieved using the perturbed inputs are defined as m_r' to avoid confusion with m_{r}. At the end of each iteration, each m_{true} value is associated with a resulting m_r'. This process is repeated I number of times.

To help ensure calculations are reasonable and that both scattering and absorption coefficients are weighted appropriately, RICE only considers m_r' values as solutions if $ß_{scat\_theo}$ and $ß_{abs\_theo}$ are within a certain threshold of $ß'_{scat\_I}$ and $ß'_{abs\_I}$. For $ß'_{scat\_I}$, this threshold is set at $2*\sigma_{scat}*ß'_{scat\_I}$ or the maximum relative $ß_{scat\_theo}$ difference between consecutive n_{true} values (k held constant), whichever is smaller. For $ß'_{abs\_I}$, this threshold is set at $2*\sigma_{abs}*ß'_{abs\_I}$ or the maximum relative $ß_{abs\_theo}$ difference between consecuative k_{true} (n held constant), values, whichever is smaller.

After I iterations, a matrix of m_{true} vs. m_r' with I number of values associated with each discrete m_{true} is created. This matrix describes the probability of each tested m_{true} producing any tested m_r' under the given uncertainty conditions. From this matrix, the probability distribution of m_r having originated from any possible m_{true} can be extracted, assuming the sampling space accounts for all the probable m_{true} values. Next, RICE interpolates the probability associated with untested m_{true} values which lie between the tested values as described in Section 5.2.5.

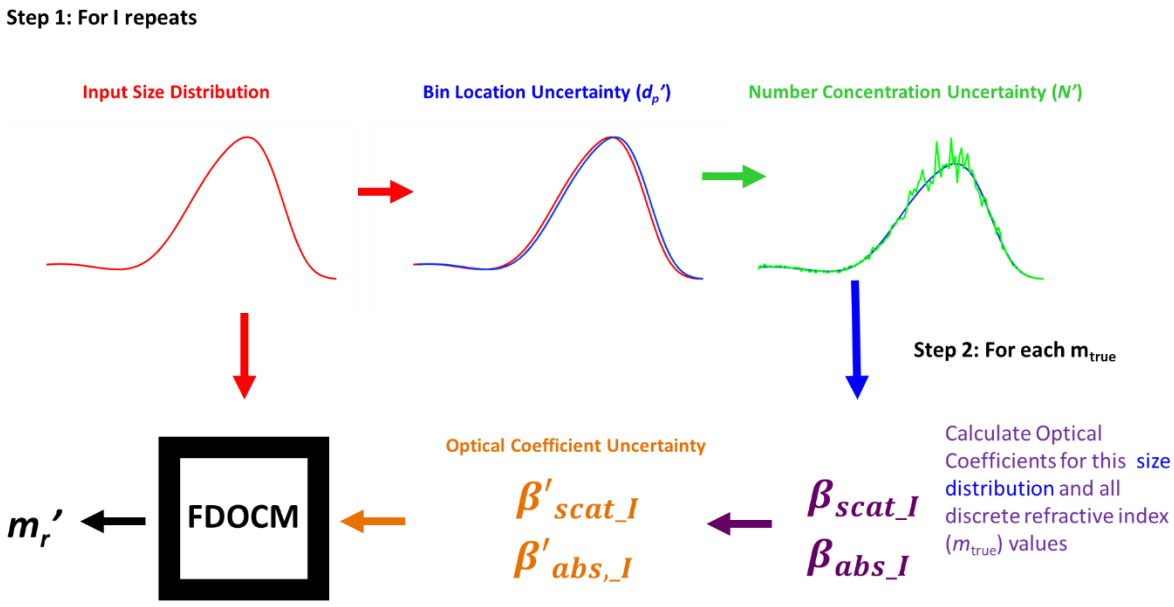

Figure 5.4 General schematic of the iterative cycle for determining m_r. Step 1 is repeated I times and step 2 is repeated for each m_{true} tested.

5.2.4 Fitting

To analyze the appropriateness of the *m* sampling space and ensure all possible m_{true} values that could give m_r are within the sampling space, two sigmoidal fit parameters of the cumulative probably distribution of n_{true} and k_{true} are used (Figure 5.3, Eq. 5.7). When fit parameters are satisfied, RICE changes from I_{spin} and M_{spin} to I_{final} and M_{final}. When calculating these distributions n_{true} and k_{true} are treated independently.

$$CP_{m_r}(n_{true}) = P_0 + \frac{Max}{\left(1+exp^{\left(\frac{n_{0.5}-n_{true}}{rate}\right)}\right)} \quad (5.7a)$$

$$CP_{m_r}(k_{true}) = P_0 + \frac{Max}{\left(1+exp^{\left(\frac{k_{0.5}-k_{true}}{rate}\right)}\right)} \quad (5.7b)$$

Where $CP_{m_r}(n_{true})$ is the cumulative probability that a given n_{true} and any values below it results in n_r; $n_{0.5}$ is the location of the 50th percentile of the probability; P_0 is the lower asymptote of the cumulative probability distribution; *Max* is the upper asymptote of the cumulative probability distribution. Analogous definitions apply to parameters in Eqn. 5.7b for *k*.

To ensure that RICE is sampling the most useful sampling space, additional parameters ("*height*" and "*idle*") are considered. After every spin-up cycle, RICE checks these parameters. If conditions for these parameters are satisfied, RICE starts the final cycle; otherwise, itmodifies n_{width} and/or k_{width} and runs again using the spin-up parameters. The fit parameters values of *height* (Eq. 5.8) and *idle* are calculated for both *n* and *k*:

$$Height = Max - P_0 \quad (5.8)$$

Height is used to ensure that all probable m_{true} values lie within the sampling space. If *height* is greater than 1.05, RICE expands n_{width} or k_{width} to n_{width*}*height* or k_{width*}*height,* respectively. The maximum expansion allowed by RICE is 1.25.

If *height* is less than 1.05, RICE checks the second quantity, *idle. Idle* is defined as the fraction of n_{true} or k_{true} values which never produced m_r. If *idle* is greater than 0.65 but less than 0.75, n_{width} or k_{width} is reduced by 20%; if *idle* is greater than 0.75 n_{width} or k_{width} is reduced by 10%. If these conditions are met, a final Iterative cycle is performed using I_{final} and M_{final} and a solution is calculated. For experiments within this work I_{spin}=10, M_{spin}=64, I_{final}=75, and M_{final}=100 are tested.

5.2.5 Output

After establishing the sampling space with I_{spin} and M_{spin} and performing the final iterative cycle using M_{final} and I_{final}, RICE creates an empirical distribution function and fits this distribution with a sigmoid as described in section 5.2.4. Unlike during the spin-up, for the output calculation *Max* is fixed to 1 and P_0 at 0, because negative and >1 probabilities are impossible. This forces the assumption that the full range of probability space is sampled. If any n_{true} or k_{true} values are at their lower limits (1 or 0 respectively), then RICE fixes P_0 to the probability observed at the nearest n_{true} or k_{true} above the lower limit. From this fit, a confidence interval, based on user-defined confidence levels, can be calculated. In the following analysis the ±2σ space (68% confidence interval or 2σ width) is reported. To isolate effects not driven by the magnitude of *n* and *k*, RICE also outputs 2σ widths normalized to the magnitude of *n* and *k* values ($2\sigma_{norm\_n}$, $2\sigma_{norm\_k}$, respectively). It should be noted that the uncertainty in *n* was normalized to the difference in aerosol *n* and that of air (n=1) while the uncertainty in *k* was normalized to *k* itself.

$$2\sigma_{norm\_n} = \left(\frac{2\sigma_n}{n-1}\right) \tag{5.9a}$$

$$2\sigma_{norm\_k} = \left(\frac{2\sigma_k}{k}\right) \tag{5.9b}$$

5.2.6 Flags

Although RICE is designed to isolate a single, reproduceable, estimate of the uncertainty in an FDOCM *m* retrieval, there are situations were RICE solutions may be misleading. In order to identify these cases, a series of flags are built into RICE, although for the current analysis, the flags are not used to filter results.

The first flag (*space-n* or *-k)* attempts to identify situations were RICE has identified an inappropriate sampling space which did not include all possible n_{true}'s and/or k_{true}'s. *Space-* is based on the *height* of the sigmoidal fit to the final result; when calculating *space-*, *Max* and P_0 are not fixed as they are in the confidence interval calculation. The *space-* flag is determined as follows:

height < 1.05:	*space-*=0
1.05 < *height* < 1.125:	*space-*=1
1.125 < *height* < 1.2:	*space-*=2
height > 1.2:	*space-*=3

Solutions with a *space-* flag of 2 or 3 should be interpreted cautiously. If possible, RICE should run the conditions again, but if RICE keeps returning a 2 or 3 for *space-* the conditions may not have a stable solution.

The second flag, *count*, attempts to identify solutions where a low number of points contribute to the final probability distributions. In the ideal situation (*Count*=0), the number of m_{true} instances which give m_r should be ~I_{final} if solutions are distributed equally among the input m_r' values. Count is set to 1 if the number of values contributing to the probability distribution is less than 0.5*I_{final}. In this case, it is possible that RICE has too large of a n_{width} or k_{width}, or that the probability distribution does not follow the assumptions that are needed for RICE to provide a robust solution.

5.3 Application

5.3.1 Test Cases

To explore the effects of RI, wavelength, and size distribution on uncertainty, RICE was applied, in triplicate, to 7 size distributions at 16 *m* values and 2 wavelengths. Size distributions were chosen to represent a variety of aerosol conditions. These distributions are labeled Rainforest High (RFH), Rain Forest Low (RFL), Urban High (UH), Urban Low (UL), Literature Simulation (LS), Chamber Simple (CS), and Chamber Complex (CC) (Figure 5.5). RFH and RFL respectively correspond to the dry and wet diurnal averages for aerosols within the Amazon.[28] UH and UL correspond to size distributions reported near Helsinki, Finland under high pollution and low pollution conditions.[29] LS corresponds to the simulated size distribution used to test a new broadband RI retrieval method.[19] CS and CC are based on chamber experiments performed at UC Riverside.[25]

Geometric mean, geometric standard deviation, and number concentration (N) for each distribution are found in Table 5.1. These values were used to generate lognormal aerosol size distributions.

Distribution Characteristics	Size Distributions						
	RFH	RFL	UH	UL	CC	CS	LS
Geo. Mean	190	128	104	191	233	253	80
Geo. SD 1	1.53	1.66	1.9	1.53	1.04	1.16	1.33
Number Conc. 1	5214	785	2189	457	47500	5601	10000
Geo. Mean	92	61	33.8	55	148		
Geo. SD 2	1.63	1.39	1.9	1.53	1.04		
Number Conc. 2	5213	406	7642	1705	8171		
Geo Mean	12	12	9.7	17.5			
Geo. SD 3	1.82	1.82	1.9	1.65			
Number Conc. 3	1090	849	9750	3581			

Table 5.1 Geometric Mean, Geometric Standard Deviations, and Number concentrations of each sample size distribution.

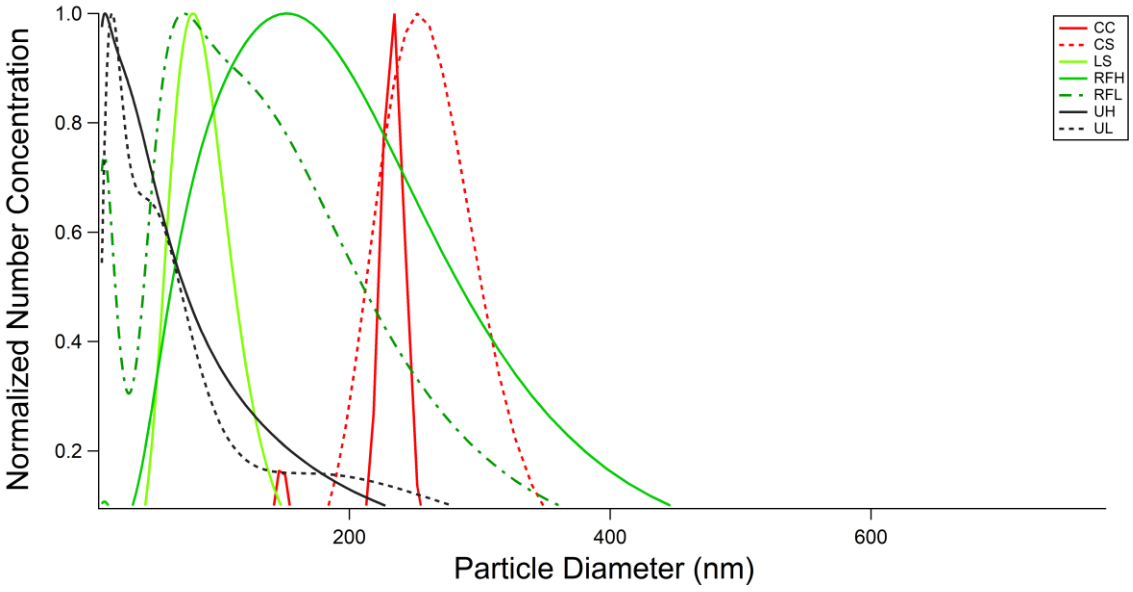

Figure 5.5 Number distributions (dN/dLog(d)) of the 7 aerosol populations tested, normalized to the highest dN/dLog(d) value observed for each distribution.

Uncertainties conditions were based on the reported uncertainties of optical, size, and number concentration measurements found within the literature. Two uncertainty levels are used in this analysis: High Uncertainty (HU) (N ± 10%, d ± 3%, ß$_{abs}$ ± 5%, ß$_{scat}$ ± 5%) and Medium Uncertainty (MU) at 50% of HU levels (i.e., N ± 5%, d ± 1.5%, ß$_{abs}$ ± 2.5%, ß$_{scat}$ ± 2.5%). HU uncertainty levels are the same as those used by Bluvshtein et al..[19]

Additionally, two different wavelengths, 632nm and 375nm, were tested. These wavelengths were tested because they are common measurement wavelengths for the upper visible (632) and UV (375 nm) regions of the solar spectrum and often used for optical measurements.[25,26,30–34] Thus, these wavelengths lie within wavelength ranges of interest for refractive index calculations. The inclusion of a UV wavelength is additionally useful, as absorption of BrC, which is a subject of many *m* measurement studies, is significantly enhanced in the UV and near-UV range.[6,13]

5.3.2 Metrics for Examining *m* Uncertainty

To help explain sources of uncertainty in the observed RICE results, 4 sensitivity metrics were calculated. These metrics describe the sensitivity of *k* or *n* retrievals and predicted ß$_{abs}$ and ß$_{scat}$ to changes, and thus uncertainty, within the input parameters.

These values are defined as the relative sensitivity of *n* to relative changes in ß$_{scat}$ ($\left|\frac{\mathrm{d}(\%n)}{\mathrm{d}(\%ß_{\mathrm{scat}})}\right|$, *n* sensitivity), the relative sensitivity of *k* to relative changes in ß$_{abs}$ ($\left|\frac{\mathrm{d}(\%k)}{\mathrm{d}(\%ß_{\mathrm{abs}})}\right|$, *k* sensitivity), and relative sensitivity of ß$_{scat}$ and ß$_{abs}$ to the relative changes in bin diameter ($\left|\frac{d(\%ß_{scat\ or\ abs})}{d(\%d_p)}\right|$, ß$_{scat}$ or ß$_{abs}$ sensitivity). These quantities are calculated by applying Mie theory and are informative as they help explain and visualize sources of uncertainty in *n*

and *k* under different conditions. For example, when *n* or *k* sensitivity is high, a small change in $ß_{scat}$ or $ß_{abs}$ will yield a relatively large change in *n* or *k*, respectively. Similarly, when $ß_{scat}$ or $ß_{abs}$ sensitivity is high, $ß_{scat}$ or $ß_{abs}$ is more sensitive to uncertainty in the bin diameter, which means size distribution uncertainty propagates more strongly into *n* or *k* retrievals, respectively.

5.4 Results

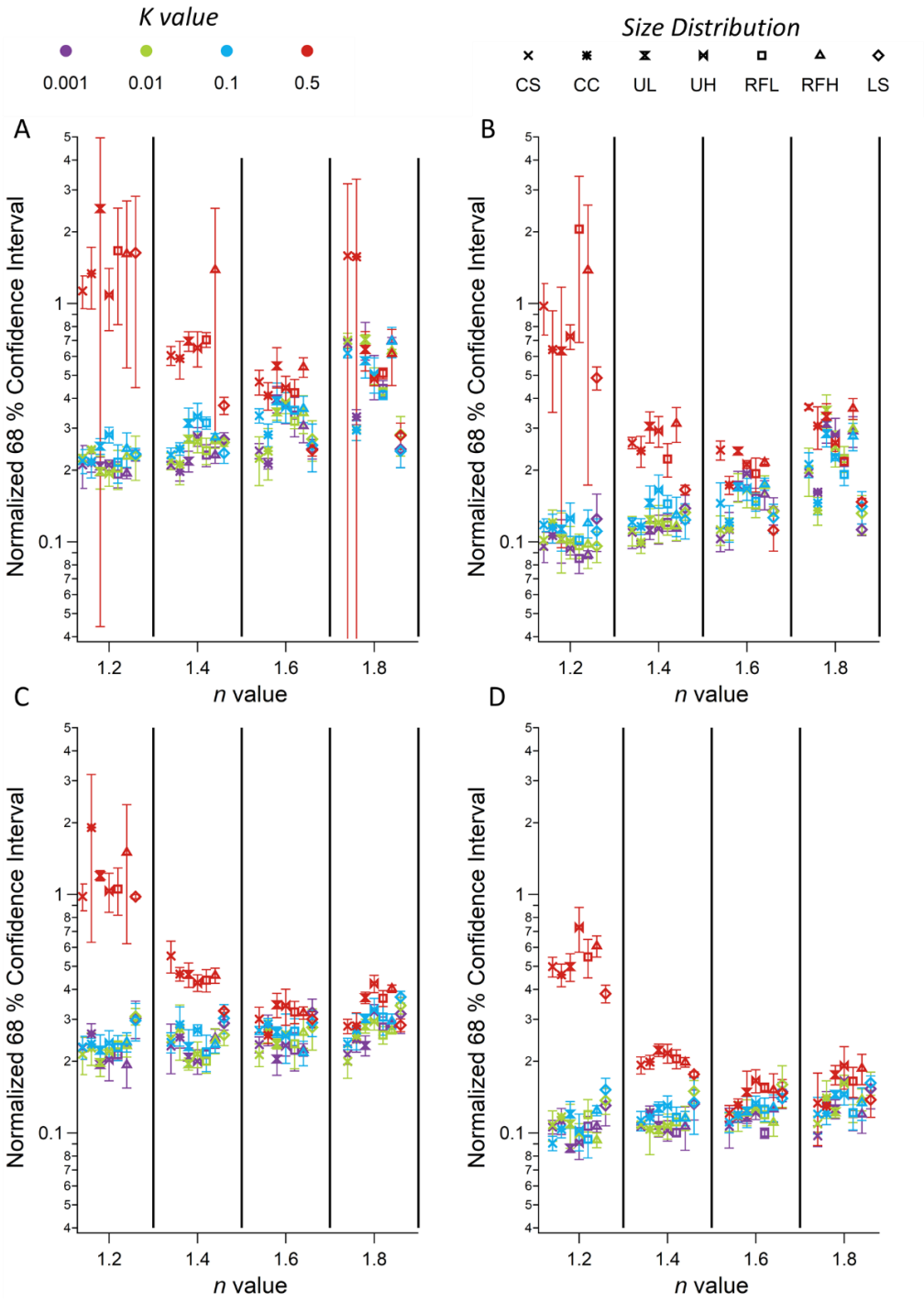

Figure 5.6. Average normalized uncertainty in *n* of triplicate runs from A) HU at 375 nm B) MU at 375nm C) HU at 632nm D) MU at 632nm for all 7 size distributions. Error bars represent 1 standard deviation of the runs. Symbols are colored by *k* value.

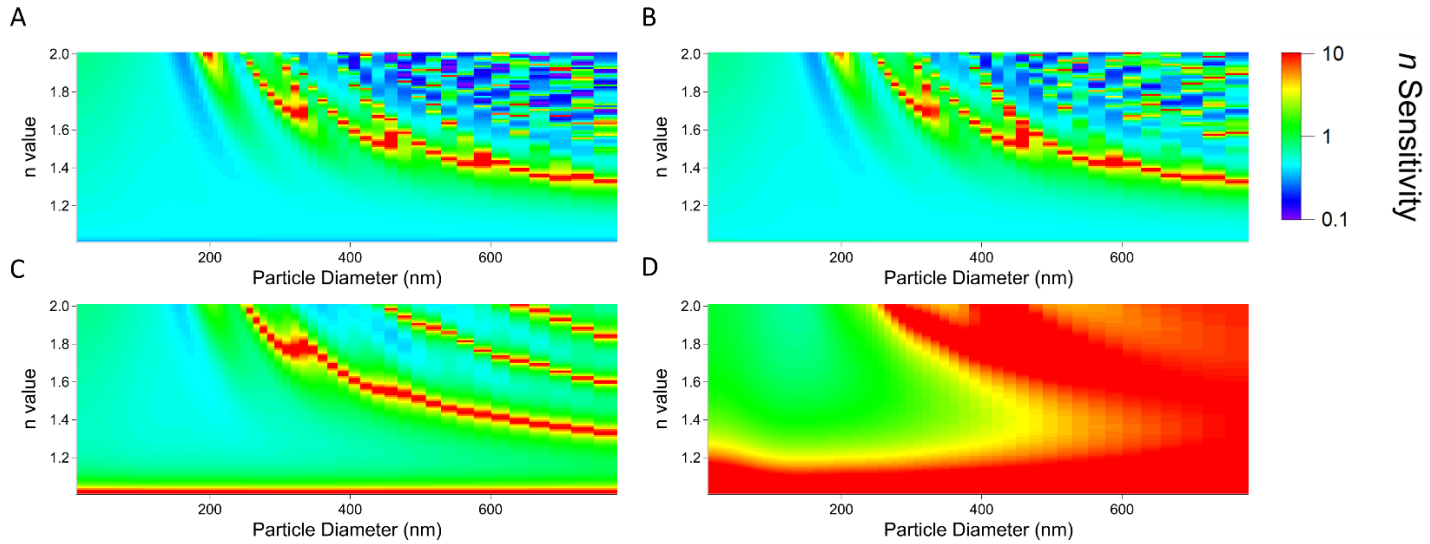

Figure 5.7 *n* sensitivity image plots when A) *k*=0.001, B) *k*=0.01, C) *k*=0.1, D) *k*=0.5 at 375 nm.

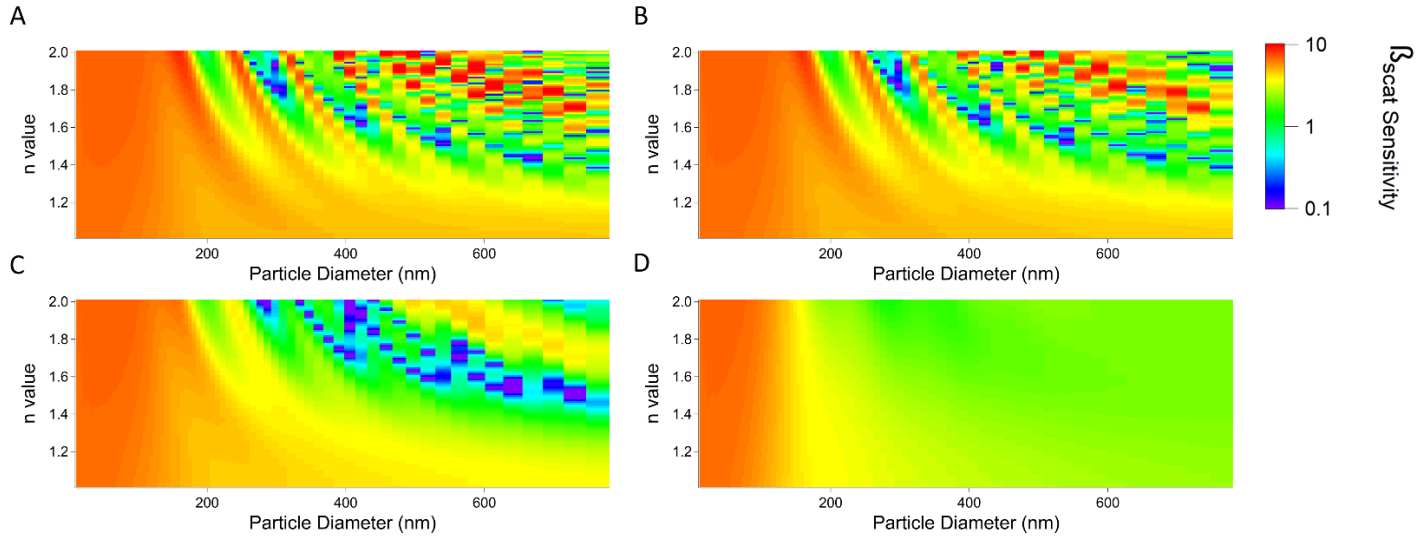

Figure 5.8. $ß_{scat}$ sensitivity image plots when A) *k*=0.001, B) *k*=0.01, C) *k*=0.1, D) *k*=0.5 at 375nm.

5.4.1 *n* Uncertainty

The following discussions are focused on the 375nm tests; for the 632 nm cases the same analyses can be performed but the sensitivity image plots would need to be adjusted to the appropriate analysis wavelength (Figures 5.7 and 5.8) For the size distributions tested, the minimum relative *n* uncertainties, i.e., minimum $2\sigma_{norm\_n}$, were independent of the wavelength and ~20% for HU cases (Figure 5.6 A,C) and ~ 10% for MU cases (Figure 5.6 B, D). Increases in $2\sigma_{norm\_n}$ above these minimums can generally be explained by features in *n* and $ß_{scat}$ sensitivity image plots (Figures 5.7 and 5.8).

RICE results reveal a strong dependence of $2\sigma_{norm\_n}$ on *k.* This effect is particularly strong for *k*=0.5 and low *n* values (1.2 or 1.4) and is explained well by changes in *n* sensitivity. Of the four *k* values examined, *n* sensitivity was highest, over approximately the whole domain, in the *k*=0.5 case. This increase in *n* sensitivity with *k* is observed over most of the *n* and d_p range and was particularly strong at low *n* values. The *k* effect is weaker, although still present, at high *n* values. Overall, these results reveal that uncertainties in retrieved *n* values (at 375 nm) are higher for the more absorbing aerosol types, particularly at low *n* values. The increase in $2\sigma_{norm\_n}$ with *k* observed by RICE is well explained by the higher *n* sensitivities observed at high *k* values.

Another trend in $2\sigma_{norm\_n}$ observed by RICE is an increase in $2\sigma_{norm\_n}$ as *n* increases. This trend was observed in all cases except the *k*=0.5 case and is explained well by a general increase in *n* sensitivity with *n* at low *k* and d_p values (k=0.001, 0.01; d_p < 200nm) (Figure 5.7 A, B) and an increase in $ß_{scat}$ sensitivity with *n* (Figure 5.8) when d_p

is low (d_p < 200nm). Absence of this trend in the k=0.5 case is well explained by the observed dramatic increase in n sensitivity and the relatively n- independent $ß_{scat}$ sensitivity in this case. It should be noted, that as diameter and k increase, trends in sensitivities become more localized; however, as a general rule, n uncertainty increases as n increases at lower diameters and k values.

Overall, the general n uncertainty trends observed by RICE can be explained as follows: at low n values, n uncertainty increases as k increases (Figure 5.7). If absorption and particle diameter are low, n uncertainty can be expected to increase with n. At higher d_p values, n uncertainty may be controlled by localized features of the n or $ß_{scat}$ sensitivities, not general trends. This variability in uncertainty trends over the size, n, and k evidences the need for RICE to assist in estimating m uncertainties on a case by case basis.

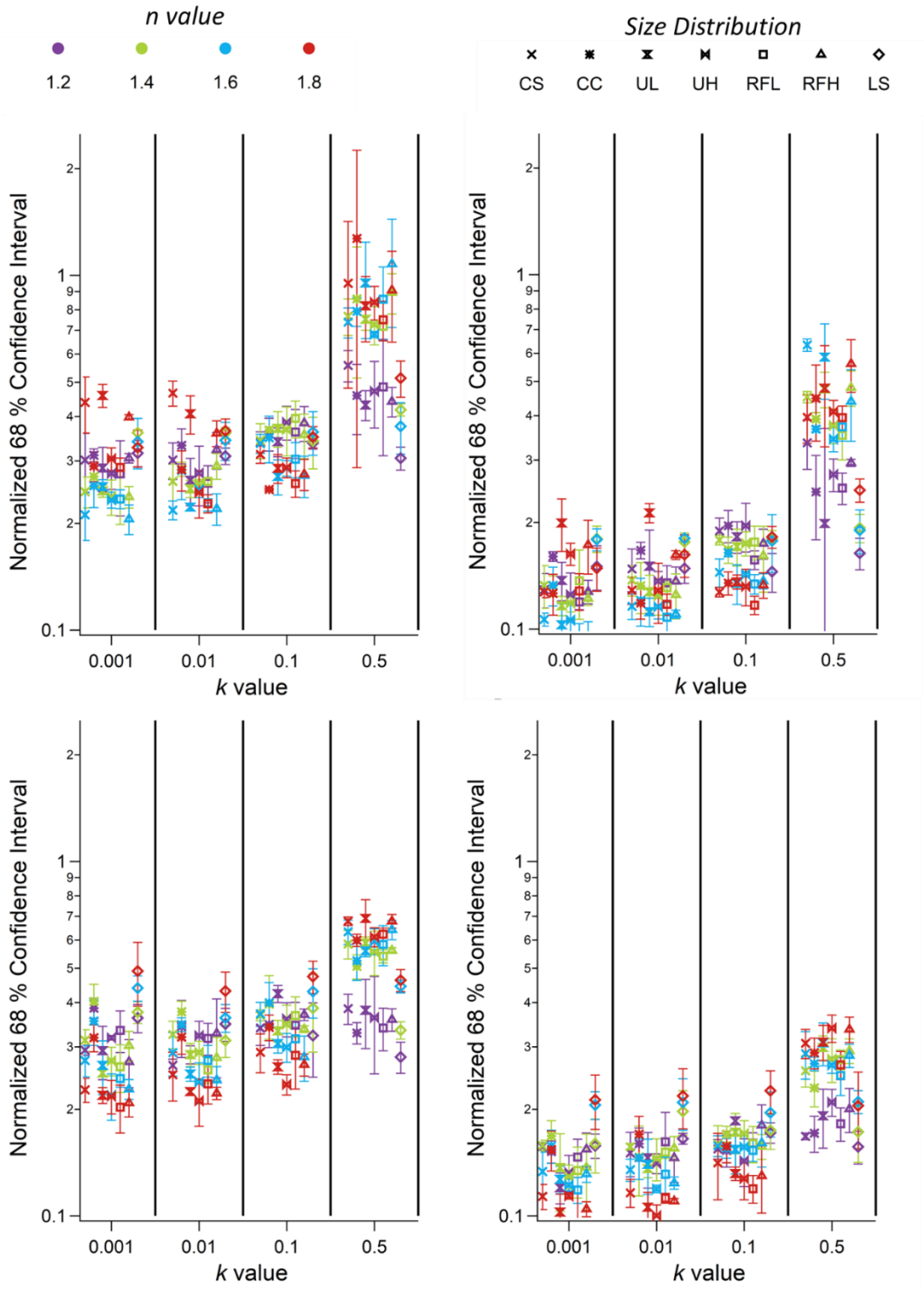

Figure 5.9. Average normalized uncertainty in *k* of triplicate runs from A) HU at 375 nm B) MU at 375nm C) HU at 632nm D) MU at 632nm for all 7 size distributions. Brackets represent 1 standard deviation of the runs. Symbols are colored by *n* value.

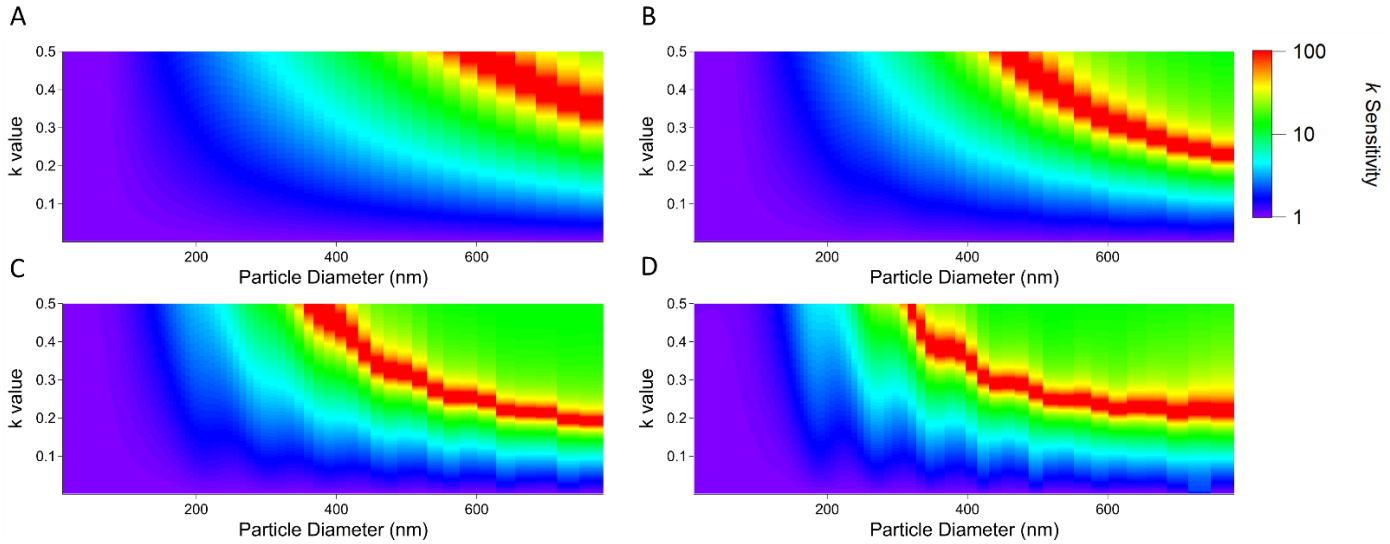

Figure 5.10 *k* sensitivity image plots when A) *n*=1.2, B) *n*=1.4, C) *n*=1.6, D) *n*=1.8

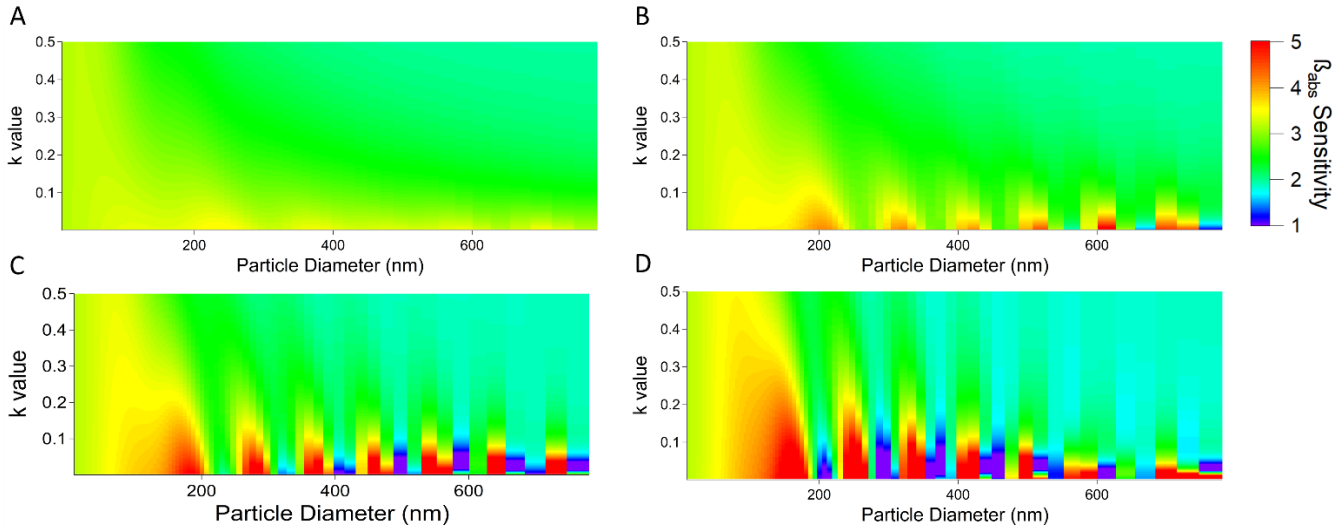

Figure 5.11 $ß_{abs}$ sensitivity image plots when A) *n*=1.2, B) *n*=1.4, C) *n*=1.6, D) *n*=1.8

5.4.2 *k* Uncertainty

For the size distributions tested, the minimum observed relative *k* uncertainties, minimum $2\sigma_{norm\_k}$, were also independent of wavelength and at ~20% for HU cases (Figure 5.9 A,C) and ~ 10% for MU cases (Figure 5.9 B, D). Increases in $2\sigma_{norm\_k}$ above these minimums can be explained by features in the *k* and $ß_{abs}$ sensitivities (Figures 5.10 and 5.11)

One feature observed in the RICE results is an increase in *k* uncertainty as *k* values increase when *k* values are high (Figure 5.9 C, D). As *k* values increase from 0.1 to 0.5, $2\sigma_{norm\_k}$ increases dramatically for all *n* values, although the increase is noticeably smaller for the $n = 1.2$ case. This trend may occur because of shifting regions of high *k* sensitivity (Figure 5.10 A-D). When *k* is small (0.001), *k* sensitivity is ~1 at all d_p values in all *n* cases. As *k* increases, regions of high *k* sensitivity move to lower d_p values, meaning at higher *k* values, a larger portion of the tested size distributions overlap with the high sensitivity regions. This leads to stronger uncertainty effects. That this trend is driven by *k* sensitivity is evidenced by the relative independence of *k* uncertainty in the LS case, because LS has no large particles ($d_p > 150$nm), thus showing the weakest response to *k* increases.

Like with *n,* the general uncertainty features observed by RICE for the tested size distributions cam be explained by examining *k* and $ß_{abs}$ sensitivities. The trends in *k* uncertainty are less stark than those of *n*. Generally, if *k* is high, the relative uncertainty of *k* increases with *k*, particularly for larger particles ($d_p >$~200 nm)

5.4.3 Individual Size Distributions

Although the uncertainty associated with most size distributions displayed the general trends discussed above, a few unique differences were observed that are worthy of discussion.

First, LS displayed the most stable *n* uncertainty characteristics, with almost no increase in $2\sigma_{norm\_n}$ with *n*. LS uncertainty displays this feature because *n* sensitivity in the region of the size distribution (~100-150 nm) is relatively low and relatively independent of *n*, as shown by the semi-vertical area of blue coloring (most obvious at ~200 nm) in all *k* cases in Figure 5.7 This means that unlike the trends for broader, larger, or smaller size distributions, for LS, *n* increases have minimal effect on $2\sigma_{norm\_n}$.

The size distribution dependence of *n* uncertainty became more prominent in the high *n* value cases (Figure 5.6). For example, in the high *n* cases (1.6, 1.8) the CC distribution had smaller $2\sigma_{norm\_n}$ than the other, non-LS, size distributions. Like LS, the CC has a peak between 100-200 nm which aligns with the region where *n* sensitivity is low and relatively *n*-independent (Figure 5.7). CC is likely more sensitive to *n* than LS because it also includes larger particles in regions where *n* sensitivity is more strongly dependent on *n.*

The two distributions that displayed the largest uncertainties as *n* increased were RFH and UL. RFH and UL are both relatively broad distributions. RFH is broad and extends to large sizes, above the *n*-independent regions discussed above. (Figure 5.7). For UL, the opposite is likely true, as most the of the size distribution is <100 nm, so the majority of the distribution lies in a region where $ß_{scat}$ sensitivity increases with *n*

(Figures 5.7 and 5.8). The contrasting features of these two distributions, further evidence the complex nature of *m* uncertainty dependencies and benefits of the analysis provided by RICE.

Concerning *k*, only one size distribution displays different results from the others. Although *k* uncertainty increases for all distributions in the *k*=0.5 case, for LS the increases are less (Figure 5.9). As discussed above (Section 5.3) this distribution has high concentrations of small particles and few larger particles. Due to this, as *k* increases, this size distribution is more likely to stay within the space of low *k* sensitivity ($k \cong 1$). This feature protects *k* retrievals from increases in relative uncertainty as *k* increases.

5.5 Conclusions

Here, we have developed and applied a tool to estimate the uncertainty in aerosol refractive index calculations. We used this tool to analyze the uncertainty of *m* retrievals, using 7 size distributions and 16 *m* values, at two radiation wavelengths. In addition, we have qualitatively validated RICE results through explaining uncertainty trends and size distribution effects through *n*, *k*, and ß sensitivities.

This analysis revealed that, for the size distributions tested, relative uncertainty in *n* can be expected to increase with *n* value and increase with *k* value if *n* and d_p are low. For *k*, at high *k* values the relative uncertainty in *k* generally increases with *k*. Despite these overall trends, the uncertainty was also dependent on the observed size distribution and should be analyzed for each individual *m* calculation.

Overall, the analysis reveals the need for, and usefulness of, a tool to estimate the uncertainty in *m* retrievals for specific measurement conditions. RICE will help constrain

uncertainties in *m* retrievals under the field and laboratory conditions. By applying RICE, users can actively account for any additional uncertainty from *n*, *k*, and size distribution effects which could change the uncertainty in FDCOM *m* retrievals.

5.6 Works Cited

1. Pachauri, R. K., Allen, M. R. , Barros, V. R. , Broome, J. , Cramer, W. , Christ, R. Church, J. A. , Clarke, L. , Dahe, Q. , Dasgupta, P. , Dubash, N. K. , Edenhofer, O. , Elgizouli, I. , Field, C. B. , Forster, P. , Friedlingstein, P. , Fuglestvedt, J. , Gomez-Echeverri, L. , Hallegatte, S. , Hegerl, G. , Howden, M. , Jiang, K. , Jimenez Cisneroz, B. , Kattsov, V. , Lee, H. , Mach, K. J. , Marotzke, J. , Mastrandrea, M. D. , Meyer, L. , Minx, J. , Mulugetta, Y. , O'Brien, K. , Oppenheimer, M. , Pereira, J. J. , Pichs-Madruga, R. , Plattner, G. K. , Pörtner, H. O. , Power, S. B. , Preston, B. , Ravindranath, N. H. , Reisinger, A. , Riahi, K. , Rusticucci, M. , Scholes, R. , Seyboth, K. , Sokona, Y. , Stavins, R. , Stocker, T. F. , Tschakert, P. , van Vuuren, D. and van Ypserle, J. P. . *Climate Change 2014: Synthesis report. Contribution of Working Groups I, II and III to the Fifth Assessment Report of the Intergovernmental Panel on Climate Change*. (IPCC, 2014).

2. Bond, T. C. *et al.* Bounding the role of black carbon in the climate system: A scientific assessment. *J. Geophys. Res. Atmos.* 118, 5380–5552 (2013).

3. Ramanathan, V. & Carmichael, G. Global and regional climate changes due to black carbon. *Nature Geosci* 1, 221–227 (2008).

4. Perrone, M. R., Tafuro, A. M. & Kinne, S. Dust layer effects on the atmospheric radiative budget and heating rate profiles. *Atmos. Environ.* 59, 344–354 (2012).
5. Hecht, E. *Optics*. (Addison-Wesley, 2002).

6. Moise, T., Flores, J. M. & Rudich, Y. Optical Properties of Secondary Organic Aerosols and Their Changes by Chemical Processes. *Chem. Rev.* 115, 4400–4439 (2015).

7. Andreae, M. O. & Gelencsér, A. Black carbon or brown carbon? The nature of light-absorbing carbonaceous aerosols. *Atmos. Chem. Phys.* 6, 3131–3148 (2006).

8. Alexander, D. T. L., Crozier, P. A. & Anderson, J. R. Brown Carbon Spheres in East Asian Outflow and Their Optical Properties. *Science* 321, 833–836 (2008).

9. Bergstrom, R. W. *et al.* Spectral absorption properties of atmospheric aerosols. *Atmos. Chem. Phys.* 7, 5937–5943 (2007).

10. Kirchstetter, T. W., Novakov, T. & Hobbs, P. V. Evidence that the spectral dependence of light absorption by aerosols is affected by organic carbon. *J. Geophys. Res.* 109, D21208 (2004).

11. Lukács, H. *et al.* Seasonal trends and possible sources of brown carbon based on 2-year aerosol measurements at six sites in Europe. *J. Geophys. Res.* 112, D23S18 (2007).

12. Flores, J. M. *et al.* Complex refractive indices in the near-ultraviolet spectral region of biogenic secondary organic aerosol aged with ammonia. *Phys. Chem. Chem. Phys.* 16, 10629–10642 (2014).

13. Laskin, A., Laskin, J. & Nizkorodov, S. A. Chemistry of Atmospheric Brown Carbon. *Chem. Rev.* 115, 4335–4382 (2015).

14. Wiley: Absorption and Scattering of Light by Small Particles - Craig F. Bohren, Donald R. Huffman. Available at: http://www.wiley.com/WileyCDA/WileyTitle/productCd-0471293407.html. (Accessed: 30th June 2017)

15. Zarzana, K. J., Cappa, C. D. & Tolbert, M. A. Sensitivity of Aerosol Refractive Index Retrievals Using Optical Spectroscopy. *Aerosol Science and Technology* 48, 1133–1144 (2014).

16. Mason, B. J. *et al.* Comparison of the Accuracy of Aerosol Refractive Index Measurements from Single Particle and Ensemble Techniques. *J. Phys. Chem. A* 116, 8547–8556 (2012).

17. Miles, R. E. H., Rudić, S., Orr-Ewing, A. J. & Reid, J. P. Sources of Error and Uncertainty in the Use of Cavity Ring Down Spectroscopy to Measure Aerosol Optical Properties. *Aerosol Science and Technology* 45, 1360–1375 (2011).

18. Radney, J. G. & Zangmeister, C. D. Comparing aerosol refractive indices retrieved from full distribution and size- and mass-selected measurements. *Journal of Quantitative Spectroscopy and Radiative Transfer* 220, 52–66 (2018).

19. Bluvshtein, N., Flores, J. M., Segev, L. & Rudich, Y. A new approach for retrieving the UV–vis optical properties of ambient aerosols. *Atmos. Meas. Tech.* 9, 3477–3490 (2016).

20. Bluvshtein, N. *et al.* Broadband optical properties of biomass-burning aerosol and identification of brown carbon chromophores. *J. Geophys. Res. Atmos.* 122, 2016JD026230 (2017).

21. Denjean, C. *et al.* A new experimental approach to study the hygroscopic and optical properties of aerosols: application to ammonium sulfate particles. *Atmos. Meas. Tech.* 7, 183–197 (2014).

22. Denjean, C. *et al.* Aging of secondary organic aerosol generated from the ozonolysis of alpha-pinene: effects of ozone, light and temperature. *Atmos. Chem. Phys.* 15, 883–897 (2015).

23. Denjean, C. *et al.* Relating hygroscopicity and optical properties to chemical composition and structure of secondary organic aerosol particles generated from the ozonolysis of α-pinene. *Atmos. Chem. Phys.* 15, 3339–3358 (2015).

24. De Haan, D. O. *et al.* Brown Carbon Production in Ammonium- or Amine-Containing Aerosol Particles by Reactive Uptake of Methylglyoxal and Photolytic Cloud Cycling. *Environ. Sci. Technol.* 51, 7458–7466 (2017).

25. Dingle, J. H. *et al.* Complex refractive index, single scattering albedo, and mass absorption coefficient of secondary organic aerosols generated from oxidation of biogenic and anthropogenic precursors. *Aerosol Science and Technology* 53, 449–463 (2019).

26. Jiang, H. *et al.* Brown Carbon Formation from Nighttime Chemistry of Unsaturated Heterocyclic Volatile Organic Compounds. *Environ. Sci. Technol. Lett.* 6, 184–190 (2019).

27. Lambe, A. T. *et al.* Relationship between Oxidation Level and Optical Properties of Secondary Organic Aerosol. *Environ. Sci. Technol.* 47, 6349–6357 (2013).

28. Rissler, J. *et al.* Size distribution and hygroscopic properties of aerosol particles from dry-season biomass burning in Amazonia. *Atmos. Chem. Phys.* 6, 471–491 (2006).

29. Hussein, T. *et al.* Urban aerosol number size distributions. *Atmos. Chem. Phys.* 4, 391–411 (2004).

30. Veihelmann, B., Konert, M. & van der Zande, W. J. Size distribution of mineral aerosol: using light-scattering models in laser particle sizing. *Appl. Optics* 45, 6022–6029 (2006).

31. Widmann, J. F., Duchez, J., Yang, J. C., Conny, J. M. & Mulholland, G. W. Measurement of the optical extinction coefficient of combustion-generated aerosol. *J. Aerosol. Sci.* 36, 283–289 (2005).

32. Sumlin, B. J. *et al.* UV–Vis–IR spectral complex refractive indices and optical properties of brown carbon aerosol from biomass burning. *Journal of Quantitative Spectroscopy and Radiative Transfer* 206, 392–398 (2018).

33. Sumlin, B. J. *et al.* Atmospheric Photooxidation Diminishes Light Absorption by Primary Brown Carbon Aerosol from Biomass Burning. *Environ. Sci. Technol. Lett.* 4, 540–545 (2017).

34. Nakayama, T., Sato, K., Imamura, T. & Matsumi, Y. Effect of Oxidation Process on Complex Refractive Index of Secondary Organic Aerosol Generated from Isoprene. *Environ. Sci. Technol.* 52, 2566–2574 (2018).

Chapter 6: Conclusions to Studies on The Production and Characteristics of Natural and Anthropogenic Aerosols

6.0 Overview

The preceding chapters examine the sources of aerosols in the Salton Sea Basin, the potential of heterocyclic compounds to form BrC, and the applications of a new tool to estimate aerosol refractive index uncertainties. Although not directly connected to one another, each project advances our understanding of aerosol dynamics, sources, or properties. Below the main conclusions and possible future directions of each study are discussed.

6.1 Salton Sea

Academic work surrounding the Salton Sea has spans many fields including volcanology, economics, ecology, limnology and water quality, atmospheric science, and environmental justice.[1-9] The work described in Chapters 2 and 3 delves into the emerging air quality challenges facing the region, and attempts to quantify important regional dust sources. Beyond allocating dust to sources, the controls on these dust sources are also discussed. One of the major findings of this work is the observation of seasonality in emissions from the Salton Sea Playa. This finding will hopefully inform mitigation efforts so dust suppression can be intensified during the late spring and early summer. Another finding of this work is the basin-wide seasonality observed in Se concentrations. This seasonality reveals that Se is likely not being permanently sequestered into Salton Sea sediments, but instead has an active atmospheric roll which warrants further investigation.

Lastly, this work reinforces findings by Buck et al. that mineral dynamics occurring on playa surfaces control playa emission potential.[10] Knowing this, future efforts to

understand playas and predict emission could be based on constructing a lab based, bottom up, model that incorporates groundwater movement and composition, evaporation-transpiration rates, and surface conditions. Such studies could help further understand when, where, and why a specific playa may become emissive. Such a predictive model could enable targeted mitigation or development of novel mitigation technologies.

6.2 Possible Steps to Mitigate Dust Levels in the Salton Sea Basin

In addition to understanding dust sources, it is also useful to consider possible steps which could be taken to mitigate dust levels in the Salton Sea Basin. The following are a series of recommendations which could improve air quality in the Salton Sea basin.

1. The Ocotillo Wells SRA, the open-ride off-road vehicle park to the west of the sea, assuredly reduces the occurrence of protective crusts and increases dust emission from this region.[11-13] To improve baseline air quality, OHV use could be limited to trails (as it is at many other OHV parks) or limited to before the rainy season, as rain can help create protective crusts on non-playa soils which will reduce dust emissions if allowed to exist through the windy months following the wet season. These trails could also be limited to soils with high sand content, as emission increases from OHV use on these soil types are relatively low. Although regularity entities are attempting to keep OHV use off playa surfaces, in areas of heavy OHV use, the mitigation efforts are focused on acute effects.[14] Longer-term impacts of OHV use on soil emissivity should be addressed if all air quality issues are to be addressed in the Salton Sea Basin.

2. Agricultural dust suppression could be increased by enforcing best management practices and implementing dust suppression technologies within the basin. These actions could include no-till warnings during high winds, incentives to keep crop cover during the windy season, and implementation of hardware to reduce acute emissions.
3. Targeted playa management also presents an option for more efficient playa management. Because playas are known to be most emissive after rain and during high wind events (late spring/early summer), active mitigation can be targeted to occur between these events.
4. Hydrologic engineering solutions may also provide one unexplored method of permanently managing playa emissions. It is likely that playa emissivity is controlled, largely, by water table height and salt movement through the soil column.[15] Given this, one possible solution to emissive playas would be to engineer lower water table heights below the playas. This might be possible using a series of wells to draw down the water table below the playas and force them into a "dry" state where they are much less emissive. Before such a solution is implemented, the hydrologic effects on the non-target areas and nearby agricultural fields needs to be examined. Non-target areas would include nearby wetlands and bird habitats and the Salton Sea itself.

These recommendations may help improve the air quality in the Salton Sea Basin and should be analyzed for their potential to improve air quality.

6.3 Refractive Indices and Brown Carbon

Chapter 4 reveals the potential of heterocyclic precursors, particularly pyrrole, to form BrC SOA. Interestingly, although gas phase furan is more abundant in biomass burning emissions, this work suggests that furan compounds are possibly less important to SOA formation and SOA absorption compared to its nitrogen-containing analog, i.e., pyrrole. Although informative, this work opens many questions regarding the role of these compounds, and associated SOA in the atmosphere. Future research efforts should attempt to identify SOA sourced from these compounds in the atmosphere and investigate other commonly emitted heterocyclic VOCs as BrC sources. This work also did not identify all the chromophores present in pyrrole SOA; as such, future investigations of this system should examine which chromophores are most important for pyrrole SOA absorption and their characteristics (e.g., lifetime and phase state).

To help understand the uncertainties in aerosol refractive index calculations (m), chapter 5 describes RICE, a method of estimating the confidence in m retrievals. RICE allows users to estimate the uncertainties associated with a single m retrieval using a full aerosol size distribution and the corresponding optical coefficients. This means that estimates of uncertainty can be based on a point by point confidence interval, not on an assumed to be representative test case. RICE will enable users to perform tasks like exploring if "interesting" data points were likely true, or estimating the uncertainties in quickly changing situations, such as field sampling. Overall, RICE provides a powerful tool for propagating uncertainty through refractive index retrievals. If used widely, it will

better constrain the uncertainty associated with aerosol refractive index calculations and lead to more accurate estimates of the aerosol direct radiative effect.

6.4 Works Cited

1 Adams, P. M., Lynch, D. K., Buckland, K. N., Johnson, P. D. & Tratt, D. M. Sulfate mineralogy of fumaroles in the Salton Sea Geothermal Field, Imperial County, California. *Journal of Volcanology and Geothermal Research* 347, 15-43, doi:10.1016/j.jvolgeores.2017.08.010 (2017).

2 Babcock, E. A. Geology of the Northeast Margin of the Salton Trough, Salton Sea, California. *Geological Society of America Bulletin* 85, 321-332, doi:10.1130/0016-7606(1974)85<321:GOTNMO>2.0.CO;2 (1974).

3 Levers, L. R., Skaggs, T. H. & Schwabe, K. A. Buying water for the environment: A hydro-economic analysis of Salton Sea inflows. *Agricultural Water Management* 213, 554-567, doi:10.1016/j.agwat.2018.10.041 (2019).

4 MacDougal, D. T. & Collaborators. The Salton Sea: A Study of the Geography, the Geology, the Floristics, and the Ecology of a Desert Basin. *New Phytologist* 13, 280-284, doi:10.1111/j.1469-8137.1914.tb05758.x (1914).

5 Anderson, M. A., Whiteaker, L., Wakefield, E. & Amrhein, C. Properties and distribution of sediment in the Salton Sea, California: an assessment of predictive models. *Hydrobiologia* 604, 97-110, doi:10.1007/s10750-008-9308-1 (2008).

6 de Koff, J. P., Anderson, M. A. & Amrhein, C. Geochemistry of iron in the Salton Sea, California. *Hydrobiologia* 604, 111-121, doi:10.1007/s10750-008-9322-3 (2008).

7 Henny, C. J., Anderson, T. W. & Crayon, J. J. Organochlorine pesticides, polychlorinated biphenyls, metals, and trace elements in waterbird eggs, Salton Sea, California, 2004. *Hydrobiologia* 604, 137-149, doi:10.1007/s10750-008-9320-5 (2008).

8 Reese, B. K. & Anderson, M. A. Dimethyl sulfide production in a saline eutrophic lake, Salton Sea, California. *Geochimica Et Cosmochimica Acta* 72, A781-A781 (2008).

9 Rodriguez, I. R., Amrhein, C. & Anderson, M. A. Reducing dissolved phosphorus loading to the Salton Sea with aluminum sulfate. *Hydrobiologia* 604, 37-44, doi:10.1007/s10750-008-9313-4 (2008).

10 Buck, B. J., King, J. & Etyemezian, V. Effects of Salt Mineralogy on Dust Emissions, Salton Sea, California. *Soil Science Society of America Journal* 75, 1971, doi:10.2136/sssaj2011.0049 (2011).

11 Baddock, M. C., Zobeck, T. M., Van Pelt, R. S. & Fredrickson, E. L. Dust emissions from undisturbed and disturbed, crusted playa surfaces: Cattle trampling effects. *Aeolian Research* 3, 31-41, doi:10.1016/j.aeolia.2011.03.007 (2011).

12 Goossens, D. Effect of soil crusting on the emission and transport of wind-eroded sediment: field measurements on loamy sandy soil. *Geomorphology* 58, 145-160, doi:10.1016/s0169-555x(03)00229-0 (2004).

13 Goossens, D. & Buck, B. Dust emission by off-road driving: Experiments on 17 arid soil types, Nevada, USA. *Geomorphology* 107, 118-138, doi:10.1016/j.geomorph.2008.12.001 (2009).

14 Dessert, M., Romero, R., Soucier, M. N., Blondell, C. & Hernandez , I. (California Air Resources Board, Imperial County Air Pollution Control District, Ramboll US Corporation, 2018).

15 Reynolds, R. L. *et al.* Dust emission from wet and dry playas in the Mojave Desert, USA. *Earth Surface Processes and Landforms* 32, 1811-1827, doi:10.1002/esp.1515 (2007).

Appendix 1: Appendix to Effects of a Receding Saline Lake (The Salton Sea) on Airborne Particulate Matter Composition

A1.1 Text

A1.1.1 Description of Trace Metal Digest Procedure

To determine total metal and metalloid concentrations, samples were placed in a Teflon vial, and 2.5 ml of concentrated HNO_3 and 0.5 ml of concentrated HF were added. All acids were sourced from Fisher Chemical and were trace metal grade or better. The closed vial was heated to 130-150 °C in an HEPA-filtered micro cleanroom, under negative pressure for 15 hours. While maintaining clean conditions, the vial was then uncapped and heated to 130 °C until ~0.5 ml of liquid remained. To assure total digestion of trace metals, 0.6 ml of concentrated HNO_3 and 1.8 ml of concentrated HCl were added to the vial for a second digestion. The closed vial was again heated on a hot plate to 130-150 °C for 15 hours. The vial was then uncapped and heated at 130 °C until ~0.5 ml of liquid remained. Finally, the solution was diluted with 2 ml of 5% HNO_3. The exact solution volume was determined by weighing the vial. The solution was transferred into an acid-cleaned 4 ml HDPE bottle and stored refrigerated until analysis.

An external geological standard (USGS G-2) was co-digested. For G-2, the relative method precision for all metals was better than 15%, while recovery of certified species, Na, Al, K, Ca, Mn, Fe was >79%. Co and Ba were the only certified species to display variation from the expected value by more than 21%. Lower than perfect mass recovery and some mass lost is expected as digests are known to have incomplete mass closure.[1]

All aerosol data were blank corrected using elemental concentrations from the digested field blanks.

PM_{10} mass concentrations of each element are calculated by summing the elemental concentration of all digests (0.056 – 10 µm) for a specific aerosol sampling period. Filter digests resulting in values that were below the method detection limit (BDL) for specific elements were included unadjusted in PM_{10} mass concentrations, as replacement of a BDL value with "0" may skew the results. For a small subset of filter digests (6 of 129) where contamination occurred during preparation, the median value of each element within the same size range was used to replace the missing values when calculating PM_{10} mass concentrations.

A1.1.2 Description of ED-XRF quantification

During ED-XRF analysis, United States Geologic Survey (USGS) standard reference material G-2 was also analyzed as an external standard. G-2 measurements were precise: all metals having an RSD of less than 7%. Variation from the expected value for certified species Na, Al, K, Ca, Fe was less than 30%. The only certified species to display error greater than 30% were Ti and Mn.

A1.1.3 Positive Matrix Factorization Case Description

Three separate PMF models were run using concentrations of each element within PM_{10}, PM_{10-1}, and PM_1. Missing data values (6 out of 129 digests), removed due to contamination during digestion, were replaced with the median value of the elemental mass concentration in that stage and given an uncertainty of 4 times this value. Below detection limit data were included to avoid introducing biases.[2] Internal PMF parameters, such as

Q_{robust}, Q_{true}, and $Q_{expected}$ were considered to assess performance of PMF. In general, Q is a measure of the fitness of the model; Q_{robust} is calculated using only samples that fit the model well, while all samples are used in calculating Q_{true}. $Q_{expected}$ is equal to the number of samples multiplied by the number of strong species. The normalized contribution of each factor was constrained to above -0.2, and Q_{robust} was used per the settings of EPA PMF 5.0. Only results from the PM_{10} model data are reported here, as the PM_{10}, PM_{10-1} and PM_1 results were observed to be qualitatively similar. Ca, Na, As, Al Fe, Mn, V, Ba, Co, Se, Ti, K were classified as strong and Ni, Cd, Cr as weak species. Weak species were identified by a S/N ratio of less than 2; S/N ratios were calculated by PMF 5.0. Fpeak was set to 0 and no species were constrained to preset values. After running the model with 2-7 factors, a 4 factor solution was selected because of a low $Q_{true}/Q_{expected}$ (5.8) (Fig. S9), small residuals for most species and samples, absence of rotational ambiguity, and reasonable factor compositions. Within this solution, only Cd, Se, and Ba did not produce normally distributed residuals. Furthermore, only weak species displayed R^2 between distributions of observed vs. predicted values of < 0.6, and most strong species displayed R^2 values > 0.9, demonstrating the ability of this solution set to reproduce the sample data well. The uncertainty was estimated using the displacement method (Paatero et al., 2014). Bootstrapping was not used because of the small size of the sample set. High uncertainties were observed in the contribution of certain species to each factor, but each factor contained at least one well-constrained species, highlighting the dominant chemical characteristic of that factor. These high uncertainties stem, in part, from the high and variable values of field blanks that are carried through the model. Rotational swaps,

indicating uncertainty in the identified components and their contributions, were not observed during displacement, and the largest change in Q was -0.01%, evidencing the good fit of the solution set.

A1.1.4 Temperature Description

Ambient temperature (Fig. S2b) also displayed expected diurnal and seasonal variation, with the highest temperatures observed during summer afternoons and lowest temperatures observed during winter mornings. Average temperatures for BBS, SCS, and SCW at 06:00 LT (a proxy for the daily minimum temperature) were 31.8 °C, 31.6 °C, and 15.9 °C, respectively. Average temperatures for BBS, SCS, and SCW at 15:00 LT (a proxy for the daily maximum temperature) were 41.5 °C, 41.3 °C, and 29.7 °C, respectively.

A1.1.5 Wind Direction Analysis

For SCS and BBS daytime wind values were well confined: during the day at SCS, greater than 60% occurrence of easterly winds (wind direction between 67.5° and 112.5°) was observed, while at BBS, wind direction was predominantly southeasterly/southerly (wind direction between 112.5° and 202.5°). SCS and BBS night periods were more variable, with no octant having a probability greater than 35%. Despite this, BBS night wind directions varied primarily between southwesterly and southeasterly, with very low probabilities of northerly winds. SCW winds displayed the opposite diurnal variability trend, with night values having a dominant (90% probability) westerly wind direction (between 202.5° and 292.5°). No wind direction octant displayed greater than 25% probability during the day SCW periods.

A1.2 Tables

Element	Average Desert, ppm	Average Playa, ppm	P Value, Playa vs Desert
Na	7.3e3 ± 3.3e3	7.2e4 ± 4.3e4	0.01
AL	4e4 ± 1.6e4	2.5e4 ± 8.2e3	0.04
K	1.4e4 ± 4.5e3	1.0e4 ± 2.5e3	0.04
Ca	2.9e4 ± 1.7e4	4.7e4 ± 1.4e4	0.02
Ti	3e4 ± 950	1.3e3 ± 460	0.00
V	55 ± 21	31 ± 14	0.02
Cr	31 ±13	18 ± 8	0.03
Mn	420 ± 180	210 ± 80	0.01
Fe	1.7e4 ± 8.8e3	1.0e4 ± 5.6e3	0.09
Co	6 ± 3	3 ± 2	0.03
Ni	13 ± 7	8 ± 4	0.12
Cu	15 ± 9	16 ± 18	0.15
Zn	49 ± 22	33 ± 15	0.15
As	7 ± 5	5 ± 3	0.27
Se	0.1 ± 0.1	0.5 ± 0.3	0.01
Cd	0.2 ± 0.1	0.2 ± 0.1	0.53
Ba	520 ± 200	250 ± 40	0.00
Pb	14 ± 6	7 ± 2	0.00

Table A1.1. Average elemental concentrations of playa and desert soils samples as measured via ICP-MS. P values were calculated from a two tailed, heteroscedastic, student's T test between the desert and playa samples. P value less than or equal to 0.05 are highlighted.

Element	Average Desert, ppm	Average Playa, ppm	P Value, Playa vs Desert
Na	1.3e4 ± 5.e3	1.3e5 ± 8.3e4	0.00
Al	7.9e4 ± 1.2e4	5.2e4 ± 2.2e4	0.00
K	1.8e4 ± 2e3	1.2e4 ± 5e3	0.00
Ca	4.5e4 ± 9e3	5.9e4 ± 2.1e4	0.00
Ti	3.4e3 ± 1e3	1.8e3 ± 1e3	0.00
V	60 ± 20	50 ± 20	0.02
Cr	40 ± 10	20 ± 20	0.00
Mn	410 ± 100	250 ± 150	0.00
Fe	2.4e4 ± 6e3	1.5e4 ± 1.0e4	0.00
Co	50%<BDL	50%<BDL	NA
Zn	50 ± 20	40 ± 20	0.00
As	50%<BDL	10 ± 20	0.95
Se	50%<BDL	2 ± 2	0.00
Cd	50%<BDL	50%<BDL	NA
Pb	23 ± 5	15 ± 5	0.00

Table A1.2. Average elemental concentrations of playa and desert soils samples as measured via ED-XRF. P values were calculated from a two tailed, heteroscedastic, student's T test between the desert and playa samples. P value less than or equal to 0.05 are highlighted.

Element	Median, PM_{10}, ng m^{-1}	Summer PM_{10}, ng m^{-1}	Winter PM_{10}, ng m^{-1}	Cal EPA Reference Exposure Levels, ng m^{-1}	P Value Summer vs.Winter
Na	480	850 ± 690	370 ± 160	NA	0.02
Al	620	870 ± 580	1e3 ± 880	NA	0.69
K	280	380 ± 270	410 ± 280	NA	0.78
Ca	670	940 ± 1.0e3	1.4e3 ± 1.8e3	NA	0.43
Ti	44	63 ± 39	57 ± 46	NA	0.75
V	1.8	2.1 ± 1.3	1.9 ± 1.4	NA	0.64
Cr	9	12.4 ± 8.8	11.1 ± 9.8	200 (Cr VI)	0.74
Mn	9.2	13.2 ± 9.3	12.2 ± 8.7	90	0.78
Fe	390	600 ± 430	540 ± 410	NA	0.72
Co	0.3	0.4 ± 0.2	0.4 ± 0.3	NA	0.63
Ni	5.7	8 ± 4.7	8 ± 8.3	14	1.00
As	0.5	0.7 ± 0.7	0.4 ± 0.2	15	0.14
Se	0.9	2.2 ± 2.7	0.3 ± 0.4	20000	0.02
Cd	0.05	0.42 ± 1.01	0.06 ± 0.03	20	0.20
Ba	15	24 ± 19	16 ± 8	NA	0.19

Table A1.3. Median, seasonal average, and standard deviations of PM_{10} elemental concentrations, as measured via ICP-MS. P values were calculated from a two tailed, heteroscedastic, student's T test between the summer and winter samples. P value less than or equal to 0.05 are highlighted.

Element	Median EF	Average Summer EF	Average Winter EF	P Value, Summer vs. Winter
Na	2.2	3 ± 0.79	1.7 ± 1.3	0.011
K	1.1	1.2 ± 0.33	1.3 ± 0.34	0.715
Ca	2.3	2.8 ± 2.7	2.5 ± 2.5	0.56
Ti	1.6	1.9 ± 0.66	1.5 ± 0.39	0.074
V	1.5	2.2 ± 1	1.7 ± 0.92	0.17
Cr	31	40 ± 33	30 ± 14	0.33
Mn	2.1	2.3 ± 0.36	2.1 ± 0.99	0.5
Fe	1.6	1.7 ± 0.39	1.5 ± 0.55	0.33
Co	3	4.2 ± 3.1	2.9 ± 0.92	0.17
Ni	42	48 ± 28	39 ± 20	0.39
As	27	21 ± 12	21 ± 10	0.034
Se	1200	2200 ± 1200	400 ± 460	0.0001
Cd	64	610 ± 1400	61 ± 31	0.15
Ba	2.9	3.7 ± 3.7	2.5 ± 1.2	0.24

Table A1.4: Median, seasonal average, and standard deviation of PM_{10} EFs. P values were calculated from a two tailed, heteroscedastic, student's T test between the summer and winter samples. P values less than or equal to 0.05 are highlighted.

A1.3 Figures

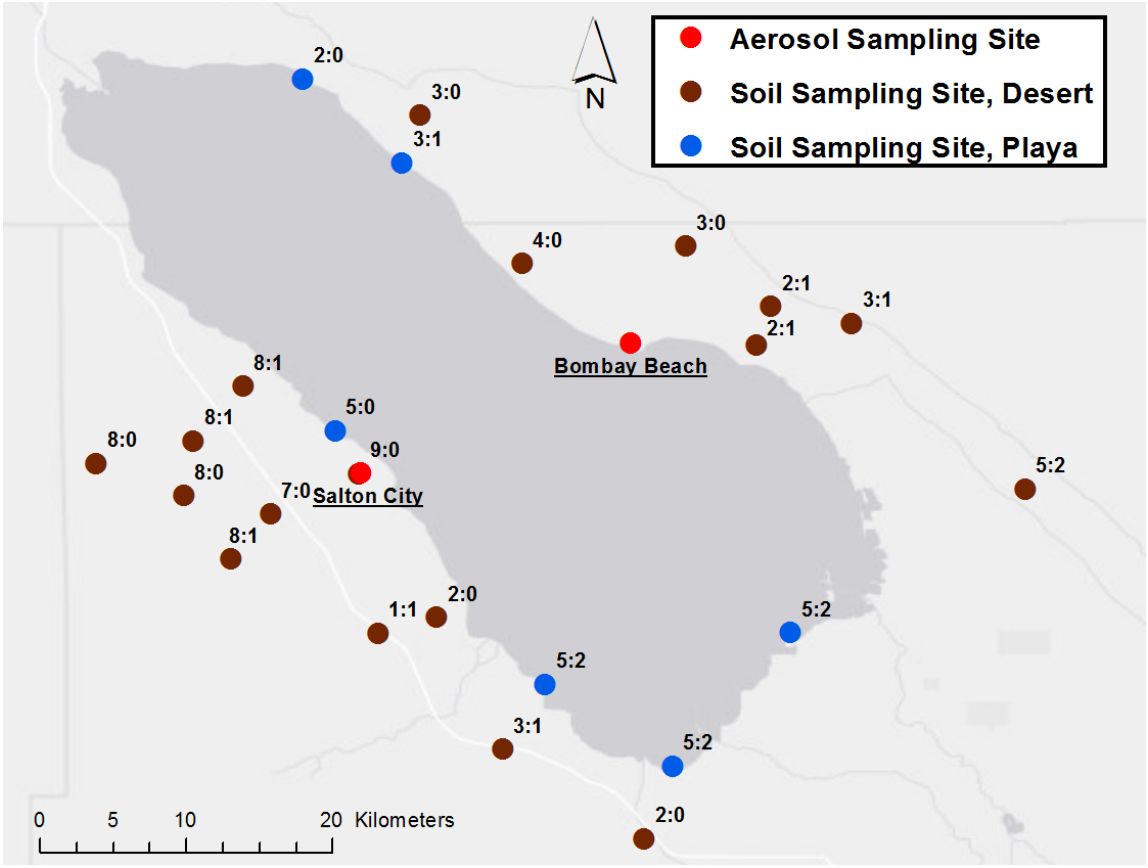

Figure A1.1. Map of soil and aerosol sampling sites. Labels represent the number of ED-XRF and ICP-MS analyzed soil samples from each site, presented as ED-XRF;ICP-MS.

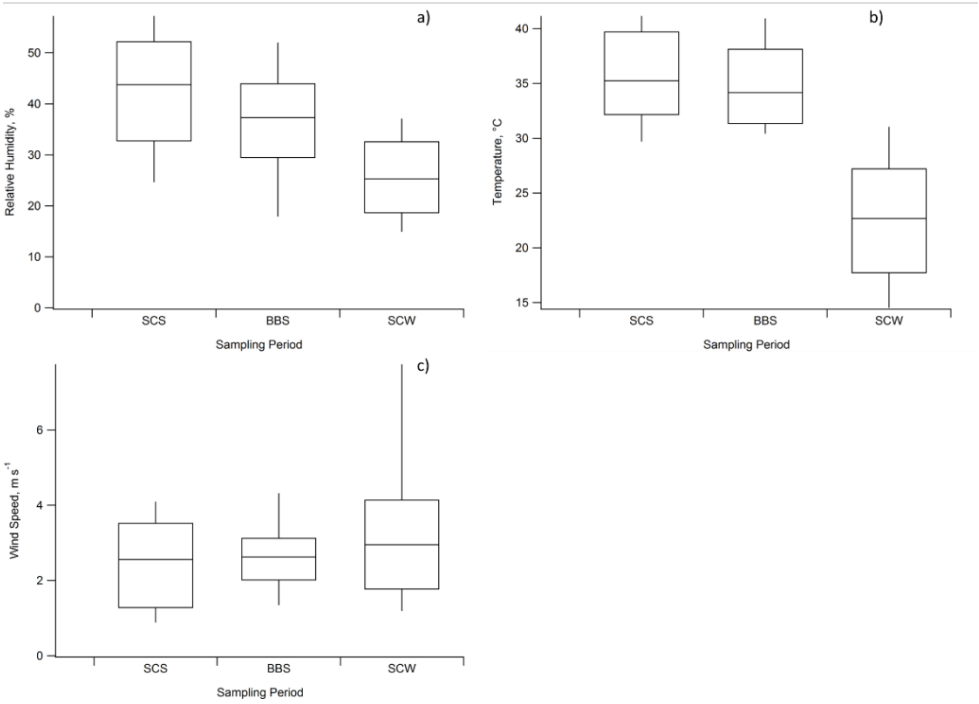

Figure A1.2. Meteorological data measured by the Imperial Irrigation District and downloaded from California's Air Quality Monitoring Information System Query Tool during aerosol sampling periods: Salton City Summer (SCS), Bombay Beach Summer (BBS), and Salton City Winter (SCW). Hourly averaged distributions of (a) relative humidity, (b) temperature, and (c) wind speed are reported. Box and whiskers highlight 10th, 25th, 50th, 75th, and 90th percentiles.

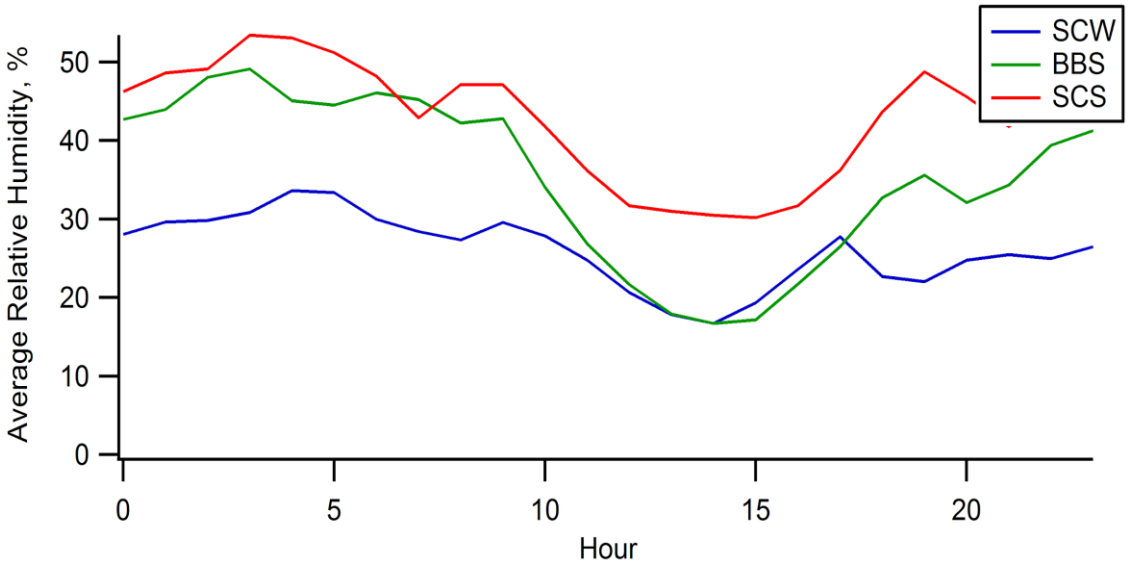

Figure A1.3: Average diurnal relative humidity pattern for Salton City Winter (SCW, Blue), Bombay Beach Summer (BBS, green), and Salton City Summer (SCS, red).

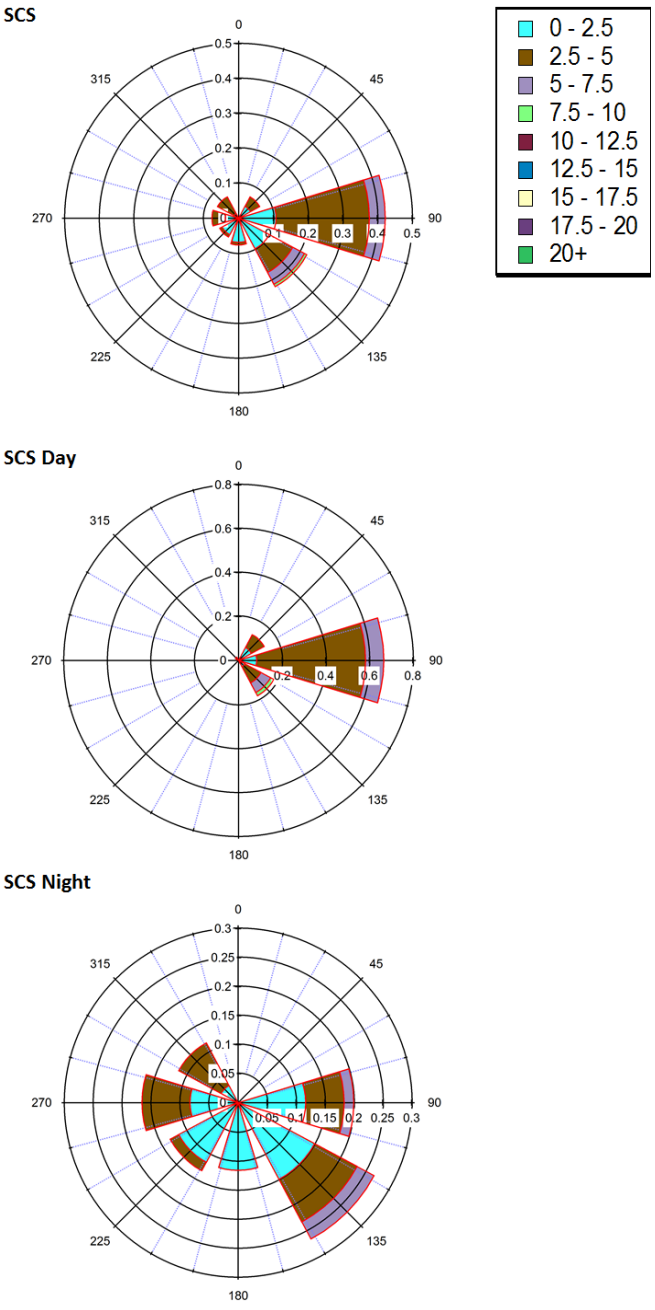

Figure A1.4: Wind Roses for Salton City Summer (SCS) sampling period. The probability of wind being sourced from a given direction is represented by the size of the colored portion and the colors represent wind speed probabilities in m s^{-1}.

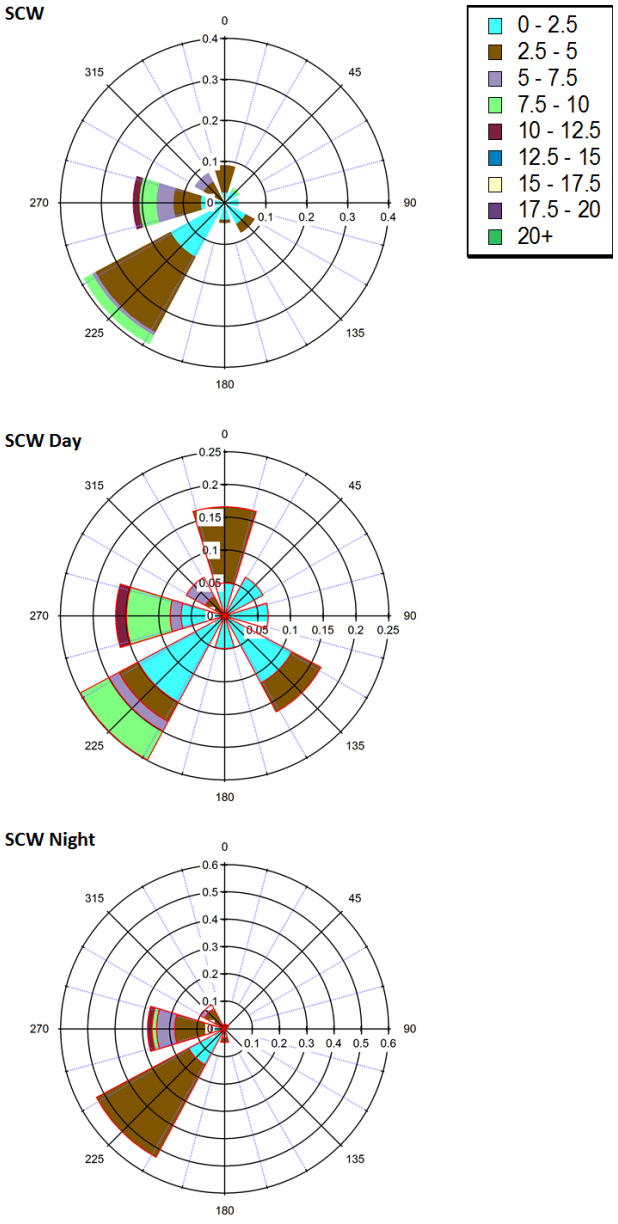

Figure A1.5: Wind Roses for Salton City Winter (SCW) sampling period. The probability of wind being sourced from a given direction is represented by the size of the colored portion and the colors represent wind speed probabilities in m s^{-1}.

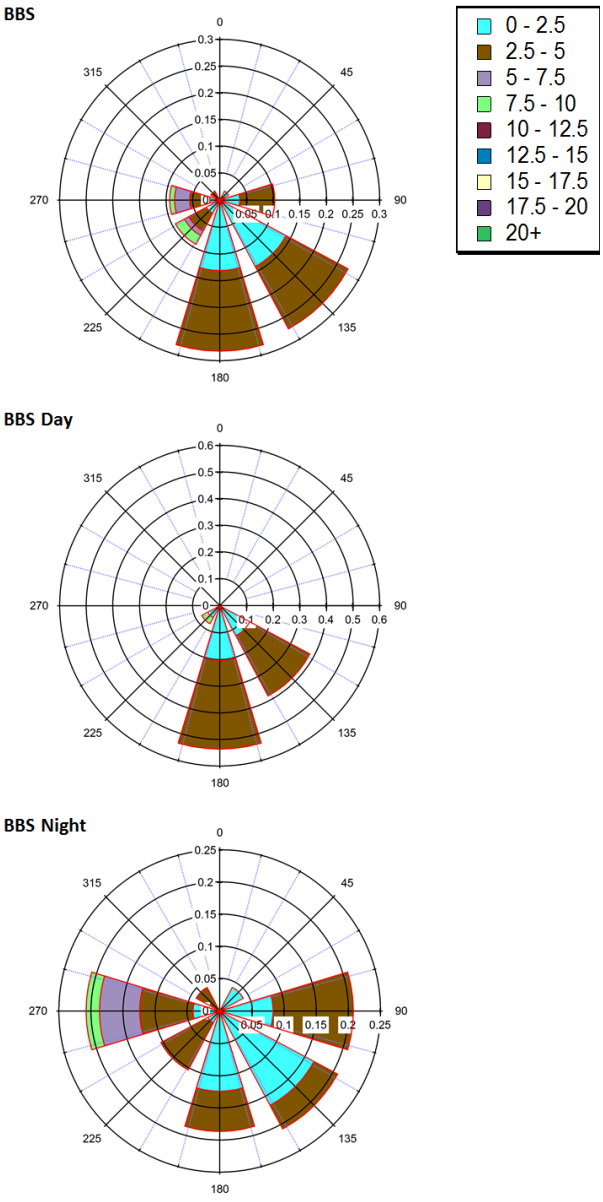

Figure A1.6: Wind Roses for Bombay Beach Summer (BBS) sampling period. The probability of wind being sourced from a given direction is represented by the size of the colored portion and the colors represent wind speed probabilities in m s^{-1}.

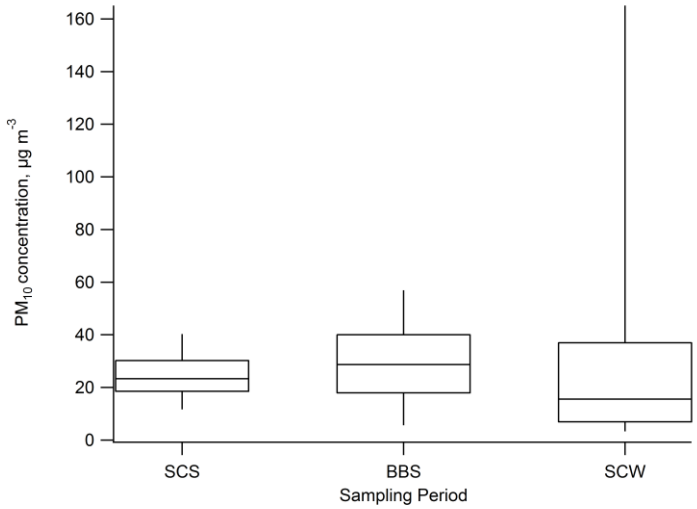

Figure A1.7. PM_{10} mass concentration as measured by the Imperial Irrigation District and downloaded from California's Air Quality Monitoring Information System Query Tool during aerosol sampling periods: Salton City Summer (SCS), Bombay Beach Summer (BBS), and Salton City Winter (SCW). Box and whiskers highlight 10^{th}, 25^{th}, 50^{th}, 75^{th}, and 90^{th} percentiles.

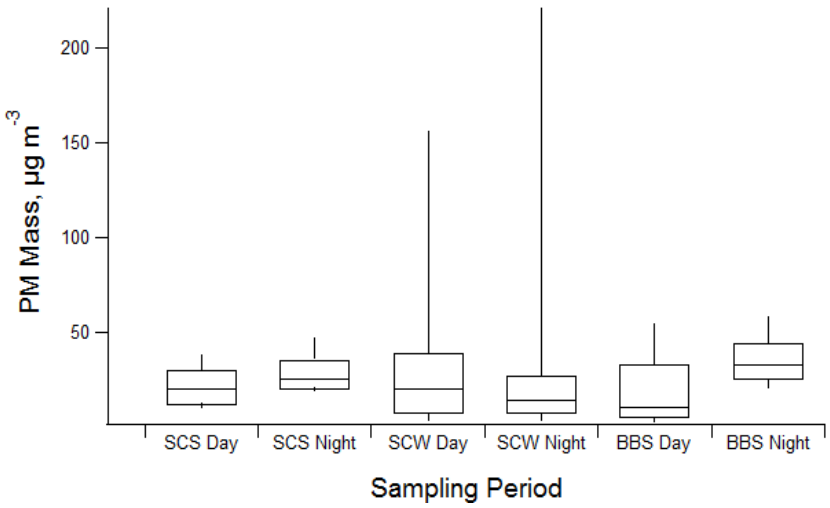

Figure A1.8. Diurnal PM_{10} mass concentrations during Salton City Summer (SCS), Salton City Winter (SCW), and Bombay Beach Summer (BBS) sampling as measured by TEOM (Imperial Irrigation District, data available through the AQMIS).

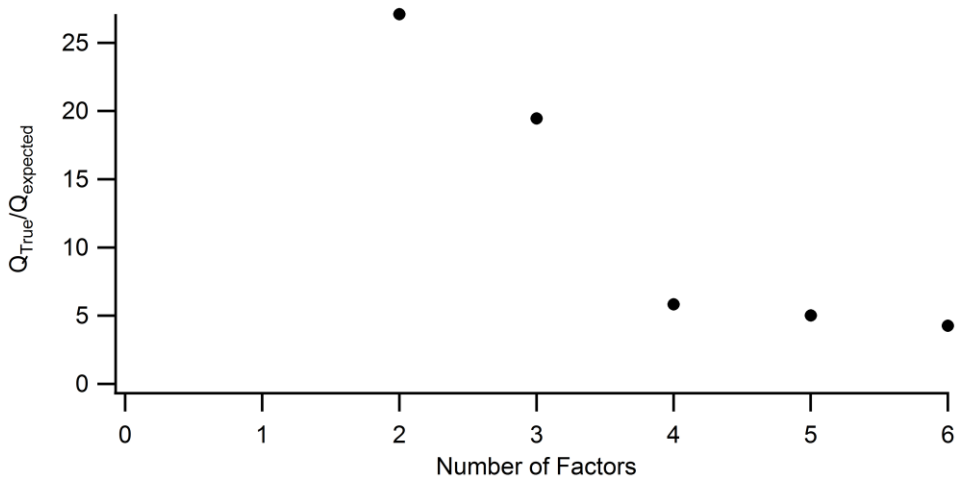

Figure A1.9. $Q_{true}/Q_{expected}$ ratio of positive matrix factorization results with different factor number inputs. A 4 factor model was selected as being the most accurate to describe the data because the change in $Q_{true}/Q_{expected}$ was insignificant after addition of another factor.

Appendix 2: Appendix to Dust Sources in the Salton Sea Basin: A Clear Case of an Anthropogenically Impacted Dust Budget

A2.1 Text

A2.1.1 Sampling Handling and Treatment

Before each deployment, samplers were acid washed in 2% nitric acid. When Samplers were deployed and removed from the field, they were enclosed in ziplock bags pre-rinsed with ultrapure water. Samples were stored under laboratory conditions (~22°C) until extraction. To extract the sample, the inside surface of the pan, the Teflon mesh, and the marbles were all rinsed with ultrapure water. A silicon brush was used to physically disrupt dust particles on the pan and mesh to maximize dust collection. Large pieces of organic matter (e.g. bugs or leaves) were physically removed from the extract. The resulting suspension was dried in a muffle furnace at 100°C. The remaining solid was weighed (Mettler AE 260, 10^{-4} g). To understand sources of error, a method blank was prepared as a typical sampler but not deployed in the field before extraction.

A2.1.2 Digestion for Trace Metal Analysis

About 30 mg of sample was ashed at 500 °C for 18 hours to remove organic matter. The sample was then suspended in a solution of concentrated nitric acid (1.5 ml) and concentrated hydrofluoric acid (0.5 ml) in a Teflon Vial. The closed vial was heated at 140 °C for 16 hours in a custom HEPA-filtered mini clean box. Next, the top was removed from the vials and the solution was boiled off at 120 °C until ~0.25 ml remained. The solution was then reconstituted in 1.25 ml HCl and 0.5 ml HNO3 and heated at 140 °C for 16 hours. The solution was again dried to ~0.25 ml and reconstituted in 5% nitric solution

(5 ml) until analysis with ICP-MS. Calibration curves were created from 1000 ug ml^{-1} stock solutions (Inorganic Ventures or Aristar Plus).

Additionally, five replicates of an external geologic standard, NIST-2702 (Inorganics in Marine Sediment), were digested and analyzed to analyze the accuracy of the digestion. Average values of these standards displayed <10% difference from published values for Al, As, Ba, Co, Cr, Cu, K, Mg, Mn, Na, Ni, Pb, Sr, Ti, V, and Zn. The difference was <30 % for all other elements except Ca (driven by a single anomalous replicate) and Cd (40% and 90%, respectively).

A2.1.3 Ion Chromatography Analysis

To measure the soluble anion content, 10 mg of sample was suspended in 10 ml of ultra-pure water, sonicated for 60 minutes, then filtered through a 0.22 µm Teflon filter. Soluble anion extracts were analyzed with ion chromatography (IC). For analysis, a 3.5 mM $NaCO_3$ and 1.0 mM $NaHCO_3$ buffer was used as eluent through a 4 mm anion-exchange column (AS14, Dionex IonPac). Anion signal was suppressed before detection (Dionex AERS 500, Thermo scientific) and anions were detected using a heated conductivity cell (DS6, Thermo Scientific). A calibration curve of known anion concentrations was created by diluting stock solutions of SO_4^{2-} (LabChem, 1000 mg/kg), PO_4^{3-} (Spex CertiPrep, 1000 mg/kg), NO_3^- (Spex CertiPrep, 1000 mg/kg), NO_2^- (High-Purity Standards, 100 mg/kg), and Cl^- (BDH, 1000 mg/kg). This curve was used to determine soluble anion concentrations in the extract solutions.

A2.1.4 PMF Uncertainty Treatment

Uncertainty values (σ_{PMF}) were calculated using a modified square root of the sum of squares method (Eq. A2.1).

$$\sigma_{PMF} = \sqrt{\left(M\sqrt{{\sigma_I}^2 + {\sigma_B}^2 + {\sigma_{Dil}}^2}\right)^2 + {\sigma_{MB}}^2} \quad \text{(A2.1)}$$

Where M is the mass dilution modifier which converts concentration uncertainties to mass uncertainties, σ_I is the analytical uncertainty defined as the standard deviation (SD) reported by the instrument for a given sample for ICP-MS data and the SD of calibration curve replicates for IC data, σ_B the SD in analytical blank values, σ_{dil} the uncertainty associated with weighing and diluting of the sample, σ_{MB} the uncertainty in method blank values, which is assumed to be 100% of the method blank value. For Mass and fraction organic matter (f_{org}), σ_{PMF} was set to 0.33 of the measured value; this is unlikely to affect the final result as both species were input as weak variables.

Both IC and ICP-MS data contained below detection limit (BDL) values for the measurements; uncertainty in these values (σ_{PMF_BDL}) was determined using Eq. A2.2:

$$\sigma_{PMF\_BDL} = \sqrt{\left(M\sqrt{{\sigma_I}^2 + (\frac{5}{6} * (c_B + 3 * \sigma_B))^2 + {\sigma_{Dil}}^2}\right)^2 + {\sigma_{MB}}^2} \quad \text{(A2.2)}$$

Where C_B is the average concentration of a species measured within blanks. σ_{MB} is not modified for BDL data because σ_{MB} is assumed to be 100 % of the method blank concentration. Additionally, 10% uncertainty was added to all species because at base uncertainty levels, many PMF runs were non-convergent, indicating an underestimation of

the uncertainties. This additional uncertainty could arise from uncertainties associated with the sampling technique, which are known to be relatively large.[1]

For ICP-MS there no were missing samples, but due to limited mass, some samples were unable to be analyzed using the IC. Soluble anion fluxes for these samples were input as the median concentration value of measured samples from the site. Uncertainty for these values were set to 4x the replacement value [2]

A2.1.5 X-Ray Diffraction

The following describes the XRD analysis of the SB April 2018 sample (Figure A2.14). The sample was mounted as a randomly oriented powder on an Al holder and analyzed using a Siemens D500 XRD with a CuKα X-ray source operating at 40 kV. Data were collected between 2-70° 2θ at a 0.01° step size and dwell time of 2 s. Alignment was calibrated using a quartz slide, and quartz in the sample was used as an additional internal calibration check. Background removal was performed using JADE software (MDI). Peak positions and intensities were assigned using reference diffraction data from the Joint Committee on Powder Diffraction Standards mineral database.

A2.1.6 HYSPLIT Analysis

NOAA's HYbrid Single Particle Lagrangian Integrated Trajectory model (HYSPLIT4, SVN 951) was used to probe possible source regions and possible regions of downwind effect. Calculations were performed using archived North America Regional Reanalysis Data.[3] Trajectories were explored using the SB site as a starting point. From this location, 12 hour back trajectories were calculated every 2 hours for the duration of each sampling period (Figure A2.6). Trajectories were capped at 10,000 m above ground

level, but only trajectories below 1,000 m are shown in Figure A2.6.

To investigate the potential downwind impacts of playa emissions, 72 hour forward trajectories were calculated for SB at 04:00 UTC (20:00 local time) every 24 hours from March 1st 2018 until June 29th 2018. This time period was chosen because it overlaps the sampling periods when the *playa* source was the strongest. Forward trajectories were initialized at 20:00 local time because meteorological data showed peaks in daily wind speed in the evening (Figure A2.8) during the calendar month April 2018, which coincided with the sampling period with strongest playa emissions. Trajectories were capped at 10,000 m above ground level. A trajectory frequency plot of these analyses is included in Figure A2.7.

A2.2 Tables

Table A2.1. Start and stop dates for each site and each sampling period. Gaps in DP column are due to site inaccessibility.

	SB Start	SB Stop	WI Start	WI Stop	DP Start	DP Stop	PD Start	PD Stop	BD Start	BD Stop
May 2017	2017-04-28	2017-06-02	2017-05-02	2017-06-02	2017-05-02	2017-06-02	2017-04-28	2017-06-01	2017-05-02	2017-06-01
Jun. 2017	2017-06-02	2017-06-28	2017-06-02	2017-06-28	2017-06-02	2017-06-28	2017-06-01	2017-06-27	2017-06-01	2017-06-27
Jul. 2017	2017-06-28	2017-07-28	2017-06-28	2017-07-28	2017-06-28	2017-07-28	2017-06-27	2017-07-28	2017-06-27	2017-07-28
Aug. 2017	2017-07-28	2017-08-27	2017-07-28	2017-08-27	2017-07-28	2017-08-27	2017-07-28	2017-08-28	2017-07-28	2017-08-28
Sept. 2017	2017-08-27	2017-09-25	2017-08-27	2017-09-25			2017-08-28	2017-09-25	2017-08-28	2017-09-25
Oct. 2017	2017-09-25	2017-10-22	2017-09-25	2017-10-22	2017-08-27	2017-10-22	2017-09-25	2017-10-21	2017-09-25	2017-10-21
Nov. 2017	2017-10-22	2017-12-10	2017-10-22	2017-12-10	2017-10-22	2017-12-10	2017-10-21	2017-12-05	2017-10-21	2017-12-05
Dec. 2017	2017-12-10	2018-01-13	2017-12-10	2018-01-13	2017-12-10	2018-01-13	2017-12-05	2018-01-13	2017-12-05	2018-01-13
Jan. 2018	2018-01-13	2018-02-11	2018-01-13	2018-02-11	2018-01-13	2018-02-11	2018-01-13	2018-02-11	2018-01-13	2018-02-07
Feb. 2018	2018-02-11	2018-03-13	2018-02-11	2018-03-13			2018-02-11	2018-03-13	2018-02-07	2018-03-13
Apr 2018	2018-03-13	2018-05-02	2018-03-13	2018-05-02	2018-02-11	2018-05-02	2018-03-13	2018-05-02	2018-03-13	2018-05-02

Table A2.2. Historic average monthly wind speed, percentile rank of average monthly wind speed during sampling, and concurrent observed monthly average wind speed during sampling for different sites in the Salton Sea Basin.[4] Concurrent indicates to the calendar month which is not exactly the corresponding sampling period. Sites chosen were Palm Springs Airport (33.8222, -116.5043) Desert Resorts Regional Airport (33.62833 N, -116.16717 W), Imperial Airport (32.83000 N, -115.57182 W)

Palm Springs Airport (1998-2018)	May	Jun.	Jul.	Aug.	Sep.	Oct.	Nov.	Dec.	Jan.	Feb.	Mar.	Apr.
Historic ($m\ s^{-1}$)	4.9 ± 0.7	5.2 ± 0.6	6.5 ± 0.5	80 ±.5	8.7 ± 0.6	8 ± 0.8	7.1 ± 0.5	6.4 ± 0.4	6.4 ± 0.7	6 ± 0.5	5.1 ± 0.6	4.8 ± 0.7
Concurrent ($m\ s^{-1}$)	8.1	7.6	6.3	6.7	7.4	5.6	3.8	5.1	4.3	5.4	6.3	7.6
Percentile Rank	0.1	0.48	0.05	0.9	0.95	0.47	0.1	0.9	0.1	0.55	0.3	0.38
Desert Resorts Airport (2000-2018)												
Historic ($m\ s^{-1}$)	9.3 ± 0.8	8.3 ± 0.8	7.1 ± 0.6	6.5 ± 0.4	6.4 ± 0.8	6 ± 0.6	4.8 ± 0.6	4.4 ± 0.5	4.6 ± 0.6	5.5 ± 0.5	7.1 ± 0.6	8.9 ± 0.9
Concurrent ($m\ s^{-1}$)	9.2	7.8	6.5	7.4	7.8	6.3	4	5.4	4	5.8	7.2	10.1
Percentile Rank	0.56	0.28	0.17	1	1	0.58	0.11	1	0.11	0.67	0.72	0.89
Imperial Airport (2000-2018)												
Historic ($m\ s^{-1}$)	8.8 ± 1.2	8.3 ± 0.8	7.8 ± 0.6	6.8 ± 0.6	6.3 ± 0.9	6.2 ± 0.7	5.4 ± 0.8	5.1 ± 0.6	6.3 ± 0.8	7.7 ± 1	9.2 ± 1.1	5.1 ± 0.7
Concurrent ($m\ s^{-1}$)	9.2	7.6	8.3	7.2	7.8	5.6	4.3	4.5	4.7	6	8.1	8.9
Percentile Rank	0.67	0.33	0.72	0.89	1	0.26	0.11	0.17	0.5	0.33	0.67	0.61

Table A2.3. Percentile rank for the sum of precipitation during the rainy season (September - March) prior to sampling (16-17) and during sampling (17-18).[4] Sites chosen were Boyd Deep (33.6514, -116.3764), Desert Resorts Regional Airport (DRRA) (33.62833 N, -116.16717 W), Mecca Fire Station (33.5714 N, 116.0767), El Centro (32.7669, -115.5617), and Imperial (32.8488 N, -115.5666 W).

Site	Years of Data	Winter Precipitation Percentile	
		16-17	17-18
Boyd Deep	1963 - 2018	0.89	0.22
DRRA	1950 - 2018	0.84	0.44
Mecca	1905 - 2018	0.74	0.28
El Centro	1932 - 2018	0.73	0.06
Imperial	1902 - 2018	0.71	0.62

Table A2.4. PMF produced base profiles of each source in ppm (μg g^{-1}), as calculated by dividing the PMF estimated mass contribution of a species by the total mass contribution. Parenthetical text denotes the confidence in the attribution. Confidence in attributions is defined by the relative negative uncertainty as given by the displacement method. Intervals were defined as confident (C) (<0.25), Semi-Confident (SC) (<0.5), Low-Confidence (LC) (<0.75), and (NC) (<1) No-Confidence. Note that the confidence is less meaning for weak species, denoted by (W).

	Biomass Burning	Local Alluvium	Playa	Anthropogenic Trace Metals	Anthropogenic Copper	Colorado Alluvium	Sea Spray
Mass (W)	SC	SC	C	LC	NC	SC	SC
f_{org} (W)	280000 (C)	74000 (SC)	20000 0 (C)	0 (NC)	170000 (LC)	170000 (SC)	100000 (LC)
Na	16000 (NC)	20000 (SC)	29000 (SC)	92000 (SC)	15000 (NC)	18000 (LC)	170000 (SC)
Mg	16000 (NC)	20000 (SC)	49000 (C)	11000 (NC)	20000 (NC)	19000 (LC)	15 (NC)
Al	35000 (LC)	69000 (SC)	20000 (LC)	67000 (NC)	62000 (NC)	41000 (SC)	68000 (NC)
K	21000 (SC)	23000 (SC)	8500 (LC)	18000 (NC)	18000 (NC)	10000 (LC)	34000 (LC)
Ca	38000 (LC)	33000 (SC)	60000 (SC)	50000 (LC)	36000 (NC)	50000 (SC)	72000 (LC)
Ti	1800 (LC)	4900 (SC)	1100 (NC)	4100 (NC)	3600 (NC)	830 (NC)	2100 (NC)
V	45 (LC)	98 (SC)	27 (LC)	67 (NC)	73 (NC)	29 (NC)	88 (NC)
Cr	36 (LC)	66 (SC)	15 (NC)	66 (NC)	54 (NC)	33 (LC)	91 (LC)
Mn	360 (LC)	810 (SC)	200 (LC)	550 (NC)	630 (NC)	210 (NC)	580 (NC)
Fe	16000 (LC)	46000 (SC)	9300 (NC)	35000 (NC)	33000 (NC)	9200 (NC)	40000 (NC)
Co	4.8 (NC)	18 (SC)	3.8 (NC)	12 (NC)	12 (NC)	0 (NC)	2.5 (NC)
Ni	18 (LC)	31 (SC)	5.9 (NC)	29 (NC)	28 (NC)	14 (LC)	48 (LC)
Cu	0 (NC)	18 (NC)	0 (NC)	190 (NC)	1400 (C)	72 (NC)	480 (NC)
Zn	240 (SC)	210 (SC)	28 (NC)	910 (SC)	250 (NC)	110 (LC)	0 (NC)
As	0 (NC)	3.1 (NC)	3.4 (NC)	260 (C)	0.83 (NC)	19 (SC)	25 (NC)
Se	5 (NC)	4.1 (SC)	1.1 (NC)	0 (NC)	4.2 (NC)	4.4 (SC)	29 (SC)

Sr	220 (NC)	340 (SC)	780 (SC)	730 (LC)	290 (NC)	250 (NC)	160 (NC)
Mo	2.3 (SC)	2 (SC)	1 (LC)	4.7 (LC)	1.7 (NC)	1.5 (LC)	3.7 (LC)
Cd	0.1 (NC)	0.32 (LC)	0.096 (NC)	7.1 (C)	0.35 (NC)	1.4 (SC)	2.1 (LC)
Sn (W)	11 (LC)	3.5 (LC)	0 (NC)	100 (C)	0 (NC)	6.6 (SC)	49 (SC)
Sb	6.9 (NC)	0 (NC)	0 (NC)	280 (C)	11 (NC)	0 (NC)	0 (NC)
Ba	3.8 (NC)	810 (SC)	200 (NC)	1700 (LC)	470 (NC)	190 (NC)	1200 (LC)
Pb	5.4 (NC)	24 (SC)	3.1 (NC)	59 (SC)	18 (NC)	14 (SC)	32 (LC)
Th	3.9 (NC)	5.9 (SC)	1.5 (NC)	2.4 (NC)	5.1 (NC)	9.2 (SC)	4.8 (NC)
U	0.83 (NC)	0.24 (NC)	0.48 (NC)	0 (NC)	0.62 (NC)	4 (C)	0 (NC)
Cl-	31000 (NC)	0 (NC)	28000 (NC)	0 (NC)	480 (NC)	0 (NC)	740000 (SC)
NO_3^- (W)	0 (NC)	0 (NC)	540 (NC)	5500 (NC)	9300 (NC)	9400 (NC)	64000 (NC)
NO_2^- (W)	550 (C)	68 (SC)	0 (NC)	290 (C)	86 (LC)	68 (SC)	200 (SC)
PO_4^{3-}	23000 (C)	0 (NC)	61 (NC)	0 (NC)	480 (NC)	0 (NC)	2100 (NC)
SO_4^{2-}	7000 (NC)	13000 (NC)	290000 (C)	11000 (NC)	37000 (NC)	33000 (NC)	210000 (NC)

A2.2 Figures

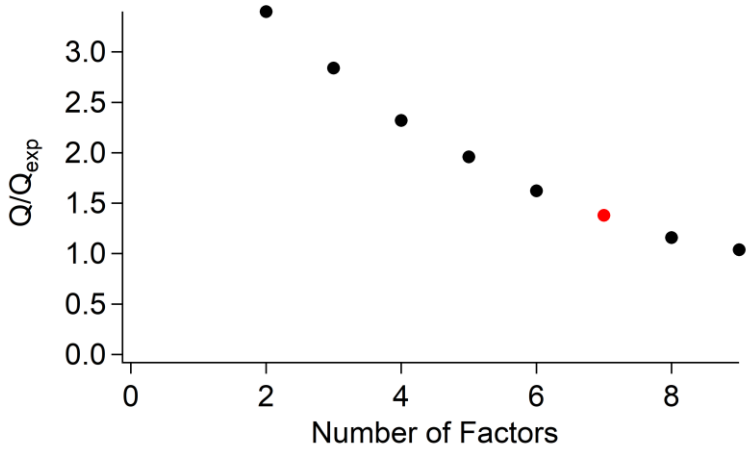

Figure A2.1. Q to Q expected ratio vs number of factors fit with PMF. Red dot represents the 7 factor solution chosen in this work.

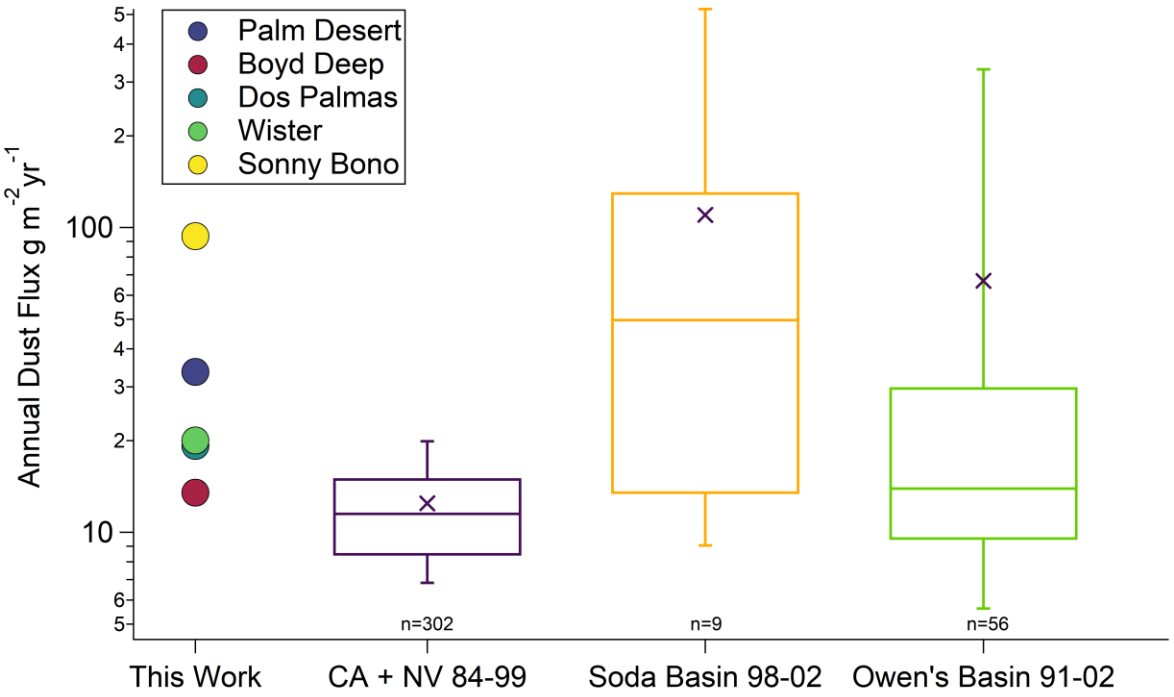

Figure A2.2. Yearly mass flux data from this study (dots) compared to historic mass flux measurements from similar samplers.[5] Within the box and whiskers, the centerline represents the median of the data, x represents the mean, the top and bottom of the box correspond to the 75th and 25th percentiles, respectively, and the top and bottom whisker correspond to the 90th and 10th percentiles, respectively.

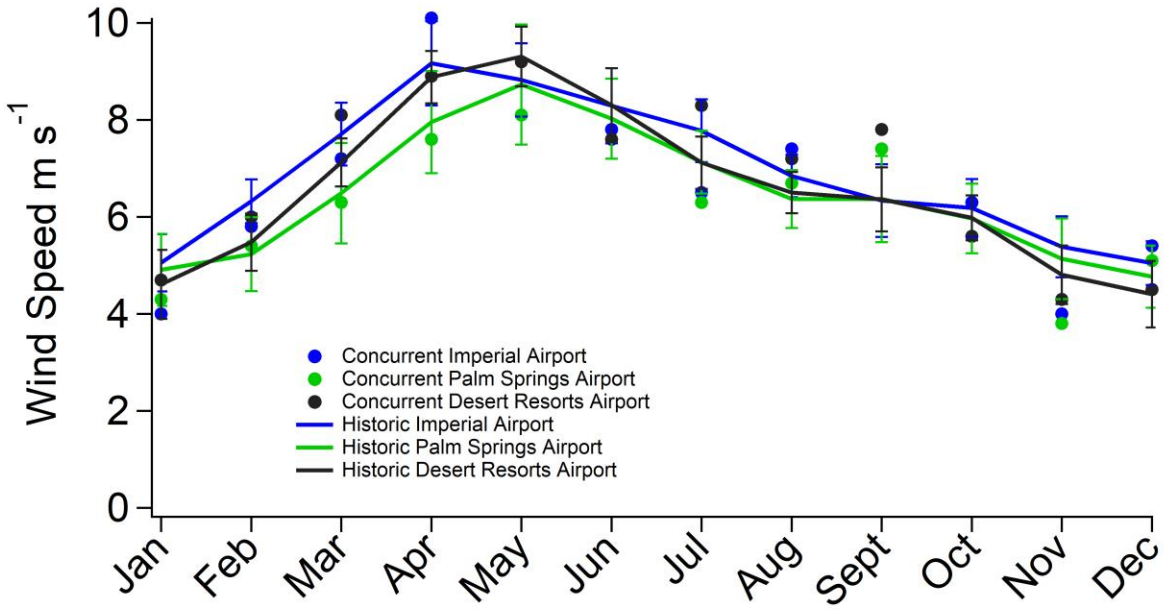

Figure A2.3. Concurrent average monthly (dots) and historic average monthly wind speed (lines) at 3 sites within the Salton Sea Basin. Data from National Oceanic and Atmospheric Association's (NOAA) National Centers for Environmental Information (NCEI).[4] Bars represent 1 standard deviation of the historic means. Site details can be found in table S2.

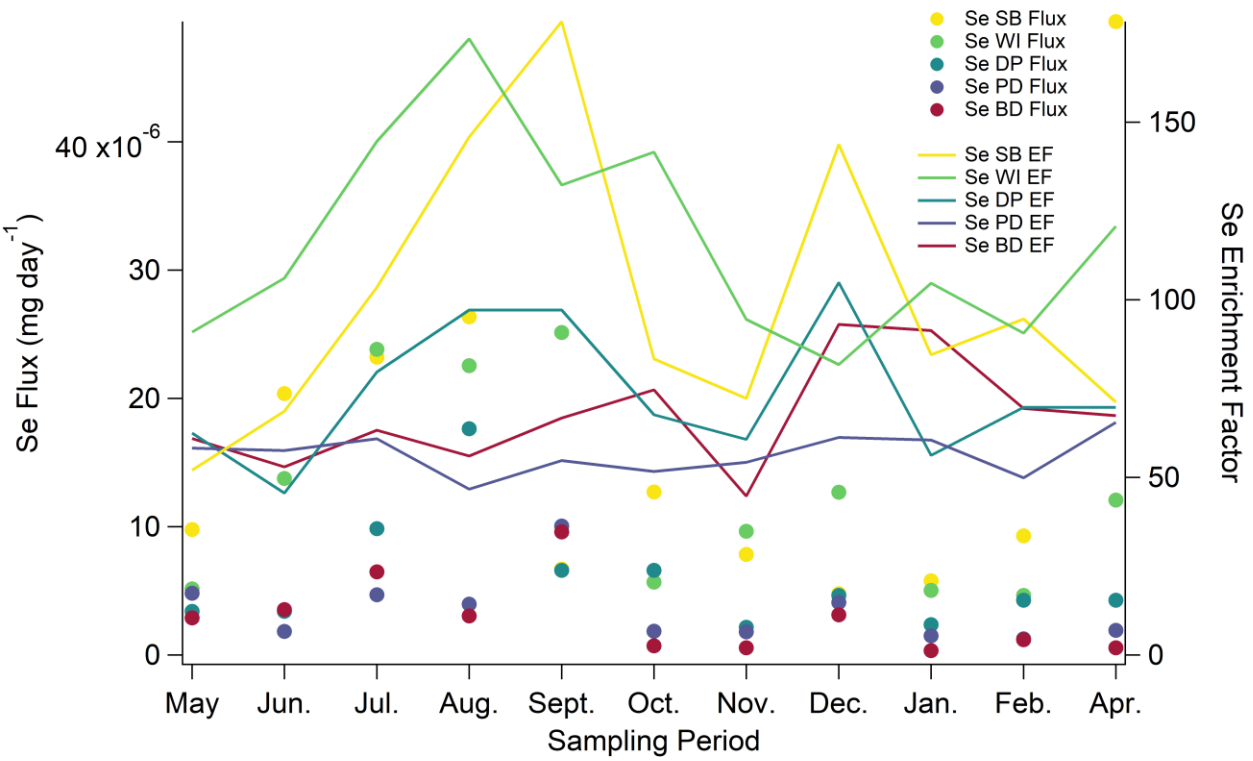

Figure A2.4. Se mass flux (mg day^{-1} pan^{-1}) (dots) and Se Enrichment Factors (lines) at each site for each sampling period.

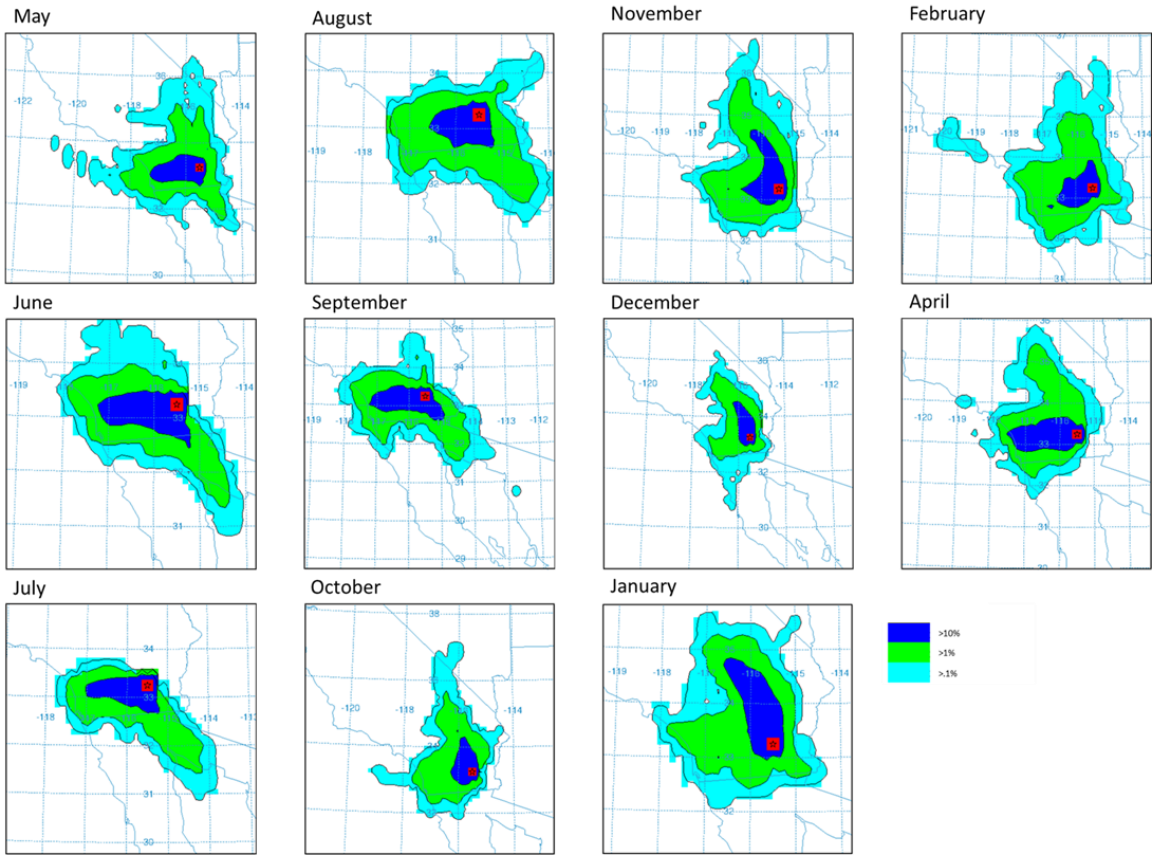

Figure A2.5. Frequency plots of HYSPLIT back trajectories for Sonny Bono Site (marked with a red square) during each respective sampling period. Frequencies were only calculated for trajectories <1,000 m above ground level. Plots show the percentage of back trajectories which cross the same 0.25° cell. Back trajectories were calculated for 12 hours at two hour intervals starting from 00:00 UTC on the day of deployment until 00:00 UTC the day of collection.

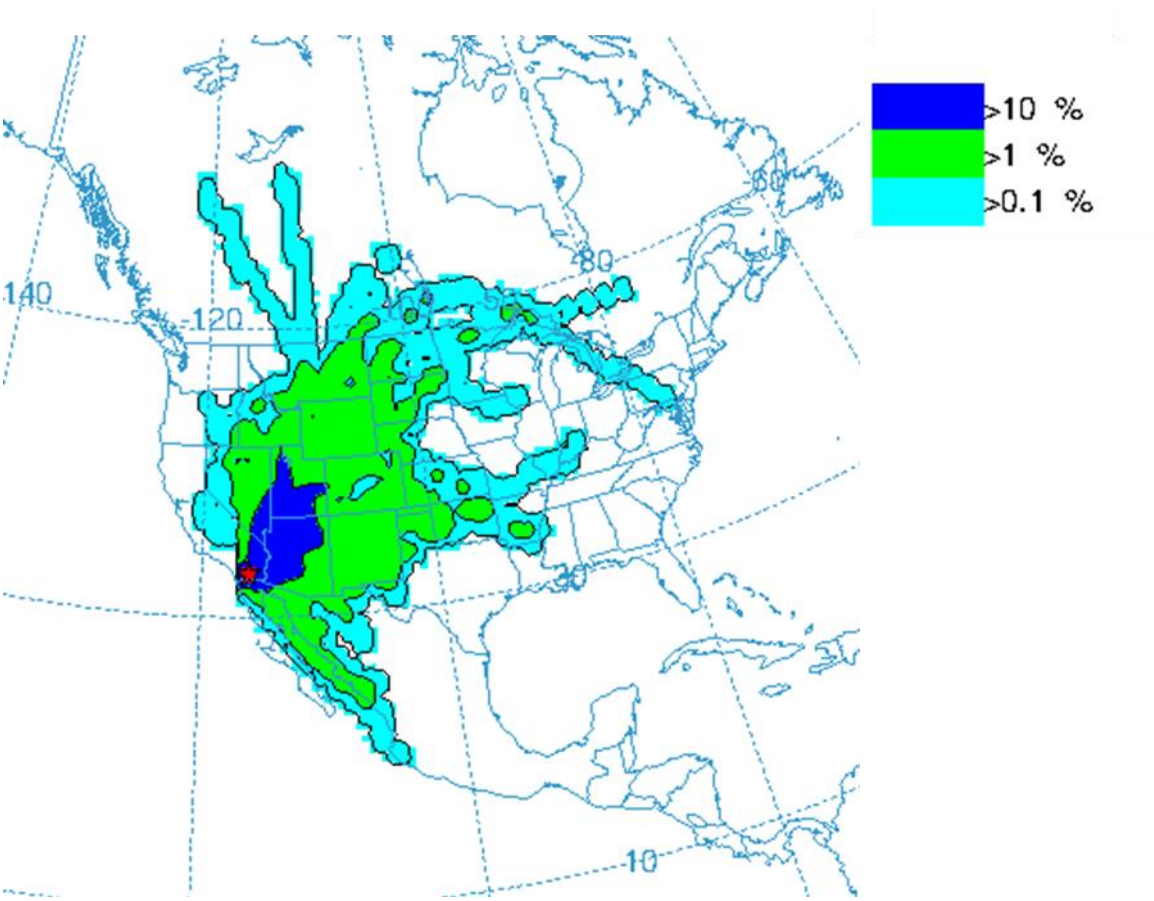

Figure A2.6. Frequency plots of HYSPLIT 72 hr forward trajectories <10,000m for Sonny Bono Site (indicated with a red star) during March 1- June 30, 2018. Plots show the percentage of forward trajectories which cross the same 1.0° cell. Forward trajectories were initialized at 20:00 Local Time.

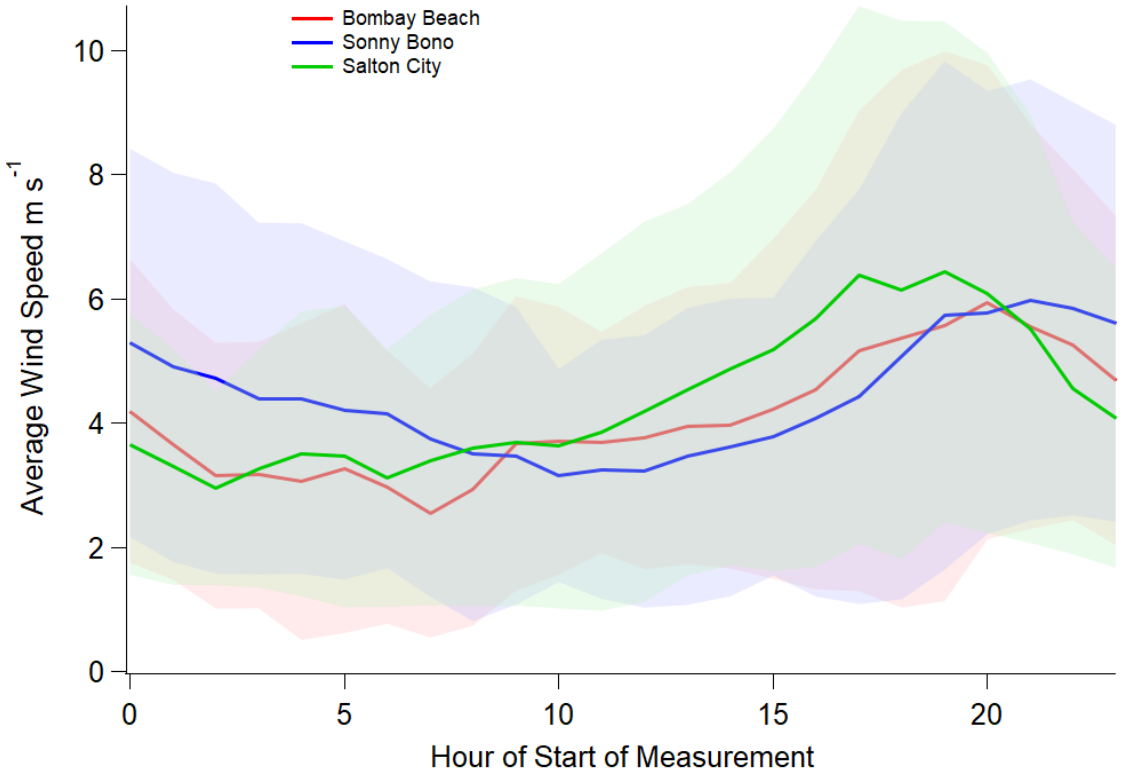

Figure A2.7. Mean wind speed for each hour over the month of April 2018 at three sites around the Salton Sea. Shaded area represents 1 standard deviation. Data acquired from the California Air Resource Board air quality data tool.[6] Sites chosen were Sonny Bono (33.17638 N, -115.62310 W) Bombay Beach (33.35264 N, -115.73419 W), and Salton City (33.27275 N, -115.90062 W).

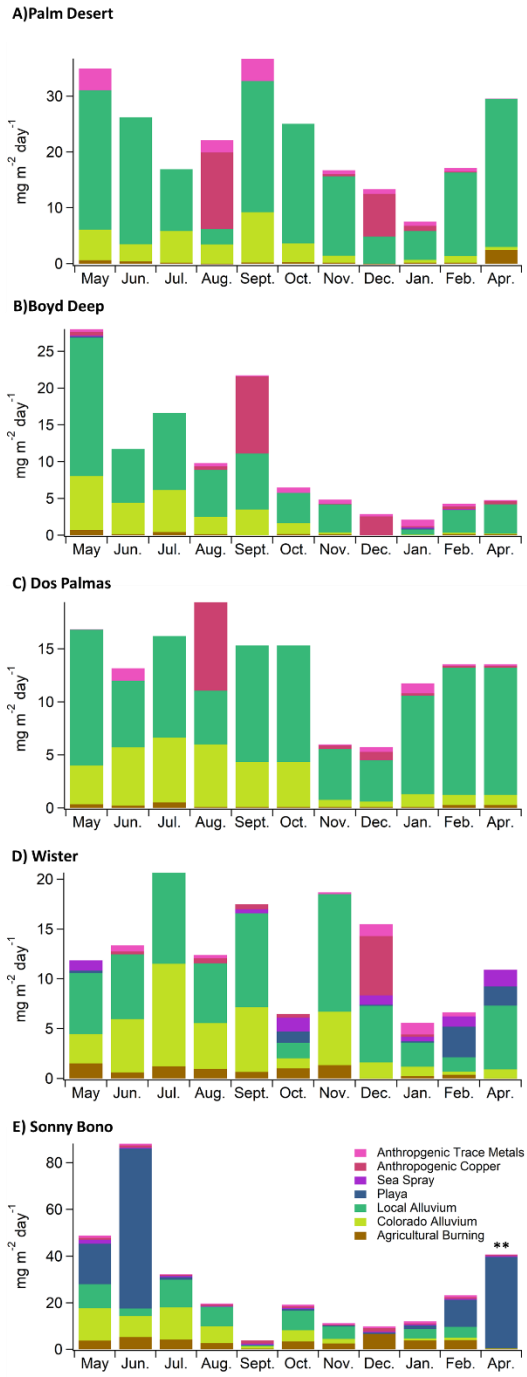

Figure A2.8. PMF mass attributions at A) Palm Desert, B) Boyd Deep, C) Dos Palmas, D) Wister, E) Sonny Bono. PMF attributions are averaged between the duplicate samples for each sampling period. ** SB April 2018 is displayed as $1/10^{th}$ of its value given its high mass concentration compared to the others.

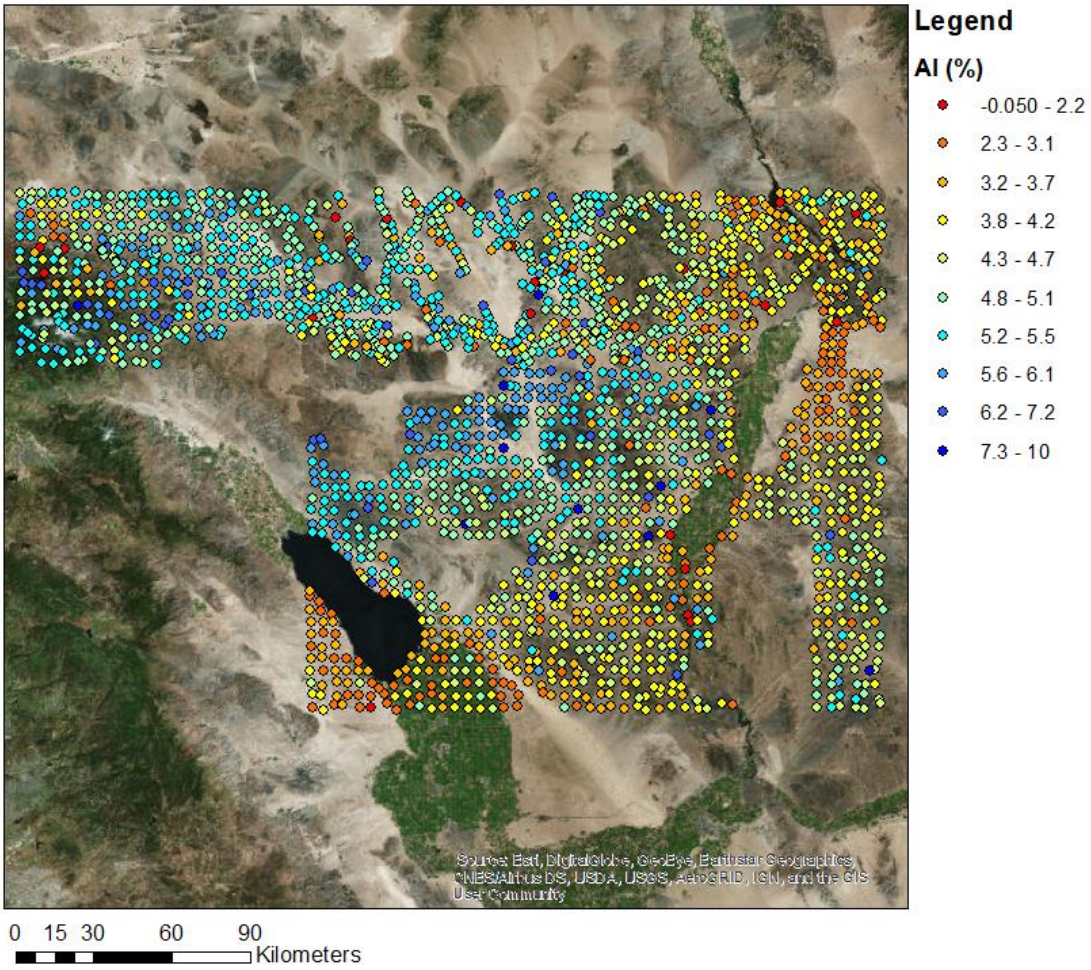

Figure A2.9. Al concentration (%) in soils or sediments in the region around the Salton Sea Basin. Data sourced from the National Uranium Resource Evaluation: Hydrogeochemical and Stream Sediment Reconnaissance.[7]

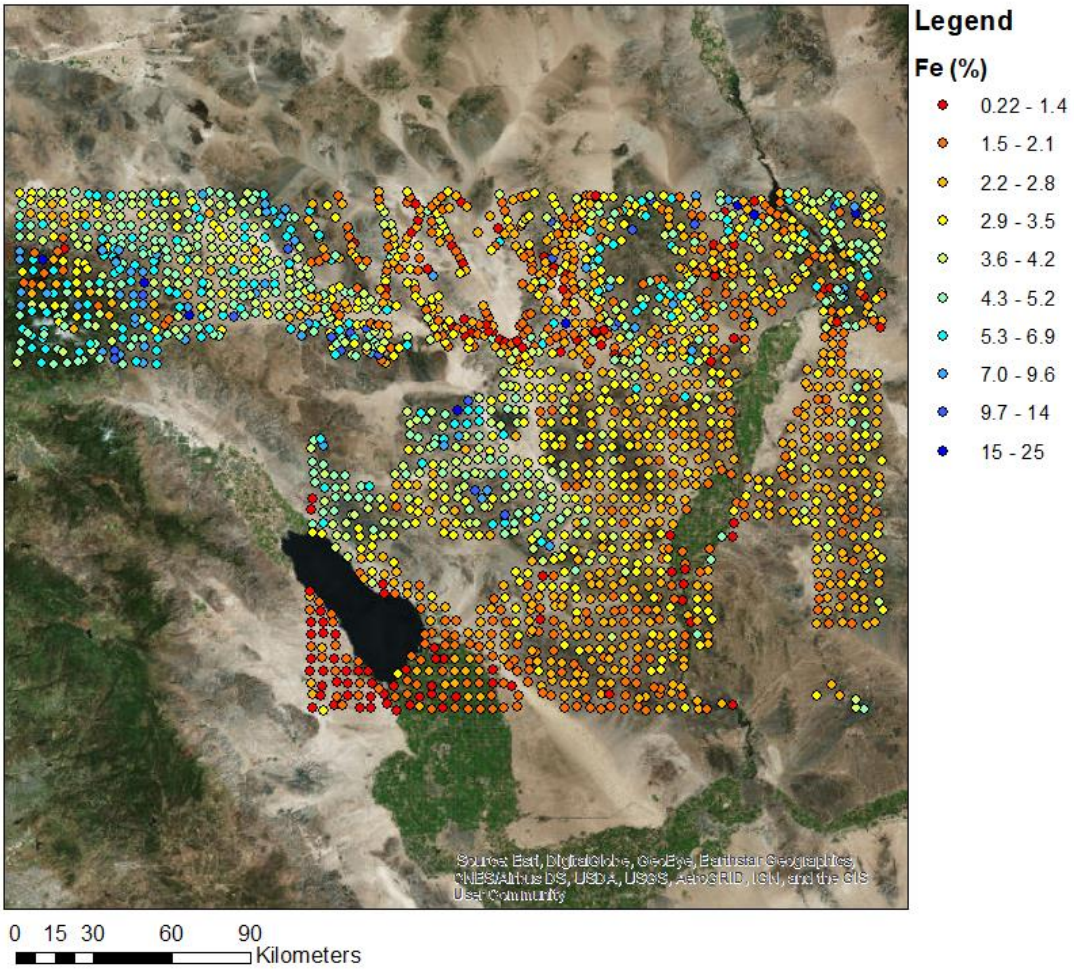

Figure A2.10. Fe concentration (%) in soils or sediments in the region around the Salton Sea Basin. Data sourced from the National Uranium Resource Evaluation: Hydrogeochemical and Stream Sediment Reconnaissance.[7]

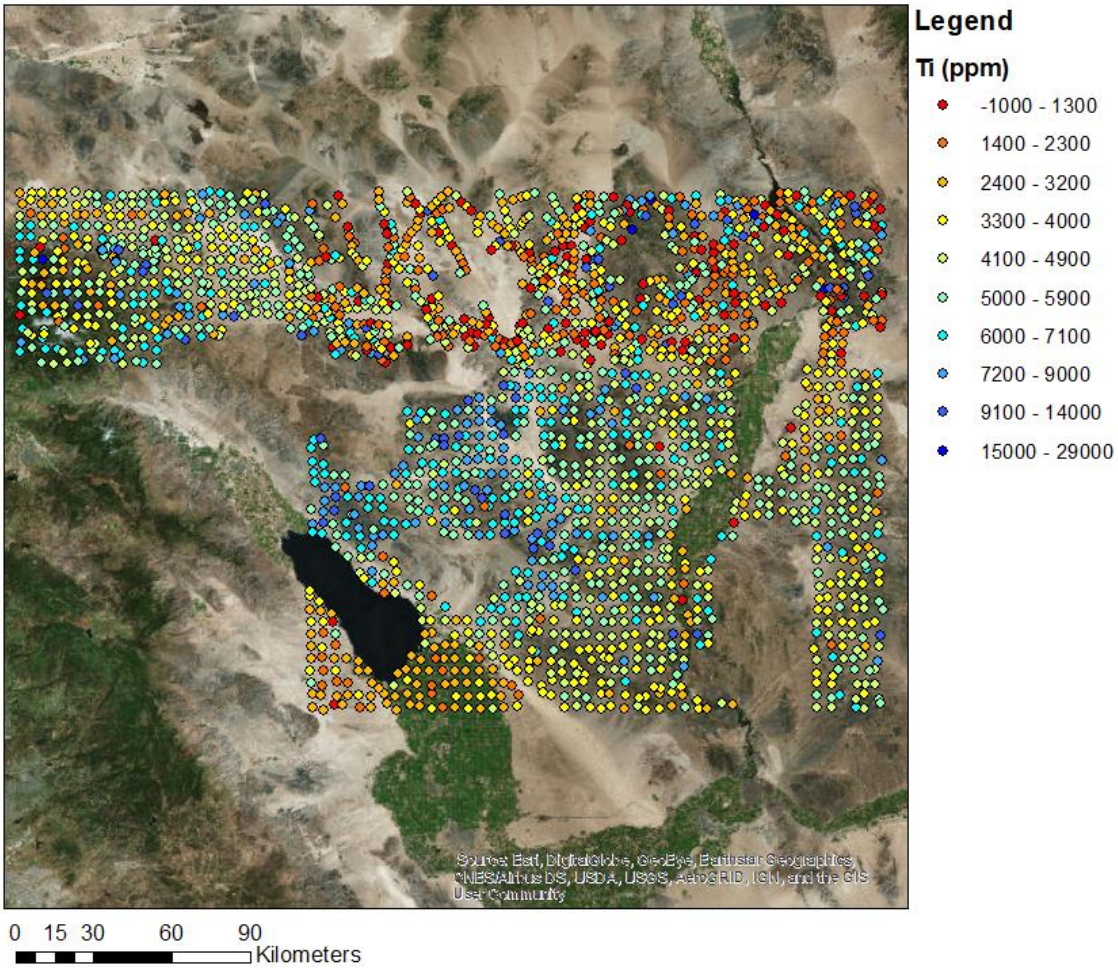

Figure A2.11 Ti concentration (mg kg^{-1}) in soils or sediments in the region around the Salton Sea Basin. Data sourced from the National Uranium Resource Evaluation: Hydrogeochemical and Stream Sediment Reconnaissance.[7]

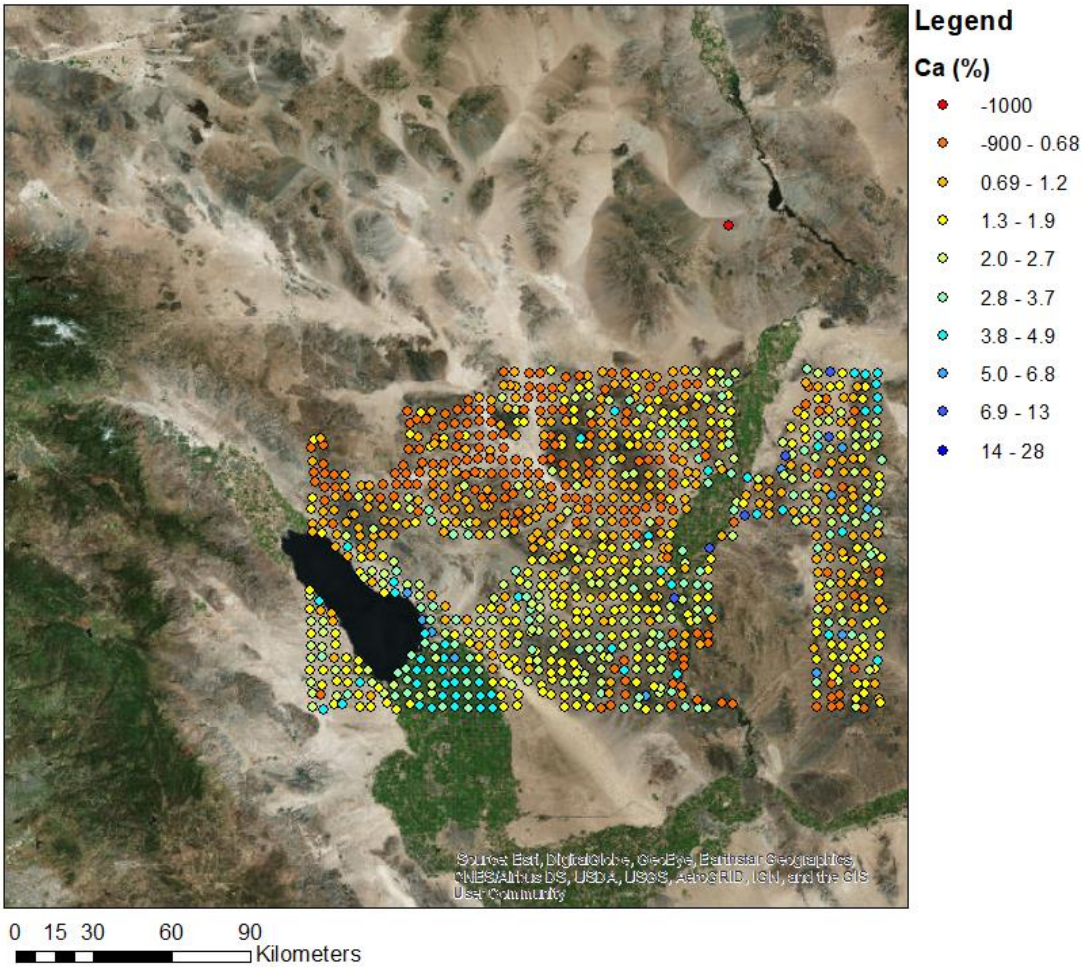

Figure A2.12. Ca (%) concentration in soils or sediments in the region around the Salton Sea Basin. Data sourced from the National Uranium Resource Evaluation: Hydrogeochemical and Stream Sediment Reconnaissance.[7]

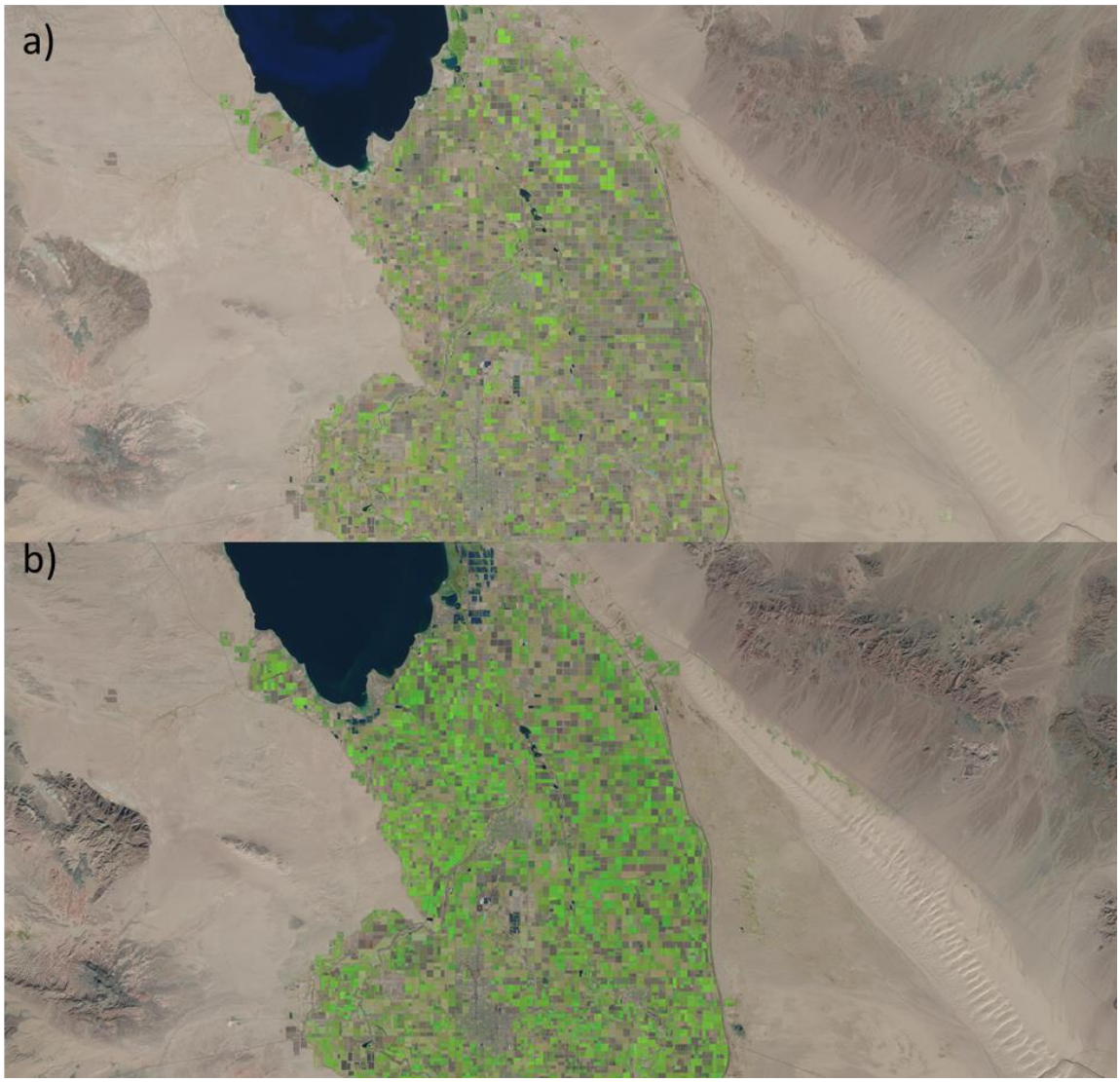

Figure A2.13. Landsat Imagery from the Sentinel 2 MSI for a) August 19th 2017 and b) January 11th 2018. [8]

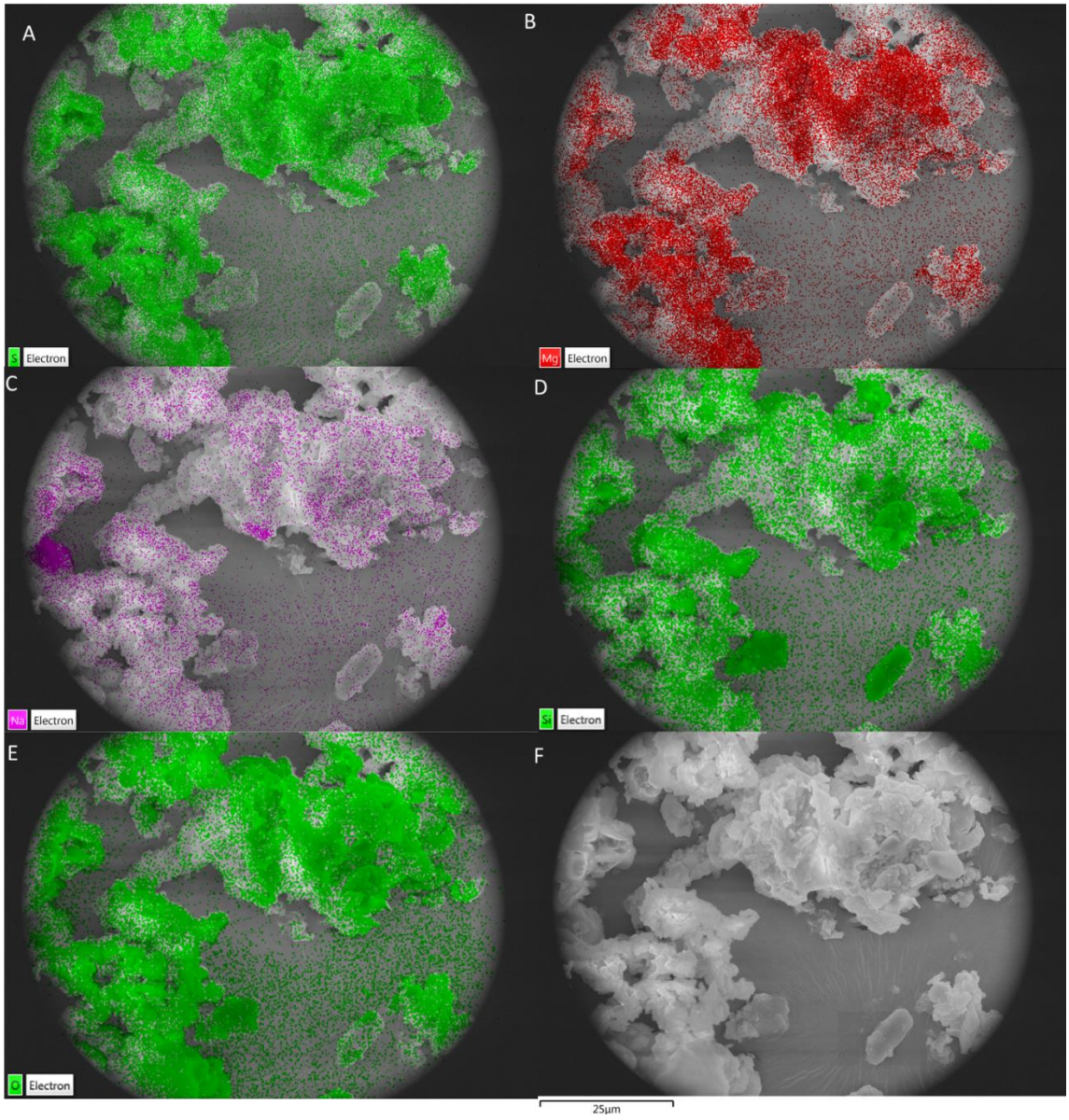

Figure A2.14. SEM-EDS image of SB April 2018 sample. Colors correspond to signal strength of A) S, B) Mg, C) Na, D) Si, and E) O. F) is the backscatter electron image with no color overlay.

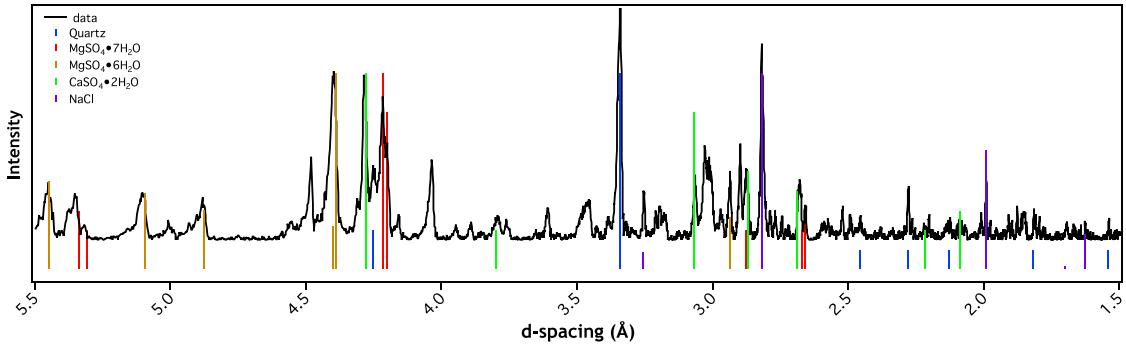

Figure A2.15. X-ray diffraction pattern of SB April 2018 sample. Colored lines represent positions and relative intensities of reflections for evaporite minerals and quartz.

A2.4 Works Cited

1. Reheis, M. C.; Kihl, R., Dust deposition in southern Nevada and California, 1984–1989: Relations to climate, source area, and source lithology. *Journal of Geophysical Research-Atmospheres* **1995,** *100* (D5), 8893-8918.

2. Hopke K., P., A Guide To Positive Matrix Factorization.

3. Stein, A. F.; Draxler, R. R.; Rolph, G. D.; Stunder, B. J. B.; Cohen, M. D.; Ngan, F., NOAA'S HYSPLIT Atmospheric Transport and Dispersion Modeling System. *Bulletin of the American Meteorological Society* **2015,** *96* (12), 2059-2077.

4. National Centers For Environmental Information: Climate Data Online.

5. Reheis, M. C., Dust Deposition in Nevada, California, and Utah, 1984-2002. U.S. Geological Survey Open-File Report 03-138.

6. Air Quality and Meteorological Information System. California Air Resources Board.

7. Smith, S. M., National Geochemical Database:Reformatted Data from the National Uranium Resource Evaluation (NURE) Hydrogeochemical and Stream Sediment Reconnaissance (HSSR) Program:U.S. Geological Survey Open-File Report 97-492. 1997.

8. Landsat-8 Imagery courtesy of the U.S. Geological Survey. US Geological Survey.

Appendix 3: Appendix to Chapter 4: Brown Carbon Formation from Nighttime Chemistry of Unsaturated Heterocyclic Volatile Organic Compounds

A3.1 Text

A3.1.1 Estimated Lifetimes of the Precursors under the Chamber Conditions

The lifetimes (t) of pyrrole, furan and thiophene in the presence of O_3 and NO_3 radicals were estimated using the corresponding rate constants (k) [1] and the typical concentrations of O_3 (750 ppbv) and NO_3 (1000 pptv) after VOC injections, as shown in Table S1. This period was the most ozone favorable portion of the experiment.

A3.1.2 Refractive Index Calculations

RI values were calculated by minimizing the absolute difference between the observed and theoretical optical coefficients of a size distribution over a range of RI inputs, at times when the mode change between consecutive SEMS measurements was lower than 10%.[2-5] For pyrrole and thiophene experiments, n_{375} and k_{375} values were calculated when PAX measurements were above the detection limits for both $\beta_{scat,375}$ and $\beta_{abs,375}$.

Refractive index (RI) values are size-independent measures of the fundamental interactions of a material with radiation. The RI consists of two components, a real component which controls scattering (n) and an imaginary component which controls absorption (k). These values determine scattering and absorption efficiencies (Q_{scat}, Q_{abs}) of a particle at a given wavelength. Q_{scat} and Q_{abs} relate the amount of radiation attenuated by each process to particle diameter (d_p). Q_{scat} and Q_{abs} can be combined with size distribution measurements to calculate theoretical integrated scattering and absorption coefficients (β_{scat_theo}, β_{abs_theo}):

$$\beta_{\text{scat or abs\_theo}} = \sum_{d_{p,1}}^{d_{p,end}} Q_{\text{scat or abs}}(d_i, \lambda, n, k) \times N_i \times \frac{(\pi \times {d_i}^2)}{4} \quad \text{(A3.1)}$$

where $d_{p,1}$ is the smallest bin diameter, $d_{p,end,}$ the largest bin diameter, and N_i the number concentration of aerosols at size d_i. To calculate an unknown RI, β_{scat_theo} and β_{abs_theo} were calculated over a large range of n and k values and compared to β_{scat_obs} and β_{abs_obs}, as measured by PAX, through a merit parameter. Here, n was iterated between 1.2 and 1.6 at steps of 0.01 and k was iterated between 0 and 0.2 at steps of 0.001. The input pair that minimized the merit parameter was chosen as the RI calculated (RI_{calc}). Here a simple merit parameter, summed difference (Δ), was used.

$$\Delta = \left|(\beta_{\text{scat\_obs}} - \beta_{\text{scat\_theo}})\right| + \left|(\beta_{\text{abs\_obs}} - \beta_{\text{abs\_theo}})\right| \quad \text{(A3.2)}$$

RI calculations using difference or weighted difference methods can also be found elsewhere.[2-4]

A3.1.4 Filter Treatment and Extraction Efficiency

The filter samples were stored at −20 °C to minimize evaporation of semi-volatile organic compounds. The filters were extracted with 22 mL of methanol (≥99.8%, Fisher Scientific) by 50 min of sonication. The extracted solution was dried under a gentle stream of nitrogen (≥99.8%, Airgas). The residues were reconstituted in 150 μL of methanol for chemical analyses and further diluted for UV-Vis measurements (Beckman DU-640) to ensure the detector would not be saturated. The extraction efficiency was estimated to be ~86% using the surrogate standards (i.e., levoglucosan and *p*-nitrophenol), as described in SI. The same extraction procedure was performed for a blank filer. There was no significant absorbance observed from the UV-Vis spectrum of the blank extract.

To estimate the extraction efficiency of filter samples, 5 μL solution of levoglucosan (1.1 mg mL^{-1}) and *p*-nitrophenol (0.97 mg mL^{-1}) were used as the reference standard and added onto a filter (Zefluor, Pall Laboratory, 47 mm, 1.0 μm pore size). The filter was then extracted with 22 mL methanol followed by sonication and dry-off procedures. Another 5 μL reference standard was added directly into a 25-mL vial that was then applied to dry-off process. Then, 100 μL N,O-Bis(trimethylsilyl) trifluoroacetamide with trimethylchlorosilane (BSTFA+TMCS) (99:1; Sylon BFT) and 50 μL anhydrous pyridine (99.8%, DriSolv) were added to each vial to derivatize the hydroxyl groups. The derivatized solutions were then used for GC-MS analysis. The extraction efficiency was estimated to be 86% using the relative concentrations of levoglucosan and *p*-nitrophenol in these two vials.

A3.1.5 LC-DAD-ESI-HR-TOFMS Analysis

The TOFMS acquired mass spectra from *m/z* 63-1050. The chromatographic separations were carried out using Waters XBridge BEH C-18 column (2.1mm ID, 50 mm length, 2.5 um particle size) at 45°C. The mobile phases consisted of eluent (A) 0.1% acetic acid in water and eluent (B) 0.1% formic acid in methanol. The applied 15-min gradient elution program was as follows: the concentration of eluent B was 0% for the first 2 min, increased to 90% from 2-12 min, held at 90% from 12-14 min, and then decreased back to 0% from 14-15 min, and held at 0% from 15-20 min. The post-run time was 2 min. The LC flow rate and injected sample volume were 0.25 mL min^{-1} and 20 µL, respectively. Prior to LC-DAD-ESI-HR-TOFMS analysis, the TOFMS instrument was calibrated using a commercially available ESI-L low concentration tuning mixture (Agilent Technology, Part number G1969-85000). This external calibration was done in the low-mass range (m/z <1700) mode.

A3.2 Tables

Table A3.1. The comparison of the MAC of SOA in this study with those of SOA in other studies

Precursor	Oxidant and seed	<MAC> ($cm^2\ g^{-1}$)	Reference
Limonene	O_3	400 [a]	Updyke et al. [9]
Limonene	OH	170 [a]	Updyke et al. [9]
α-Cedrene	O_3	260 [a]	Updyke et al. [9]
α -Humulene	O_3	300 [a]	Updyke et al. [9]
Farnesene	O_3	60 [a]	Updyke et al. [9]
α-Pinene	O_3	50 [a]	Updyke et al. [9]
α-Pinene	OH	100 [a]	Updyke et al. [9]
Pine Needle Oil	O_3	100 [a]	Updyke et al. [9]
Cedar Leaf Oil	O_3	500 [a]	Updyke et al. [9]
Isoprene	OH	50 [a]	Updyke et al. [9]
Isoprene	O_3	10 [a]	Updyke et al. [9]
Tetradecane	OH	80 [a]	Updyke et al. [9]
1,3,5-trimethylbenzene	OH	20 [a]	Updyke et al. [9]
1,3,5-trimethylbenzene	OH (Intermediate, VOC/NO_x=7.5)	70 [a]	Updyke et al. [9]
Naphthalene	OH	200 [a]	Updyke et al. [9]
Naphthalene	OH (high NO_x, VOC/NO_x=3.3)	1000 [a]	Updyke et al. [9]
IEPOX	$MgSO_4$ [b]	11-344 [c]	Lin et al. [10]
IEPOX	$(NH_4)_2SO_4$ [b]	5-15 [c]	Lin et al. [10]
Isoprene	NO_x free	43 [d]	Liu et al. [11]
Isoprene	OH (high NO_x, VOC/NO_x=0.9)	16 [d]	Liu et al. [11]
α-Pinene	OH (NO_x free)	53 [d]	Liu et al. [11]
α-Pinene	OH (high NO_x, VOC/NO_x=1.0)	155 [d]	Liu et al. [11]
1,3,5-Trimethylbenzene	OH (NO_x free)	89 [d]	Liu et al. [11]
1,3,5-Trimethylbenzene	OH (high NO_x, VOC/NO_x=1.3-1.6)	782 [d]	Liu et al. [11]
Toluene	OH (NO_x free)	66 [d]	Liu et al. [11]
Toluene	OH (high NO_x, VOC/NO_x=1.2-1.5)	3018 [d]	Liu et al. [11]
d-Limonene	O_3, acidic seed	40-500 [e]	Nguyen et al. [12]

[a] The MAC values were averaged over the range of 300-700 nm.
[b] Aerosols were from reactive uptake of synthetic IEPOX standard onto the acidified or non-acidified aerosols
[c] The MAC values were averaged over the range of 290-700 nm
[d] The MAC values were averaged over the range of 300-700 nm
[e]. The MAC values were averaged over the range of 300-700 nm

A3.3 Figures

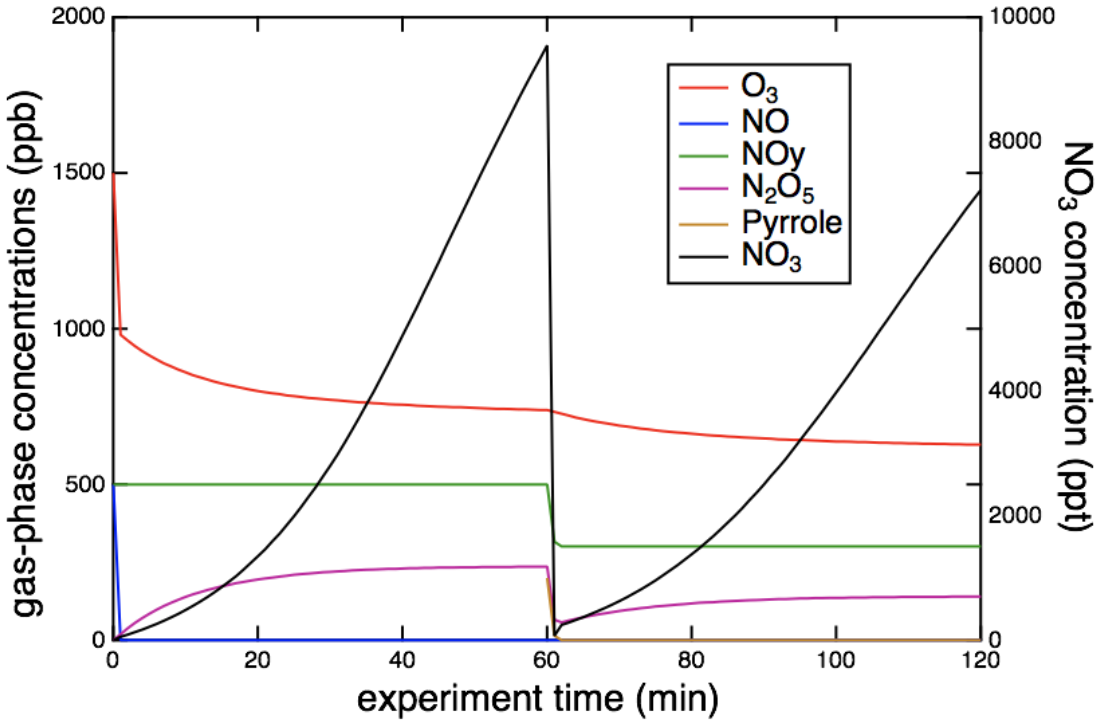

Figure A3.1. Kinetic box-model simulation of NO_3 radical production during the experiment.[14-16] Initial O_3 set to 1500 ppb and NO set to 500 ppb. A 200-ppb pyrrole injection is simulated at 60 minutes.

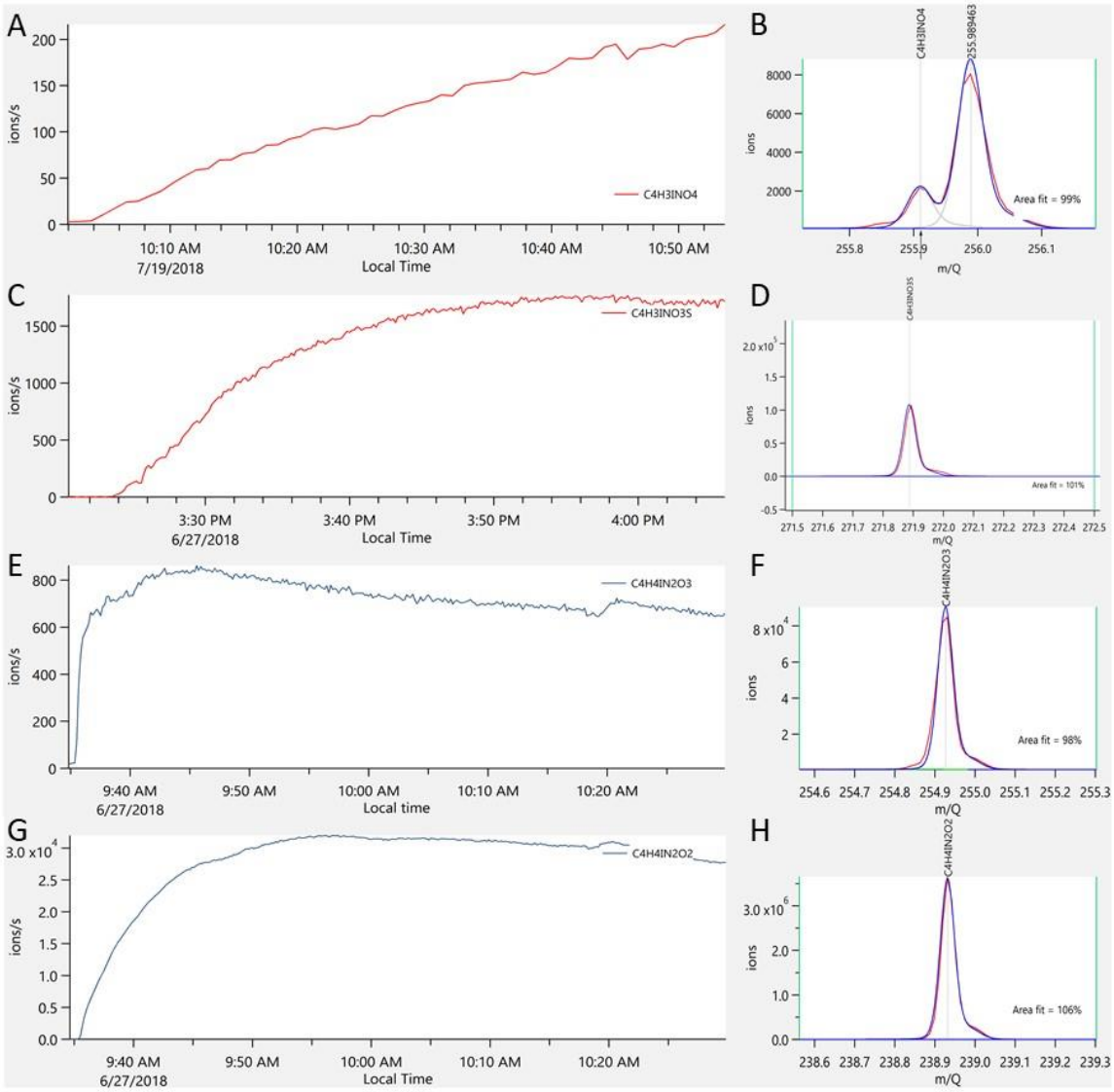

Figure A3.2. The CIMS time series of possible nitrate-furan (A), nitrate-thiophene (C), nitrate-pyrrole (E), and nitropyrrole (G). Local time is the time of the experiment, beginning at the start of the experiment. Mass fittings of nitrate-furan (B), nitrate-thiophene (D), nitrate-pyrrole (F), and nitropyrrole (H) as assigned using Tofware 3.03 (Aerodyne Research Inc), where blue represents the fit to the peak and red is the observed signal.

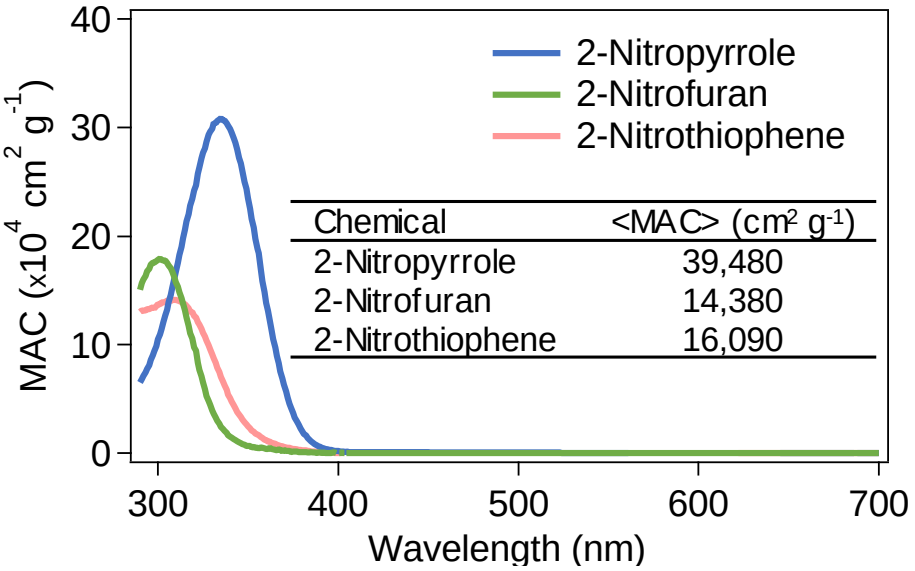

Figure A3.3. The MAC of heterocyclic nitro compound standards as a function of wavelength, including 2-nitropyrrole, 2-nitrofuran, and 2-nitrothiophene.

A3.4 Works Cited

1 Atkinson, R., Aschmann, S. M., Winer, A. M. & Carter, W. P. Rate Constants for the Gas-phase Reactions of Nitrate Radicals with Furan, Thiophene, and Pyrrole at 295+/-1 K and Atmospheric Pressure. *Environ. Sci. Technol.* **19**, 87-90 (1985).

2 Denjean, C. *et al.* A new experimental approach to study the hygroscopic and optical properties of aerosols: application to ammonium sulfate particles. *Atmos. Meas. Tech.* **7**, 183-197, doi:10.5194/amt-7-183-2014 (2014).

3 Denjean, C. *et al.* Aging of secondary organic aerosol generated from the ozonolysis of alpha-pinene: effects of ozone, light and temperature. *Atmos. Chem. Phys.* **15**, 883-897, doi:10.5194/acp-15-883-2015 (2015).

4 De Haan, D. O. *et al.* Brown Carbon Production in Ammonium- or Amine-Containing Aerosol Particles by Reactive Uptake of Methylglyoxal and Photolytic Cloud Cycling. *Environ. Sci. Technol.* **51**, 7458-7466, doi:10.1021/acs.est.7b00159 (2017).

5 Zarzana, K. J., Cappa, C. D. & Tolbert, M. A. Sensitivity of Aerosol Refractive Index Retrievals Using Optical Spectroscopy. *Aerosol Sci. Technol.* **48**, 1133-1144, doi:10.1080/02786826.2014.963498 (2014).

6 Dingle, J. H., Zimmerman, Stephen, Frie, Alexander L. , Min, Justin , Jung, Heejung, Bahreini, Roya. Complex Refractive Index, Single Scattering Albedo, and Mass Absorption Coefficient of Secondary Organic Aerosols Generated from Oxidation of Biogenic and Anthropogenic Precursors. *Aerosol Science and Technology*, doi:10.1080/02786826.2019.1571680 (2019).